Thesis submitted for the degree

Doctor of Philosophy

Scanning Tunneling Microscopy and Photoelectron Spectroscopy Studies of Lead Halide Perovskite Surfaces, Defect Dynamics and the $MAPbX_3$-CuPc Interface

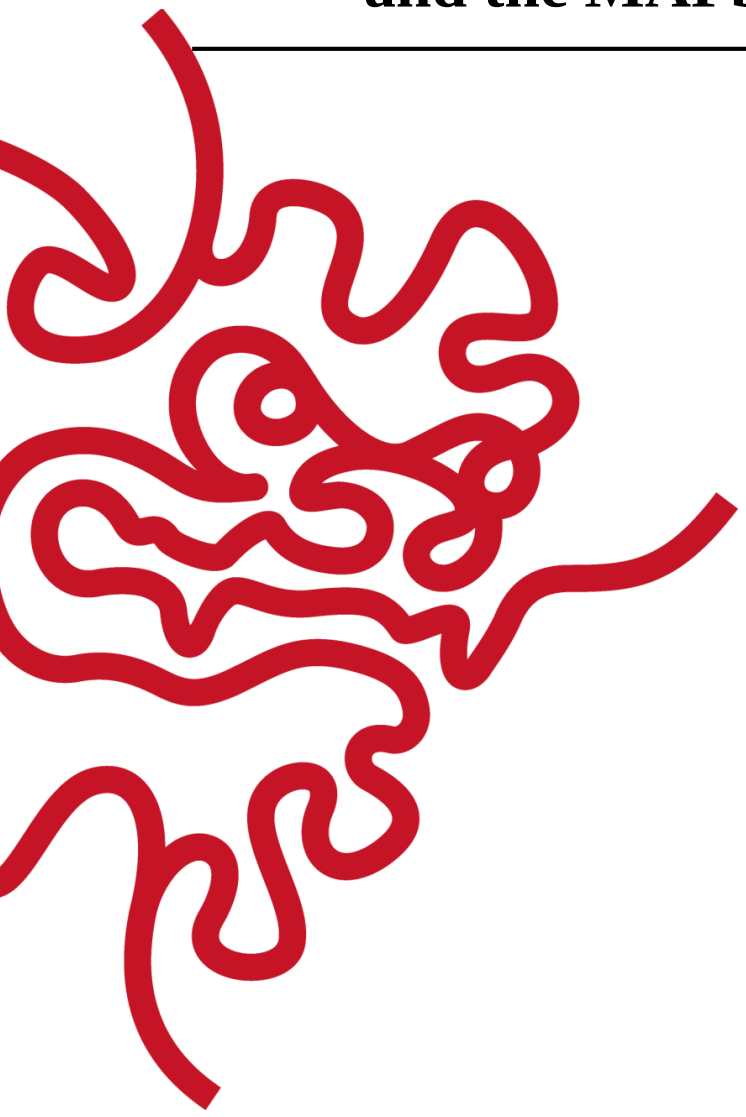

by

Collin Stecker

Supervisor: **Yabing Qi**

April, 2020

Declaration of Original and Sole Authorship

I confirm that:

- This work was done solely while a candidate for the research degree at the Okinawa Institute of Science and Technology Graduate University, Japan.
- No part of this work has previously been submitted for a degree at this or any other university.
- References to the work of others have been clearly attributed. Quotations from the work of others have been clearly indicated, and attributed to them.
- In cases where others have contributed to part of this work, such contribution has been clearly acknowledged and distinguished from my own work.
- None of this work has been previously published elsewhere, with the exception of the following:

  - Chapter 3 was largely derived, with permission, from the publication: Stecker, C.; Liu, K.; Hieulle, J.; Ohmann, R.; Liu, Z.; Ono, L. K.; Wang, G.; Qi, Y., Surface Defect Dynamics in Organic–Inorganic Hybrid Perovskites: From Mechanism to Interfacial Properties. *ACS Nano.* **2019,** *13* (10), 12127-12136.

  - Chapter 4 was largely derived, with permission, from the publication: Hieulle, J.; Wang, X. M.; Stecker, C.; Son, D. Y.; Qiu, L. B.; Ohmann, R.; Ono, L. K.; Mugarza, A.; Yan, Y. F.; Qi, Y. B., Unraveling the Impact of Halide Mixing on Perovskite Stability. *J. Am. Chem. Soc.* **2019,** *141* (8), 3515-3523.

  - Chapter 6 was largely derived, with permission, from the publication: Hieulle, J.; Luo, S.; Son, D.-Y.; Jamshaid, A.; Stecker, C.; Liu, Z.; Na, G.; Yang, D.; Ohmann, R.; Ono, L. K.; Zhang, L.; Qi, Y.B. Imaging of the Atomic Structure of All-Inorganic Halide Perovskites. *J. Phys. Chem. Lett.* **2020**, 818-823.

Date: Feb. 6th, 2020

Signature: Collin Stecker

Abstract

Over the past decade, lead halide perovskites (PVKs) have emerged as a promising new light absorber material for thin film solar cells. Lab-scale perovskite-based photovoltaic devices have made impressive gains in power conversion efficiency (PCE) and are nearing the same efficiency as silicon-based solar cells. However, perovskite solar cells lack stability, and this is a major obstacle preventing commercialization. The interfaces between the different layers in a device have been implicated as potential areas of charge recombination and material degradation. Understanding the perovskite surface is crucial because it is involved in these interfaces and also because it is the layer that is in first contact with extrinsic species that may cause degradation. Defects in the perovskite material have also been identified as a potential cause of sub-optimal performance. Additionally, some strategies for improving stability have included using mixed halide perovskites, or perovskites containing cesium instead of or mixed with organic cations such as methylammonium (MA). Reports at the device engineering level are plentiful, but fundamental, atomic-scale understanding of the perovskite surface is scarce, especially from an experimental perspective. This bulk of this thesis focuses on scanning tunneling microscopy (STM) studies examining the perovskite surfaces of $CsPbBr_3$ and mixed halide perovskites $MAPbBr_{3-y}I_y$ and $MAPbBr_{3-z}Cl_z$, the surface defects of $MAPbBr_3$ and their dynamics, as well a device-relevant perovskite/hole transport material (HTM) interface comprised of $MAPbX_3$/CuPc, where X=I or Br. Furthermore, X-ray photoelectron spectroscopy (XPS) is used to characterize stability of the material, and electronic properties are investigated by ultraviolet photoemission spectroscopy (UPS). Where feasible, these experimental results are corroborated by density functional theory (DFT) calculations performed by collaborators. The goal of this thesis is to provide fundamental insight regarding perovskite surfaces, their defects and their dynamics, and their interfaces with other materials, which may help guide applied research toward creating devices with better performance and stability.

Acknowledgements

First and foremost, I would like to thank the millions of Japanese taxpayers who helped provide financial support for my studies. I would also like to thank the Okinawa Institute of Science and Technology Graduate School staff for their strong administrative support that allowed me to focus on my research.

I would like to give my deepest gratitude to my supervisor, Professor Yabing Qi, for his invaluable academic guidance over the past 5 years and for being so generous in giving me an opportunity to work in his lab and providing the materials and equipment to realize our experimental ideas. He has helped me develop both as a scientist and as a person. I would also like to give special thanks to our lab's group leader, Luis K. Ono, who provided valuable scientific discussion, help when troubleshooting issues in the lab, coordination with equipment companies, and camaraderie during our daily lunches. Your endless optimism is admirable.

I would also like to thank all the other members, past and present, of the Energy Materials and Surface Sciences Unit. You all have helped me learn a lot during my time at OIST. In particular, I would like to thank Dr. Robin Ohmann, who graciously took me under his wing and patiently taught me how to use the STM. Your advice at all points in the scientific process was always thoughtful and I appreciate the time you took to help. Your kind personality and friendship was greatly appreciated. I would also like to specifically thank Dr. Jeremy Hieulle, who is the lead author for the projects presented in Chapters 4 and 6, and contributed greatly to data acquisition, analysis and figure creation of these projects. He was an invaluable mentor and a great collaborative partner for working split-shifts on the STM. Your insightful scientific advice at all points in the scientific process was greatly appreciated. I am also thankful for psychological support and friendship during the rougher spots, your sense of humor was a great help in diffusing some of the stress. I would also like to thank all the DFT collaborators for their hard work on the projects in Chapters 3,4 and 6.

Finally, I would like to thank all of my friends and family, both here at OIST and back home. Your emotional support was absolutely essential. You helped me stay balanced and connected, and reminded me there is a world outside of graduate school.

List of Abbreviations

α-CuPc	Alpha-phase CuPc
Al_2O_3	Aluminum Oxide
β-CuPc	Beta-phase CuPc
CB(M)	Conduction Band (Minimum)
$CsPbBr_3$	Cesium Lead Bromide
CuPc	Copper Phthalocyanine
DFT	Density Function Theory
DOS	Density of States
E_a	Activation Energy
ETL	Electron Transport Layer
FA	Formamidinium
FTO	Fluorine-doped Tin Oxide
HTL	Hole Transport Layer
IE	Ionization Energy
ITO	Indium-doped Tin Oxide
J_{sc}	Short-circuit current
K-cell	Knudsen Cell
Li-TFSI	bis(trifluoromethane)sulfonimide lithium salt
MA	Methylammonium
MABr	Methylammonium Bromide
MAI	Methylammonium Iodide
$MAPbBr_3$	Methylammonium Lead Bromide
$MAPbI_3$	Methylammonium Lead Iodide
O_2^-	Superoxide radical
OHP	Organic-inorganic Hybrid Perovskite
P3HT	poly(3-hexylthiophene)

$PbBr_2$	Lead bromide
$PbCl_2$	Lead Chloride
PbI_2	Lead Iodide
PCBM	Phenyl-C_{61}-Butyric acid Methyl ester
PCE	Power Conversion Efficiency
PEDOT:PSS	poly(3,4ethylenedioxythiophene):polystyrene sulfonate
PES	Photoelectron Spectroscope
PL	Photoluminescence
PTAA	poly(triarlyamine)
QCM	Quartz Crystal Microbalance
SA	Self-Assembled
SnO_2	Tin Oxide
Spiro-MeOTAD	2,2′,7,7′-tetrakis(*N*,*N*-di-*p*-methoxyphenylamine)-9,9′-spirobifluorene
STM	Scanning Tunneling Microscope
tBP	4-tert-butylpyridine
TiO_2	Titanium Dioxide
TMPc	Transition Metal Phthalocyanine
UHV	Ultra High Vacuum
UPS	Ultraviolet Photoelectron Spectroscopy
VB(M)	Valence Band (Maximum)
V_i	Iodide Vacancy
V_{MA}	Methylammonium Vacancy
V_{oc}	Open-circuit voltage
XPS	X-ray Photoelectron Spectroscopy

List of Figures

Table of Contents

Chapter 1: General Introduction

1.1 Motivation

This thesis takes an experimental approach to examining the surfaces of organic-inorganic perovskite (OHP) materials at the atomic scale, and the findings are discussed in the context of photovoltaic applications, with additional support from theoretical work performed by collaborating research groups. Material surfaces, as well as interfaces between adjacent materials in photovoltaic devices, have been identified as key areas affecting device performance and stability. The passivation of surfaces and defects has been established as a useful method for improving device performance, and is described in Section 1.3. However, a detailed picture of the perovskite surface at the atomic scale is lacking, especially from an experimental perspective. Identifying the types of defects at the surface and how the surface reconstructs in various perovskite formulations provides a more accurate picture of the perovskite surface and can help inform future surface passivation strategies. Additionally, examining submonolayer coverages of charge selective layer materials on top of perovskite allows for the identification of how the two materials interact with each other at this interface. This can lead to better modelling of the interface and potentially identify fundamental reasons for better or worse charge transfer and performance for a given charge selective layer. Based on these motivations, this thesis provides the first atomic resolution images of vacancy defects cluster and the movement of individual ions in OHP materials. The surfaces of mixed halide and Cs-based perovskites were imaged with atomic resolution for the first time, and the effect of changing the X-site and A-site ions on the surface layer structure was revealed. Finally, the interfacial layer of CuPc on $MAPbX_3$ was shown to have a different orientation than previously proposed based on theoretical work in the literature. This highlights the importance of verifying theoretical studies with atomic resolution experimental work, and could lead to a better understanding of charge transfer and performance in OHP solar cell devices that utilize CuPc as a hole transport layer (HTL). This work establishes a general approach that can be further employed to investigate interfaces between OHPs and other device-relevant charge transport layers.

1.2 Overview: organic-inorganic hybrid perovskite (OHP) solar cells

Solar energy from photovoltaics has the potential to decrease carbon emissions and contribute to a more sustainable energy industry. Silicon-based solar panels are widely deployed in the market, but are not suitable for all applications as they are heavy and lack flexibility. Solar panels utilizing organic-inorganic halide perovskites (OHPs) as the light absorbing material have the potential to offer a high efficiency, low-cost solution that is compatible with flexible substrates. It should be noted that OHPs also have applications in other optoelectronic applications, including LEDs[1-4] and lasers,[5, 6] but this thesis will mainly be framed in the context of solar cells.

OHPs have a general molecular formula of ABX_3 (Fig. 1.1), where A is an organic cation, B is a metal 2+ cation (Pb, Sn), and X is a halide ion (I, Br, Cl), and were first shown to be useable as light absorbers in solar cells in 2009.[7] The B cation is coordinated with six halide ions in the X position to form an octahedral framework. The A cation can be organic or inorganic and has 12 nearest neighbors, lying in a cuboctahedral site.

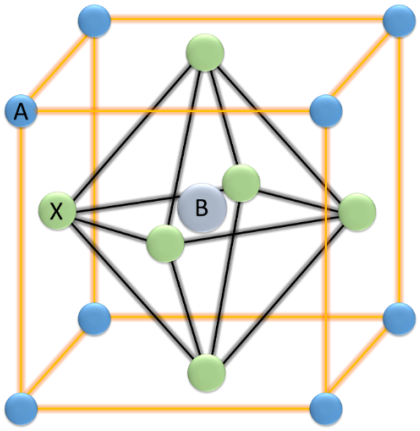

Figure 1.1 Perovskite unit cell with general formula ABX_3.

OHPs have exhibited unique and exceptional optoelectronic properties, including high charge carrier mobility, high absorption coefficient, long charge carrier diffusion lengths, low exciton binding energy and band gaps suitable for efficient absorption of solar irradiation.[8-11] Kojima et al. utilized methylammonium lead iodide ($MAPbI_3$) and methylammonium lead bromide ($MAPbBr_3$) in a cell architecture similar to those used in dye-sensitized solar cells3 to achieve a power conversion efficiency (PCE) of 3.8% and 3.1%, respectively.[7] This work set off a flurry of research into this material class, with the next breakthrough occurring when Kim et al.

used $MAPbI_3$ as a light absorber in a mesoscopic all-solid-state architecture to produce cells with a power conversion efficiency (PCE) of 9.7%.[10] In the ensuing decade, record efficiencies saw a meteoric rise, with the current record for PCE exceeding 25%, a value comparable to conventional Si single crystal solar cells.[12] This rapid rise in achievable efficiency was realized through optimization of processing conditions and cell architectures, a better understanding of film morphology and charge transport properties, and experimentation with new materials for each layer within the cell.

OHPs have also garnered much attention among the solar cell research community due to their low material cost and potential compatibility with roll to roll printing and other mass production techniques. Numerous fabrication methods have been explored, including both one-step[10, 13] and two-step solution processing,[14] vapor assisted solution processing,[15] vacuum deposition,[16, 17] chemical vapor deposition,[18] spray coating,[19, 20] room temperature solvent-solvent extraction,[21] doctor blading,[22] and bar coating.[23] In addition to working on improving methods for large area deposition,[24] progress towards scalability is also being made through engineering perovskite solar cell modules.[25, 26]

Perovskite cells are also being incorporated into tandem cells, and may serve as a cost-effective way to boost the efficiency of conventional solar cells, considering the comparatively inexpensive capital investment required by companies with existing silicon-based solar cell manufacturing plants.[27] McMeekin et al. demonstrated the viability of a perovskite-Si tandem cell, showing the potential for a PCE over 25% for 4-terminal tandem cells.[28] Low-temperature processed monolithic tandem cells have been reported[29] and recently a PCE of over 23% was achieved for a 2-terminal all-perovskite tandem cell.[30]

With efficiencies reaching above 20% and approaching that of single crystal Si cells, there has been a change in emphasis in the literature. There is renewed effort to focus on stability and interface engineering, both seen as keys to further optimization and eventual commercialization of OHP-based solar cells. Understanding the interfaces in OHP devices requires a thorough understanding of the perovskite surface. This thesis consists of a fundamental surface science investigation of lead halide perovskites, with focuses on the nature and dynamics of defects at the $MAPbBr_3$ surface, the surface atomic structure and stability of different perovskite formulations, and the device-relevant interface between $MAPbX_3$ and copper phthalocyanine (CuPc).

1.3 OHP-based solar cell device layers

In this section, a description of the OHP-based solar cell working principle and device architectures is followed by a brief overview of each layer in the perovskite solar cell (Fig. 1.2). Photons in the solar spectrum with energy exceeding the band gap, i.e., the energy gap between the valence band maximum (VBM) and conduction band minimum (CBM), of the perovskite material can excite electrons from the filled valence band (VB) to an unoccupied state in the conduction band (CB), creating an electron-hole pair. A low exciton binding energy of 16 meV enables electron-hole pairs to efficiently separate into free carriers.[8] The perovskite layer is typically sandwiched between two charge selective layers, and the free electrons and holes migrate to the electron transport layer (ETL) and hole transport layer (HTL), respectively. In these transport layers, the electrons and holes are selectively conducted to their respective electrodes and finally to the external circuit. The standard sandwich architecture has three main variants, the planar solar cell, in which only a compact layer of material is used for the ETL, the mesoscopic architecture in which a mesoporous layer of the ETL material is deposited on top the compact layer, and the inverted architecture, in which the placement of the HTL and ETL are swapped. This mesoporous layer is employed to increase the effective contact area and thus charge transfer at the perovskite/ETL interface. The inverted cell structure, in which the HTL rather than the ETL must be transparent to the incoming sunlight, allows for experimentation with different materials not compatible with the conventional architectures.

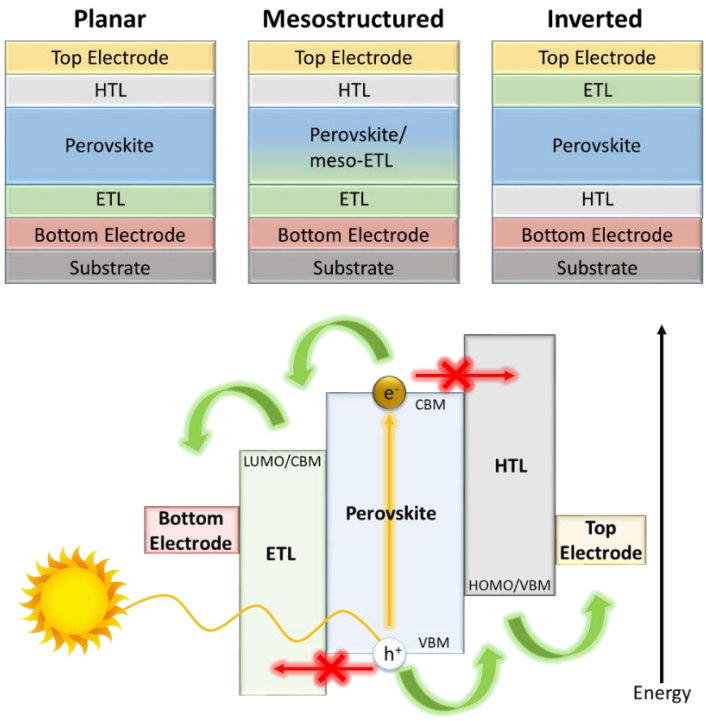

Figure 1.2 Perovskite device architectures (top) and perovskite solar cell working principle (bottom).

Substrate Layer

For a majority of studies in the literature, the substrate of the device stack is glass, which efficiently transmits incoming light to the cell. However, the compatibility of OHPs with flexible substrates is one of its key benefits, and investigation of flexible perovskite solar devices is a crucial branch of research. Perovskite cells on flexible substrates have shown an impressive 95% PCE retention after 5000 bending cycles at r=5mm[31] and an 85% PCE retention after 5000 cycles at a harsher bending of r=2mm.[32] Recently, OHP-based solar cells on 2.5μm ultra-thin substrates have been demonstrated that can achieve over 17% efficiency and withstand harsher bending (r=0.5mm) and even complete crumpling.[33]

Bottom Electrode Layer

The "bottom" electrode, thus termed as it is on the bottom of the layer stack during fabrication, actually faces the incoming solar radiation, and thus transparency is of the utmost importance to let the maximum number of photons reach the perovskite absorber layer. Although the vast majority of reports use a transparent conducting oxide (TCO), typically fluorine-doped tin

oxide or indium-doped tin oxide (FTO and ITO, respectively), as the bottom electrode, there is also interest among the flexible solar cell community to replace these materials, as they are known to be mechanically brittle. Graphene has emerged as a strong candidate replacement, with reports of both rigid[34] and flexible[32] inverted structure cells using graphene as a transparent conducting electrode that achieve a PCE of around 17%.

Electron Transport Layer (ETL)

The ETL is most commonly composed of a compact layer of titanium dioxide (TiO_2), which features a suitably large band gap, allowing visible light to transmit to the perovskite layer. It also has a favorable energy level alignment between with the conduction bands of OHP materials, which allows electrons to conduct through the layer, but blocks holes. The mesoscopic architecture adds a mesoporous layer of TiO_2 on top of the compact layer in order to improve charge extraction by increasing contact area with the perovskite active material.[35] Utilizing a mesoporous aluminum oxide (Al_2O_3) film on top of a compact TiO_2 can cause a favorable increase in V_{oc}.[11] Tin oxide (SnO_2) has also received considerable attention as an ETL, as it is compatible with low-temperature processing and has been successfully employed in large area solar cells.[36-38] The organic molecule phenyl-C61-butyric acid methyl ester (PCBM), a member of the fullerene family of compounds, has also been utilized as an ETL primarily in inverted device architectures. PCBM features a higher electron conductivity than TiO_2, is more hydrophobic, and can result in hysteresis-less cells.[39]

OHP Absorber Layer

Extensive work has been performed exploring different compositions of OHP light absorbing layer and the subsequent effect on common performance parameters such as open-circuit voltage (V_{oc}), short-circuit current (J_{sc}), fill factor (FF) and PCE, as well as material properties including band gap, carrier diffusion length, and carrier mobility. Much of this exploration has centered around substituting or mixing different elements at the A, B and X sites in the crystal.[40] It has been shown that the band gap of the active layer can be tuned by creating films with different ratios of two different halides in the X position.[41] For instance, the band gap can be tuned from 1.55 to 2.3 eV by mixing the appropriate ratio of bromine and iodine based precursors ($PbBr_2$, PbI_2, MAI, MABr). Tandem solar cells that utilize OHPs can take advantage of this tunability, as the ideal band gap for a top cell matched with a conventional Si-based bottom

cell is 1.8 eV. McMeekin et al. demonstrated the feasibility of a perovskite-Si tandem to achieve over 25% PCE by holding a semi-transparent $FA_{.83}Cs_{.17}Pb(Br_{.4}I_{.6})_3$ (band gap 1.75 eV) perovskite top cell in front of silicon solar cell and summing the PCEs.[28] The bandgap tunability also provides the benefit of enabling the creation of semi-transparent active layer thin films of varying colors, an attractive aesthetic feature for building-integrated photovoltaics.[41]

Highest efficiencies have been achieved with lead-based OHPs (Pb in the B site of the crystal structure), but tin-based OHPs have also been studied, although these are often hindered by lower efficiencies and poor stability.[42, 43] Mixing Sn into Pb perovskites can lower the bandgap to the 1.2 eV range, and this strategy was recently used in an all-perovskite tandem cell.[30] Mixing different cations in the A-site has also shown a number of benefits. Methylammonium (MA) cation in the A site is most common, but replacing MA with formamidinium (FA) cation increases the high temperature stability of the perovskite layer.[44] FA-based perovskite layers can have complications due to their amorphous delta phase for mixed halide and pure iodide films, which is not suitable for photovoltaic device use.[45] Recently, the inorganic Cs cation has also been used in the A site, and it was shown that the addition of Cs cation stabilizes the $FAPb(I_xBr_{1-x})_3$ perovskite, which normally has an amorphous phase at a I:Br ratio of 6:4.[28] Cesium was also shown to increase the stability and reproducibility of the overall device performance when mixed in a triple cation formulation with MA and FA.[46] Cs-based all-inorganic perovskite solar cells are also viable, with efficiencies reaching above 10%.[47] Rubidium is normally too small of a cation to form a stable photoactive perovskite phase, but incorporation of Rb^+ into a CsFAMA mixed cation perovskite enabled high open-circuit voltage and PCE, with impressive stability under high stress testing.[48] Incorporation of K^+ into the perovskite was shown to reduce or eliminate hysteresis in a wide variety of perovskite formulations by preventing halide Frenkel defects.[49]

There is also ongoing discussion regarding the role of excess precursor in the OHP film. Chen et al. reported evidence of reduced carrier recombination in $MAPbI_3$ films with excess PbI_2 as seen through extended photoluminescence lifetimes. It was found that a judicious amount of PbI_2 could passivate grain boundaries in the film and improve charge transport.[50] Another study found that excess PbI_2 yielded higher PCE, while PbI_2 deficient (excess MAI) samples had higher V_{oc}.[51] Excess MAI has been suggested to accumulate on the surface, reducing conuctivity,[52] while evidence has also been found for a beneficial effect of interfacial MAI.[53]

The role of grain boundaries and grain size has also been a focus of research on perovskite films. Local variation of photoluminescence (PL) intensity and lifetime was found from grain to grain. Lower PL intensities and lifetimes were measured at grain boundaries, signifying greater non-radiative recombination. Treatment with pyridine improved PL intensity at grain boundaries, which is consistent with the theory of passivation of defects at grain boundaries.[54] There is also evidence linking grain boundaries to increased ion migration.[55] Post-annealing with methylamine gas increased grain size and reduced surface impurities,[56] while a hot-casting technique was able to produce millimeter-size grains,[57] and rapid crystallization via a vacuum-flash assisted solution processing technique enabled high-quality films over a large area.[24] Numerous other fabrication techniques have been reported to improve OHP film quality and device performance, but will not be exhaustively discussed here.

Hole Transport Layer (HTL)

A wide variety of organic and inorganic materials have been shown to be suitable for creating efficient OHP-based solar cells, and a few selected materials will be highlighted here. The most commonly used HTL consists of 2,2′,7,7′-tetrakis(*N*,*N*-di-*p*-methoxyphenylamine)-9,9′-spirobifluorene (Spiro-MeOTAD) doped with 4-tert-butylpyridine (tBP) and bis(trifluoromethane)sulfonimide lithium salt (Li-TFSI). LiTSFI was found to be necessary for SpiroMeOTAD to undergo a beneficial oxygen-induced doping process,[58] and it was shown that in OHP-based cells, tBP prevents phase segregation of the LiTSFI and SpiroMeOTAD.[59] Transition metal phthalocyanines (TMPcs) have also been explored due to their relatively lower cost and superior tolerance to high temperatures compared to Spiro-MeOTAD.[60-65] The copper variant, CuPc, and its derivatives have been incorporated in perovskite solar cells reaching up to 18.8%.[66] The perovskite-CuPc interface is the subject of Chapter 5 and will be discussed in greater detail there.

Poly(3,4ethylenedioxythiophene):polystyrene sulfonate (PEDOT:PSS) is used as an alternative HTL in the inverted solar cell structure,[39] with poly(3-hexylthiophene) (P3HT)[67] or poly(triarlyamine) (PTAA)[68] also showing promise as an HTL in high-performing perovskite solar cells. Inorganic HTLs have also been widely explored due to their low cost and high stability. Both NiO_x[69, 70] and CuO_x[71] have produced efficient and stable perovskite solar cells, and many other inorganic materials have been shown to be viable HTLs.[72]

Top Electrode Layer

Au top electrodes are most common, with Ag,[73] Al,[55] and Cu[74] electrodes also being explored. The higher cost of Au and Ag electrodes is a concern for eventual commercialization. Additionally, such metal electrodes can pose problems including degradation due to AgI formation,[73] and diffusion of metal atoms into the OHP layer.[75, 76] Carbon materials are a low-cost alternative for the top electrode. Drop casting perovskite into a porous carbon film enabled a PCE of nearly 13% without the use of a HTL.[77] Multi-layer graphene electrodes have been used in combination with a thin PEDOT:PSS buffer layer[78] as well as in HTL-free architectures.[79] HTL-free cells utilizing a paintable carbon top electrode have also been reported, achieving a PCE above 14%.[80] Recently, a low-temperature processed OHP solar cell using carbon electrodes modified with CuPc was shown to boost efficiency to nearly 15%.[81]

These individual layers can have significant influence on not only the achievable PCE, but also on defect properties, ion migration, interfacial properties and stability, which are all focus areas of this thesis. An overview of these topics follows.

1.4 Defects, ion migration, and interfaces in OHPs

Part of the reason perovskite have gained so much attention is their so-called defect tolerance. The polycrystalline perovskite films used in OHP-based solar cells have a large defect concentration but are still able to achieve high efficiencies.[82] This tolerance arises from the fact that some defects only create shallow trap states, from which trapped charges can escape with relative ease.[83] Conversely, the same study showed defects with higher formation energy cause deep trap states, which can lead to non-radiative recombination and subsequent reduction of photocurrent. However, the shallow point defects are still of great relevance, as these point defects can affect performance parameters indirectly by enabling migration of ion to interfaces in a device. Surface defects on the perovskite film are also of great interest as they are present at the interface with an adjacent device layer, potentially affecting charge transfer. There has been evidence that traps at the interface are the dominant recombination loss mechanism rather than traps at grain boundaries,[84] which are sites of many defects and where ion migration occurs more readily.[55]

Ion migration in perovskite solar cells gained attention after it was first proposed as a potential reason for current-voltage hysteresis.[85] This hysteresis manifests itself as different current

output at a given voltage for the forward voltage sweep (short circuit current to open circuit voltage) and the reverse voltage sweep (Fig. 1.3). This makes it difficult to properly evaluate cell performance, and adds unpredictability that is not desirable for practical application. Understanding and suppressing ion migration is considered one avenue for controlling hysteresis.

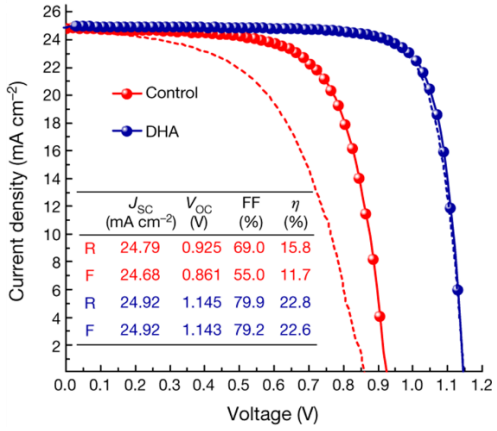

Figure 1.3 Current-voltage hysteresis. Forward and reverse scans are shown for a control sample with hysteresis (red) and a modified sample without hysteresis (blue). Reproduced from Ref. 94 with permission from SpringerNature.

Numerous theoretical and experimental studies support the existence of ion migration, although the exact nature of the ion migration, including the migration mechanism, is still a subject of debate. Halide ion migration in the perovskite absorber layer is not surprising, as oxygen vacancy-assisted ion migration within perovskite oxides is known to occur.[86] Mesoporous TiO_2/ $MAPbI_3$-based cells showed evidence of two types of stored charge, one of which decays on a large timescale and was attributed to mobile ions.[87] It was also purported that ions migrating in the material could create an internal electric field that screens the applied bias potential, causing hysteretic behavior.[88]

Such ion migration was proposed to occur via vacancy defects. The hopping rate of iodide vacancies (V_i) has been calculated, showing they can diffuse quickly.[89] A study by Azpiroz et al. reported an exceptionally low activation energy (E_a) of 0.08 eV for V_i migration, and an E_a of 0.46eV for methylammonium vacancies (V_{MA}) in $MAPbI_3$.[90] In comparison, Pb ions have been ruled out as a mobile species due to their comparatively high E_a of 2.31 eV.[91] However, widely varying activation energies have been obtained for the migration V_i and V_{MA}, utilizing a number of theoretical and experimental techniques. Activation energies for V_i migration range from 0.08-

0.58 eV and values for V_{MA} migration range from 0.46-1.12 eV.[89-96] From these studies, ion migration via halide vacancies seems likely. However, migration of the MA cation is also viable, and a photo-thermal induced resonance microscopy study showed MA cation motion.[97] Additionally, Domanski et al. attributed a slow timescale reversible performance loss to MA cation migration based on measurement of current transient dynamics and theoretical modeling.[98] In another study, the mechanism of ion migration was evaluated theoretically, and it was found that an interstitial mechanism is preferred for MA cation migration, while for iodide migration there was little energetic difference between an interstitial mechanism and a vacancy-assisted mechanism.[99] It was also proposed that methylammonium vacancies could provide a path due to less steric hindrance.[100]

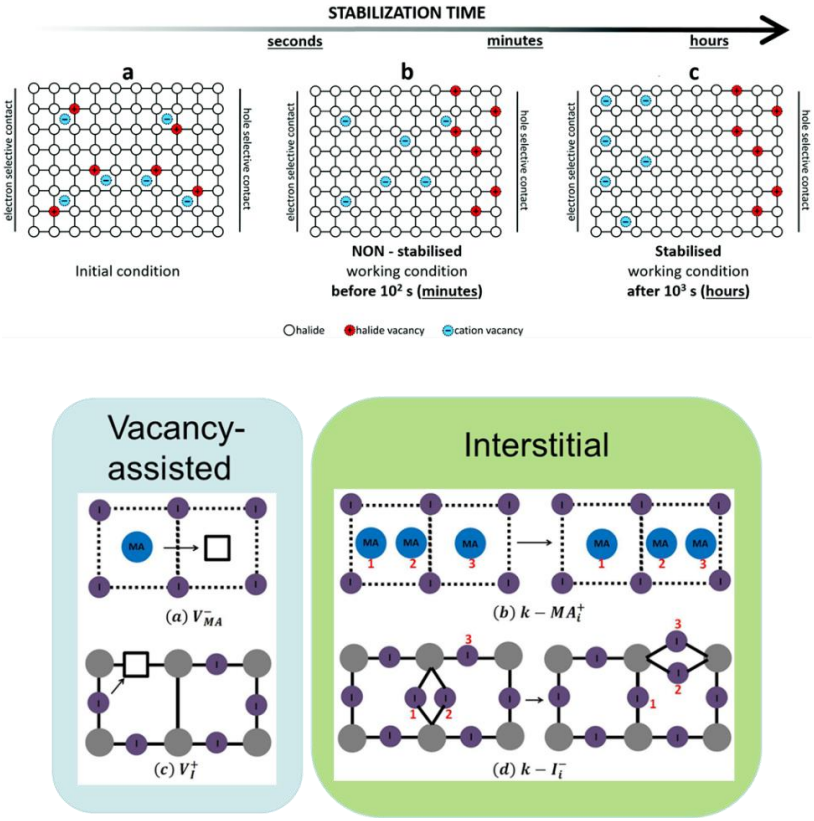

Figure 1.4 Ion migration in perovskite solar cells. (Top) Schematic for vacancy-assisted ion migration, detailing proposed different timescales for MA cation and halide migration. Reproduced from Ref. 107 with permission from The Royal Society of Chemistry. (Bottom) Schematics for possible mechanisms of ion migration in OHP materials. Reproduced from Ref. 108 with permission from The Royal Society of Chemistry.

Iodine ions were shown to move through the perovskite film via an XPS study where spectra were taken at different locations on a lateral OHP device both before and after biasing the device at 1 V for 30 min. The ratio of I/Pb near each electrode was different after biasing, showing an increased presence of I^- ions at the positive electrode.[101] Studies attempting to clarify the nature of ion migration tend to focus on $MAPbI_3$, however, a study of mixed Br/I perovskite shows bromine substitution into $MAPbI_3$ suppresses hysteresis, both experimentally, via transient photocurrent measurements performed after pre-biasing at different voltages and for different durations, and theoretically, via DFT calculations.[102] Activation energy of V_i migration increases by 30% in simulation of $MAPb(Br_{0.1}I_{0.9})_3$ compared to that in $MAPbI_3$. It was also calculated that iodide vacancy formation energy is 80% greater in the mixed perovskite, resulting in fewer defects. In addition to the negative effects detailed below, ion migration is especially important for mixed halide perovskites for its potential role in the phase segregation that has been observed under illumination.[103-105]

In general, better understanding and control of ion migration is crucial as it has multiple implications for device performance. Accumulation of ions at interfaces in a device can cause band bending,[90, 106] which can affect charge transfer to the HTL or ETL. Chemical interaction between the halide ion of the perovskite layer and the selective contacts has been proposed as a cause of hysteresis[107] and gradual deterioration of performance.[108] It has also been shown that halide species can cross the HTL to degrade the metal electrode.[73] These interactions could be exacerbated by increased concentration of ions at the interface due to ion migration, thus linking ion migration to stability.

A major strategy for solving the issues related to defects, ion migration, and hysteresis has centered around the concept of defect/surface passivation.[109] Sites of unbalanced negative charge, such as undercoordinated halide ions or cation vacancies (e.g. V_{MA}), can be passivated by Lewis acids or additive cations. PCBM can act as a Lewis acid and has been shown to reduce or eliminate hysteresis.[39, 57, 110, 111,] Another Lewis acid, iodopentafluorobenzene, was shown to passivate undercoordinated iodide at the OHP surface that act as hole traps at the OHP/HTL interface.[112] Incorporation of Na^+ and K^+ into the perovskite was suggested to passivate cation vacancies or undercoordinated halides at grain boundaries,[113, 114] while another study attributed the performance improvement from K^+ incorporation to its ability to occupy interstitial sites and prevent Frenkel

defects.[49] Conversely, sites of excess positive charge, such undercoordinated Pb cations or halide vacancies, can be passivated by Lewis bases or additive anions. Molecules that feature a lone pair of electrons on nitrogen,[115] sulfur,[116] or oxygen[117] functional groups have been successfully employed to passivate perovskite surfaces. Cl anions have been shown to increase charge carrier lifetimes[118] and a theoretical study shows Cl incorporation can heal deep trap states caused by Pb or I vacancies.[119] The success seen via surface and defect passivation underscores the importance of understanding the perovskite surface and its contribution to charge transfer properties at the interfaces of devices.

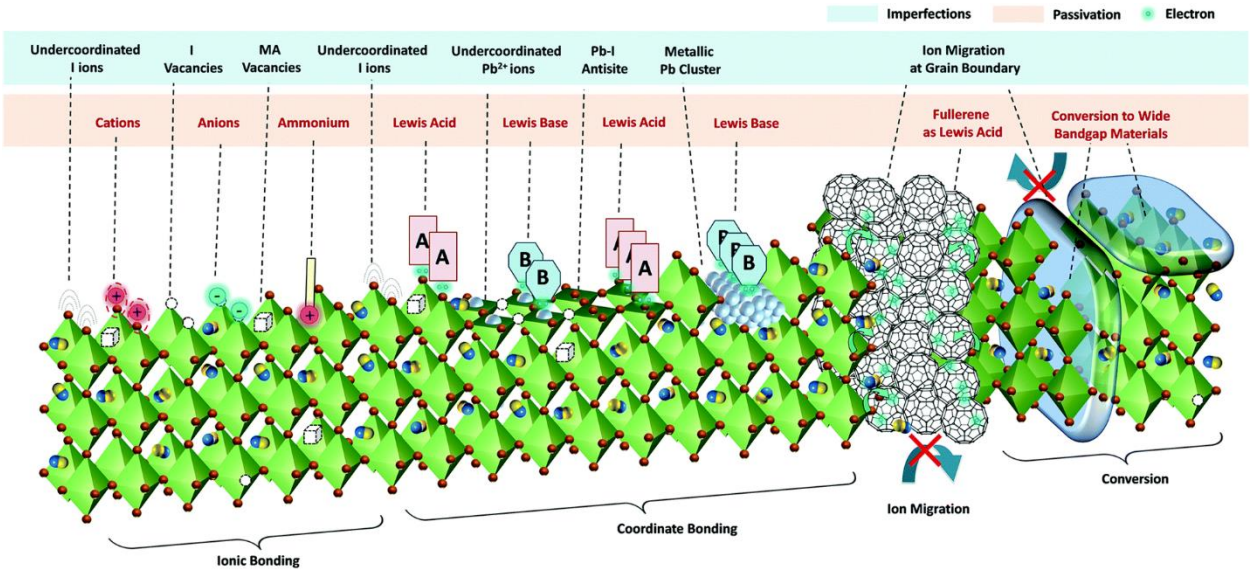

Figure 1.5 Surface and defect passivation in lead halide perovskite materials. Reproduced from Ref. 117 with permission of The Royal Society of Chemistry.

The interfaces themselves have also been the subject of extensive investigation,[120, 121] with the concept of energy level alignment between adjacent layers often discussed in the context of charge transfer efficiency. Wang et al. performed UPS measurements on various OHP-HTL interfaces and summarized the various types of energy level offsets that are possible, concluding that HTLs with a Type I interface, such as spiro-MeOTAD, are preferable as this type of interface blocks the opposite charge carriers.[122] A study comparing $MAPbI_3$ solar cell performance for different HTLs found the best performance with HTLs that had an ionization energy (IE) equivalent to that of the perovskite.[123] However, there is evidence that, within a certain range, the IE of the HTL doesn't significantly affect solar cell performance parameters.[124, 125] For some OHP

preparation methods, it was found using HTLs with sufficiently large IEs leads to lower J_{sc} due to the formation of a hole extraction barrier.[125] Such discrepancies in the literature have been attributed to differences in perovskite film preparation methods,[121] and it should be noted that discrepancies exist between studies on OHP-ETL interfaces as well.[126, 127] Additionally, it has been shown that different precursor ratios for the OHP film can result in different energy level alignments for the C_{60}-$MAPbI_3$ interface.[128] Finally, further convolution can occur when using organic molecules as charge transport layers, as it has been shown the orientation of an organic molecule can alter interfacial properties.[129]

1.5 Stability of OHP materials

The issues discussed in the last section are also related to the stability of perovskite materials, which constitutes a major hurdle towards commercialization of OHP-based technologies. OHP-based solar cells are known to be sensitive to environmental factors including moisture, oxygen, high temperature, and UV radiation. Zhou et al. compared devices stored in dry air or under nitrogen with those stored in ambient air. After 24 hours of storage, the dry or nitrogen stored samples retained 80% of their PCE, whereas ambient air samples only retained 20%, highlighting the need for more robust materials and device architectures.[130]

Improvement of device stability requires a thorough understanding of what contributes to degradation of OHPs. Degradation mechanisms involve precursor (PbX_2 and MAX) formation in the film, which can be triggered by a number of factors, including high temperature and moisture. It has been proposed that in the presence of moisture, aqueous MAI can dissociate into methylamine and hydrogen iodide (HI), which is made favorable by the evaporation of methylamine gas and the breakdown of HI upon exposure to O_2 and UV radiation.[131, 132] Additionally, both monohydrate and dihydrate complexes form in the perovskite film upon exposure to moisture, which can lead to precursor formation and the degradation mechanism mentioned above. The hydrate formation is reversible for low humidity, but there exists a threshold humidity level beyond which the hydration becomes permanent.[133, 134]

Oxygen can also cause degradation of the perovskite, and multiple pathways have been suggested. For instance, ambient O_2 can react with oxygen vacancies in TiO_2 to form a superoxide radical (O_2^-), which can cause degradation.[135] Light, especially UV irradiation, has also been

identified as a cause of degradation, and it has been suggested that perovskite may decompose differently in light and dark.[136] A combination of light and oxygen was shown to degrade OHP-based solar cells quickly, and evidence showing degradation in the absence of light but with applied bias implies that oxygen interacting with excited electrons to form O_2^- is the initial degradation step.[137] Additionally, oxygen infiltration into the perovskite bulk was shown to be enabled and enhanced by progressively stronger irradiation with light. Mixing FA/MA cations was able to suppress this phenomenon, providing additional insight into the superior stability reported for mixed cation formulations.[137] Also, the UV range of the solar spectrum can provide additional complications, triggering the well-known oxidative photocatalytic properties of TiO_2 leading to degradation at the ETL/OHP interface.[138]

Improvements in stability have been shown by using mixed halide and mixed cations formulations. Incorporation of Br into the X site has been shown to improve moisture stability,[139] while FA incorporation into the A site has been shown to improve thermal stability.[44] A pair of studies led by Michael Saliba show stable performance from perovskites with a small fraction of Cs or Rb added.[46, 48] However, the stability tests for these studies were done in nitrogen atmosphere. Other studies tested stability in humid atmosphere and found that perovskite formulations containing Rb are not as moisture stable as those utilizing Cs or K cations.[140, 141] A recent study utilizing a sodium fluoride (NaF) additive shows significant improvements over reference CsMAFA triple cation perovskite, retaining 90% of its original PCE after 1000h.[142] Another strategy for improving stability consists of the introduction of much larger organic cations to form mixed-dimensional 2D/3D perovskite materials. The increased hydrophobicity of the long carbon chain of these cations confers improved device stability, as evidenced by an impressive stability test maintaining 12% PCE for over 10,000h under illumination and ambient conditions.[143] Use of tetraammonium zinc phthalocyanine to form 2D perovskite at grain boundaries significantly improved moisture and heat stability.[144] Judicious choice of HTL/ETL can also improve stability. For instance, utilizing more thermally resilient HTLs can increase stability,[145] as can engineering increased hydrophobicity[146] or lower UV photocatalytic activity[147] in the ETL.

Overall, such efforts have led to multiple groups reporting devices exceeding 1000h of stability under constant illumination for high efficiency (>20% PCE) devices.[142, 147-149] Although

OHP cells can now last on the order of thousands of hours, much work is still needed to approach the stability of Si-based cells currently on the market.

1.6 Scanning Tunneling Microscopy (STM) on OHPs

The device-related background discussed in the previous sections provides important context for the work in this thesis, but a detailed summary of initial scanning tunneling microscopy (STM) studies on perovskite is also important for understanding the results discussed in later chapters. Ohmann et al. published the first real-space, atomic resolution images of a OHP surface, employing STM imaging on *in situ* cleaved single crystal $MAPbBr_3$.[150] This was followed quickly by an STM study from She et al. detailing the surface of $MAPbI_3$ thin films.[151] Both studies found similar results, with the surface reconstructions observed on $MAPbBr_3$ closely resembling those observed on $MAPbI_3$. Both surfaces are terminated with an MA-X containing layer, rather than a Pb-X containing layer. The two different reconstructions were found to originate from the relative orientation of the MA cations in the perovskite lattice. The "zig-zag" reconstruction occurs when the MA cations are oriented perpendicular to one another (Fig. 1.6a and b), while the "paired" reconstruction occurs when the MA cations are oriented anti-parallel to each other (Fig. 1.6c and d). The pairing of the halide ions occurs due to electrostatic attraction to the partial positive charge at the nitrogen end of the MA cation's dipole. Conversely, there is a larger spacing between adjacent pairs of Br anions due to interaction with the partial negative charge on the carbon end of the MA cation. Density functional theory (DFT) calculations found that the "paired" reconstruction was 0.51 eV lower in energy per unit cell than the "zig-zag" domain.[150] It is important to note that even though MA^+ is present in the surface layer, it is rarely resolved in STM images because the density of states (DOS) of the MA cation does not extend into the vacuum as much as the DOS of the halide ions.[150]

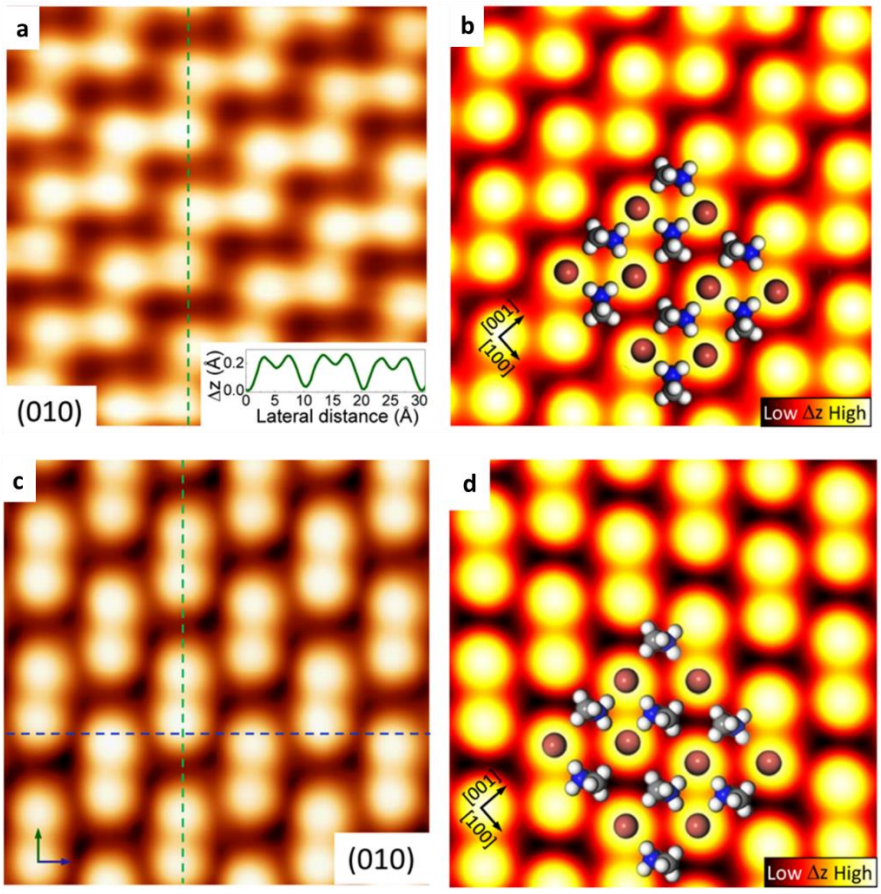

Figure 1.6 Surface reconstructions of $MAPbBr_3$. STM images of the "zig-zag" (a) and "paired" (c) reconstructions of the $MAPbBr_3$ surface and their corresponding simulated STM images calculated by DFT (b,d respectively). Br anions appear as bright protrusions. Color code for overlay in (b,d): N (blue), C (gray), H (white), Br (brown). Reprinted in part with permission from Ref. 2 under the *ACS AuthorChoice* Usage Agreement. Copyright 2015, American Chemical Society.

Other STM studies have looked at precursor depositions and the $MAPbI_3$ growth process,[152] and complex patterns were observed for a possible monolayer of $MAPbI_3$ on Au(111).[153] A particularly interesting study by Hsu et al. observed a drastically different $MAPbBr_3$ surface structure when the sample was illuminated.[154] This was attributed to a photodriven rearrangement of the dipoles of the MA cations, and resulted in the creation of one-dimensional potential wells that could help explain the long carrier lifetimes in OHPs. This study also reports imaging a Pb-Br terminated surface, whereas previous studies have only observed MA-Br terminated surfaces. The number of STM studies is still severely limited, but this technique can

provide rich information about perovskite surfaces, which, as discussed in Sections 2.3 and 2.4, play a key role in device performance and stability.

1.7 Overview of Copper Pththalocyanine (CuPc)

Chapter 5 will discuss the device relevant interface between $MAPbX_3$ perovskites and CuPc, so here a brief description of the CuPc molecule, its appearance in STM, and its polymorphic nature is provided. CuPc is widely used as a pigmentation molecule in industry, and is also of fundamental interest for probing unique spin properties.[155] In the context of OHP-based solar cells, CuPc and its derivatives are utilized as HTLs.[60, 63, 66, 156] The CuPc molecule itself consists of a Cu atom sitting at the middle of an organic phthalocyanine ring, which constitutes a conjugated π-orbital system enabling facile charge transport. This conjugated system is made up of four isoindole groups (i.e. a fused benzo-pyrrole group) connected by nitrogen atoms. CuPc has been widely studied by STM, including studies on metal-molecule contacts[155] and organic-organic heterojunctions.[157] This makes CuPc a suitable choice as an entry point for studying a perovskite-HTL interface via STM. The appearance of CuPc can vary significantly depending on the underlying substrate and the imaging parameters chosen. CuPc often appears as four-lobed cross shape (Figs. 1.7b,d) resembling its geometric shape, but it is also possible to image molecular orbitals with the right imaging parameters and a relatively weak interaction between CuPc and the substrate (Figs. 1.7a,c). For higher coverages, self-assembled (SA) layers form, with a variety of patterns and dimensions observed in the literature,[158-160] two of which are depicted below (Figs. 1.7d,e).

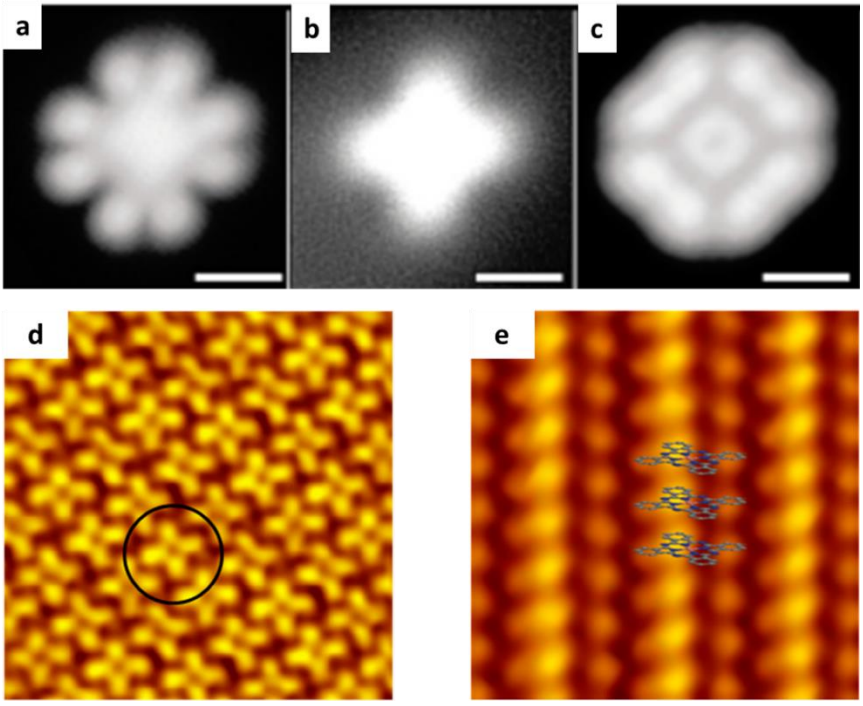

Figure 1.7 STM images of CuPc molecules and self-assembled (SA) layers. a-c) STM images of an individual CuPc molecule in its HOMO state, in-gap state, and LUMO state, respectively. Adapted with permission from Ref. 163. Copyright 2013 American Chemical Society. d) First layer of CuPc on Bi(111), showing a flat-lying orientation. e) Second layer of CuPc on Bi(111), showing an upright orientation. Figs. d and e adapted from Ref. 166 under a Creative Commons Attribution 4.0 license.

The polymorphic nature of CuPc is also worth covering as a primer for some of the discussion in Chapter 5. The exact number of distinct polymorphs is somewhat unclear, with differing accounts in the literature.[161, 162] However, there are only intermolecular stacking models in the literature for two polymorphs (Fig. 1.8),[163] the metastable alpha phase (α-CuPc) and the thermodynamically stable beta phase (β-CuPc). Each polymorph has a distinct "stacking angle", which is depicted below as the angle between the normal of the molecular plane of the CuPc molecule and the macroscopic direction of one row of CuPc molecules (b-axis, Fig. 1.8). However, for easier analysis and discussion of STM images in Chapter 5, I will be redefining the stacking angle as angle between the b-axis and the CuPc molecular plane (rather than its normal). Using this definition and the values in Figure 1.8, stacking angles of 63.5° and 44.2° are obtained for α-CuPc and β-CuPc, respectively. It is also important to note there are different intermolecular spacings along the b-axis for these two polymorphs. Finally, β-CuPc is shown with alternating molecular orientation, while for α-CuPc the CuPc molecules are shown as all parallel.

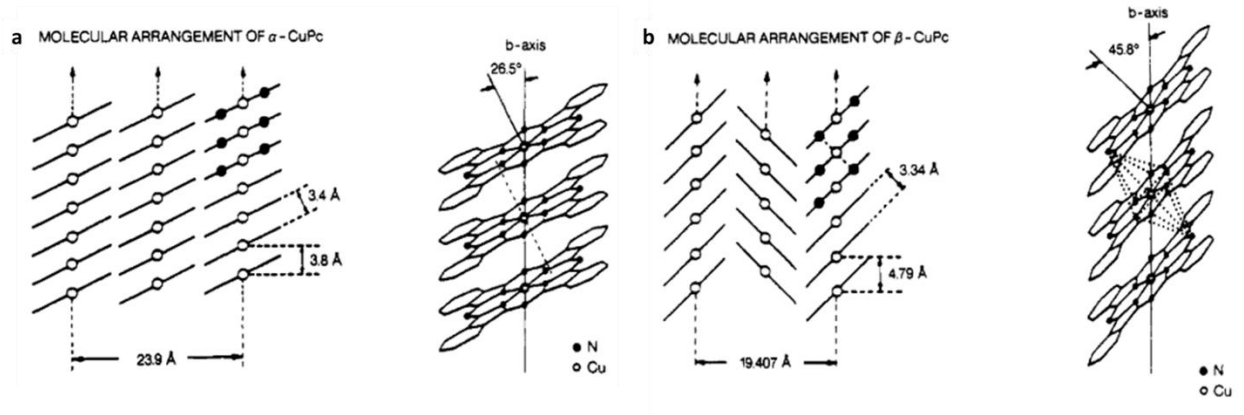

Figure 1.8 Stacking arrangements of α-CuPc and β-CuPc. Schematics showing the intermolecular stacking of CuPc molecules in the α-CuPc (a) and β-CuPc (b) polymorphs. Reproduced from Ref. 169. Copyright 1978 Oil & Colour Chemists Association.

Chapter 2: Instrumentation and Methods

2.1 Ultra-high vacuum (UHV) system

In this thesis, unless otherwise stated, an ultra-high vacuum (UHV) system was utilized for sample preparation and analysis in order to obtain atomic resolution images of the pristine lead halide perovskite surface. A combination of turbo molecular pumps, ion pumps, and titanium sublimation pumps were used to achieve a base pressure in the range of 10^{-10} to 10^{-9} torr. A turbo molecular pump (backed by a roughing pump) was used to pump down the chambers from atmospheric pressure. In order to obtain a UHV environment, the chamber was heated to 100-120°C for at least 48 hours while the pump ran. After this bake out procedure, UHV pressures were achieved. In order to reduce vibrations during STM image acquisition, pumping was switched from the turbo pump to an ionic pump. Titanium sublimation pumps were used as needed to recover a low base pressure, especially after deposition trials, which unavoidably increased pressure in the system by a nominal amount. Maintaining a UHV environment was important because exposure of a sample to atmospheric pressure (760 torr) results in adsorption of contaminants from ambient air that can cover the surface of interest and complicate the acquisition of atomic resolution images. The experimental setup used in this thesis has sample preparation chambers, a scanning tunneling microscope (STM), and a photoelectron spectroscope (PES) connected in the same UHV system (Fig. 2.1). This allowed for samples to be prepared and subsequently characterized by multiple techniques without exposing the sample to contamination at higher pressures.

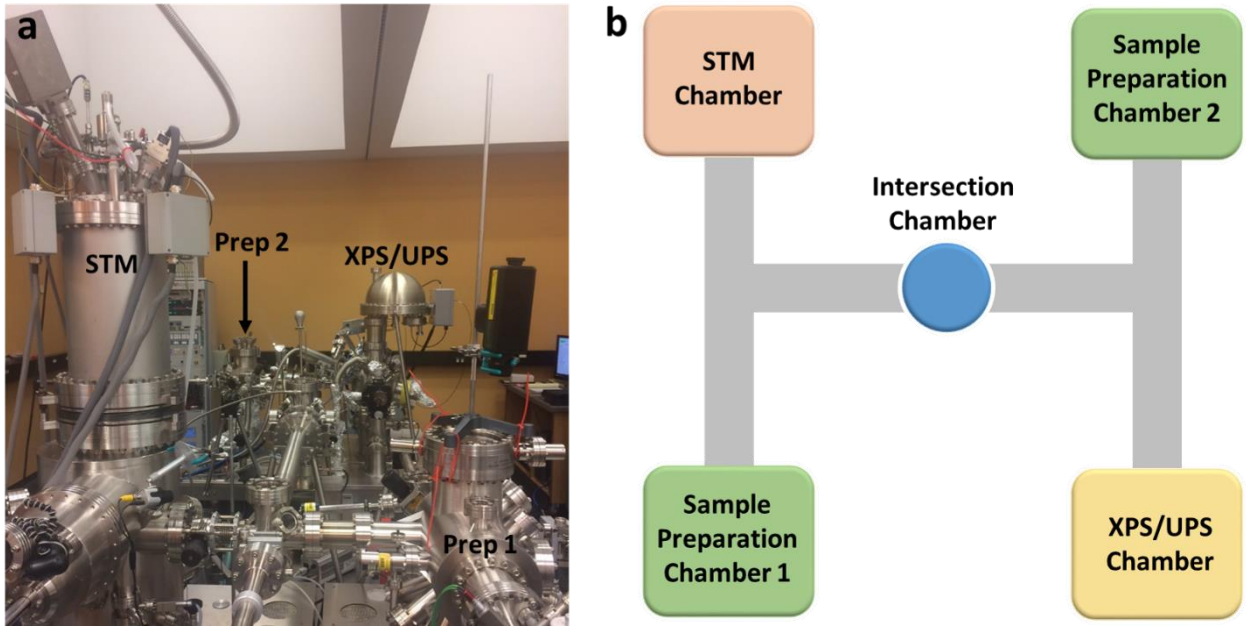

Figure 2.1 UHV System Overview. a) Photograph of the UHV system used in this thesis. b) Diagram showing the layout of the various sample preparation and analysis chambers. All chambers are connected in the same UHV system.

2.2 Perovskite Sample Preparation

Two different methods were used for preparing perovskite samples for STM imaging. One method utilized single crystals, while the other involved creating thin-films. Single crystal samples were grown using a solvent exchange method previously reported in the literature.[164] A vial containing an equimolar solution of lead bromide ($PbBr_2$) and methylammonium bromide (MABr) in dimethylformamide was placed inside a larger vial filled ⅓ to ½ full with isopropyl alcohol and sealed with paraffin film. After 2-3 days of storage at ambient temperature, methylammonium lead bromide ($MAPbBr_3$) crystals of a few mm in dimension were formed. The grown crystal was carefully carved into an L-shape or T-shape, loaded onto an STM sample plate, and fixed in place with a metal top plate that had a hole cut into it to allow part of the crystal sample to protrude. The sample was loaded into the UHV system and the protruding crystal was physically cleaved with a scalpel *in situ*, producing a pristine surface for characterization.[150]

For ultra-thin film deposition, Knudsen cell (K-cell) evaporators attached to the UHV sample preparation chamber were used. Before attachment, these are loaded with a crucible containing perovskite precursor materials, such as PbX_2 or MAX, where X= Br, I or Cl. A

thermocouple near the crucible was used to monitor the temperature and a water cooling feedthrough in the K-cell was used to prevent overheating. Precursor materials were degassed by heating them to their respective evaporation temperatures prior to use in any perovskite film depositions. Perovskite thin films were deposited onto Au(111) single crystal substrates, which were cleaned in UHV by 3-4 cycles of either Ar^+ or Ne^+ ion sputtering followed by annealing at 773 K for 5-10 min. The effectiveness of this cleaning protocol was checked via XPS survey scan showing no contamination peaks and STM imaging showing the typical herringbone reconstruction of the clean Au(111) surface. The cleaned Au(111) substrate was stored in an intersection chamber in the UHV system while the precursor materials were heating. Approximately 30 min before deposition, the sample stage was cooled to 130 K, using a feed-through tube and N_2 gas that had been cooled by running it through a copper coil submerged in liquid nitrogen. Once the stage was cooled and the precursor molecules had thermalized at the desired deposition temperature for at least 5min, the clean Au(111) substrate was transferred from the intersection chamber to the cooled stage. Cooling the stage was important for increasing the sticking coefficient of the MAX molecule. After the sample was in the correct position, the shutters on the precursor molecule K-cells were opened simultaneously, starting the co-deposition. After the desired deposition time, typically 3-10 minutes, the K-cell shutters were closed and the sample was transferred back to the intersection chamber. The sample was allowed to anneal at room temperature for at least 3h before transferring it to the cooled STM stage for imaging. Allowing the film to warm up to room temperature was found to enable the two precursor molecules to move around and react thoroughly, aiding in perovskite film formation. During the deposition, conditions were monitored via quartz crystal microbalance (QCM). Due to the non-directional evaporation of the MAX precursor compounds[16] and resultant cross-talk in QCM signals, absolute flux during the deposition and absolute thickness values for the resultant perovskite films were not obtainable. Nonetheless, these values were used to monitor consistency of the deposition protocol. QCM readings were also utilized during initial determination of appropriate heating parameters, typically targeting a low flux of 0.01-0.02Å/s for PbX_2 precursors.

The UHV system used was not equipped with conventional bulk characterization techniques such as x-ray diffraction (XRD). The ultrathin nature of the film samples not only complicates measuring an appreciable signal with XRD, but also leads to quick degradation once removed from the UHV chamber. In lieu of measuring the ultrathin film samples, XRD was

performed on an $MAPbBr_3$ crystal sample ground into a fine powder. The obtained XRD spectrum (Fig. 2.2) shows peak positions consistent with reports in the literature.[165, 166] STM images show the same surfaces reconstructions for the $MAPbBr_3$ crystal samples and for the ultrathin films,[150, 167, 168] leading to the conclusion that the ultrathin films are also indeed $MAPbBr_3$.

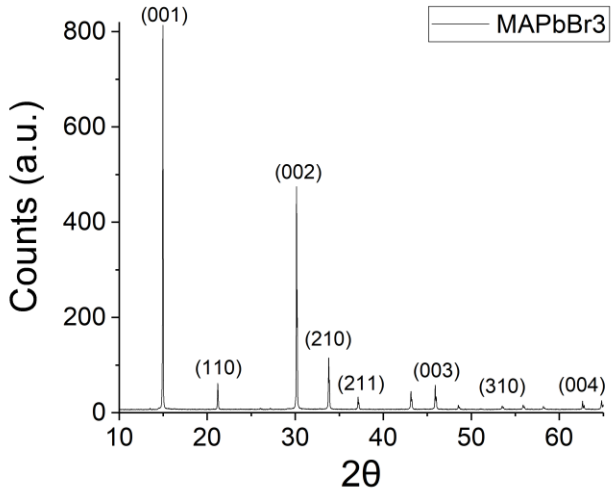

Figure 2.2 Powder XRD spectrum of the $MAPbBr_3$ crystal sample. All peaks present in the spectrum can be assigned to crystal directions in $MAPbBr_3$. Only select peaks have been labeled to maintain figure clarity.

For Chapter 3, a combination of single crystal and thin-film samples were used. For Chapters 4-6, only thin-film samples were used. Thin-films proved to be more reliable to image, as the underlying Au(111) substrate allowed for better conduction of tunneling electrons. Also, the tip was easier to recover after a tip crash on the thin film as opposed to the single crystal sample.

2.3 Scanning Tunneling Microscopy (STM)

STM was first developed in 1982 by Binnig and Rohrer.[169] For this technique, a bias voltage is applied between an atomically sharp metallic tip and the sample. When the tip is brought within a few angstroms of the sample, electrons are able to tunnel through the vacuum barrier (Fig. 2.3). The tunneling current is exponentially dependent on the tip-sample distance (i.e. the barrier width), and this current is used to obtain topographical and electronic information with subatomic resolution. Such a resolution is made possible because (1) the tip is atomically sharp and (2) the tunneling current is exponentially dependent on the tip-sample distance. This enables the

visualization in real space of atomic resolution details regarding intrinsic defects and structural changes at the interface.

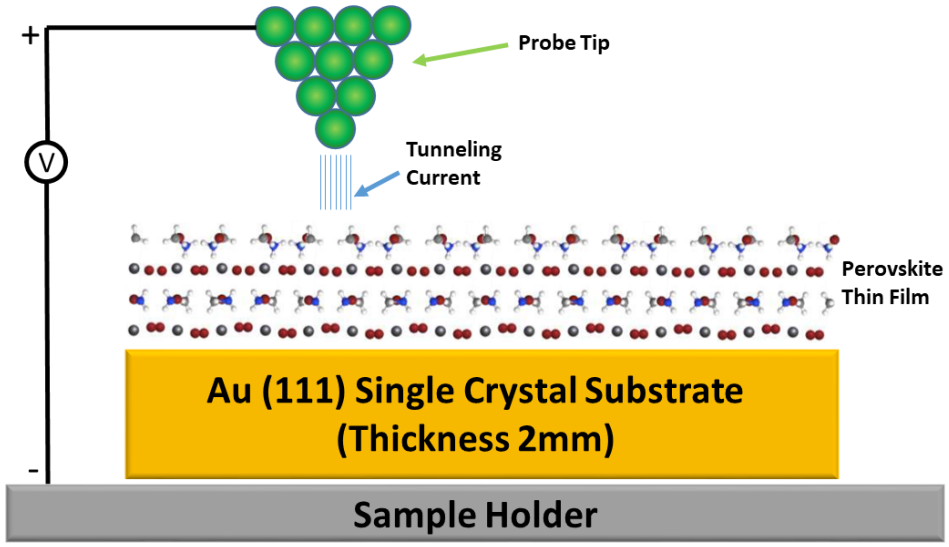

Figure 2.3 Diagram of STM measurement of a perovskite film.

The STM setup used was manufactured by Omicron, utilizing the MATRIX software package for image acquisition. Cut Pt/Ir tips purchased from Bruker were pinched into a proprietary tip holder, which could then be mounted onto the piezoelectric scanner of the STM. Piezoelectric materials expand or contract when a voltage is applied to them. Multiple electrodes attached to the piezoelectric scanner allow for sub-nanometer movement in three dimensions. Imaging for this thesis was done in constant current mode, in which a feedback loop controls the voltage applied to piezoelectric scanner in the z-direction. This adjusts the position of the tip to maintain a constant tunneling current. The tip position is recorded and creates an image where changes in contrast correspond to changes in charge density. Control of the piezoelectric scanner in the x and y directions is done through the MATRIX software. The STM was operated under UHV (10^{-10} torr) conditions. Imaging was typically performed at low temperatures, using either liquid helium (4.5 K) or liquid nitrogen (77 K) for cooling. In Chapter 3 a Lakeshore 335 Temperature Controller connected to the STM stage was used for counter heating to achieve temperatures ranging from 4.5 K to 290 K.

2.4 Photoelectron Spectroscopy (PES)

PES is a characterization technique based on the photoelectric effect, first observed by Heinrich Hertz in 1887 and later explained theoretically by Albert Einstein in 1905. In this technique, the sample is bombarded with photons of a given energy. Electrons in the sample material absorb an incident photon's energy and a fraction of them escape the surface of the material with some amount of kinetic energy (Fig. 2.4). Electrons that escape the material are collected by a detector after passing through a hemispherical analyzer which is able to select for electrons of a given kinetic energy via electrostatic input lenses and by applying a given voltage between two hemispherical surfaces in the analyzer. Electrons that escape the sample material without any collisions make up the main photoemission peaks. Other electrons experience inelastic collisions with other atoms in the material before they escape. These so-called secondary electrons lose a significant portion of their initial kinetic energy and appear as a background signal in PES spectra.

In this thesis, both X-ray and ultraviolet photoelectron spectroscopy (XPS and UPS, respectively) are utilized. PES techniques are surface sensitive and the exact probing depth depends on the radiation source used and the material being measured. Probing depth can be estimated according to a universal curve of the inelastic mean free path (λ_{IMFP}) vs. electron energy, where probing depth is taken to be $3\lambda_{IMFP.}$ For XPS, the probing depth can reach up to approximately 10 nm, while UPS is even more surface sensitive, with a typical probing depth of 1-2 nm.

Depending on the energy of the incident radiation, different energy levels of the material can be investigated. XPS can probe the core levels of a material, providing information about the identities, relative ratios, and chemical states of different elements present in a sample. An Omicron system producing magnesium K_α X-rays (1253 eV) was used for all XPS measurements. In this thesis, changes in the chemical states seen in XPS over time were used as an indicator of material degradation, and thus a measure of stability. Additionally, during optimization of co-evaporation parameters, chemical ratios from XPS were used as an initial check of sample quality. In the literature, XPS has been utilized to examine chemical composition and electronic structure of OHP materials. $MAPbI_3$ film formation,[170] the dependence of the OHP electronic structure on

the halide ion,[171] ion migration,[101] and the electronic structure of perovskite-ETL interfaces[172] have all been investigated with XPS.

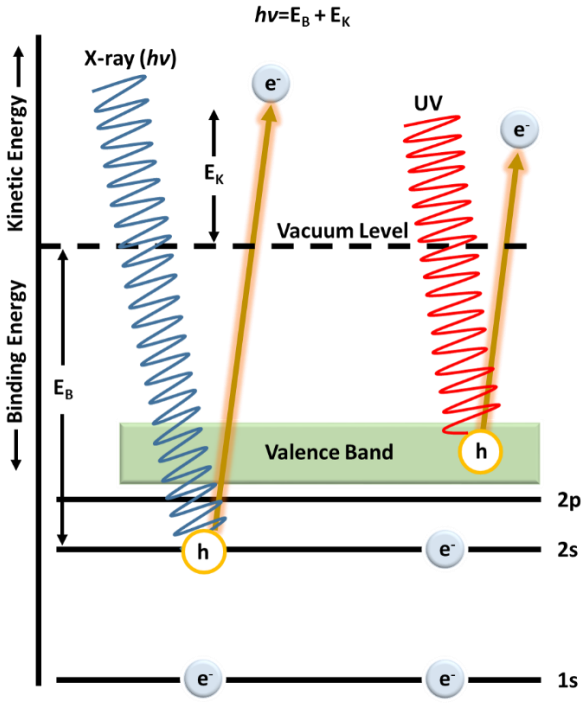

Figure 2.4 Operating principle of PES. X-ray (UV) radiation extracts an electron from the core level (valence band) of the material. The kinetic energy of the ejected electron is measured by a detector and can be used to calculate the electron's binding energy.

UPS was primarily used for valence band analysis, and also for determination of the material work function by analyzing the cutoff of the secondary electron background signal. A helium discharge lamp providing radiation of 21.21 eV was used for all UPS measurements. Understanding changes in the valence band and work function are important for energy level matching at the interfaces within the solar cell, which determines charge transfer efficiency to the external circuit.

2.5 Note on theoretical support from collaborators

Theoretical support was provided by collaborating theory groups that utilize density functional theory (DFT) calculations to predict crystal structures and simulate STM images. DFT

is a computational method widely used in the fields of materials science, physics and chemistry to calculate the electronic structure of many-body systems. As suggested by the name, DFT utilizes functionals of the electron density of the system to identify the system's ground state. DFT approaches many-body problems by treating the system as many one-body problems. For example, DFT treats a system with x electrons as x different systems with one electron each. Various approaches exist for approximating the interaction (i.e., the exchange and correlation) of these one-electron systems, and improving these approximations is a topic of current research. Common approximation methods include the local density approximation and the generalized gradient approximation. DFT calculations have been used previously to provide theoretical support that aids in the interpretation of results from STM studies on perovskite,[150, 151] and are utilized in a similar fashion in this thesis. Details of the theoretical methods used by the collaborating groups will not be discussed here. However, details can be found in the respective publications.

Chapter 3: Defects at the $MAPbBr_3$ surface and their dynamics[168]

3.1 Introduction

Based on the literature reviewed in sections 2.3 and 2.4, the importance of defects, ionic dynamics within the perovskite film, and interfacial properties is clear. Defects are often discussed in the context of bulk defect densities, which have been shown to have important relevance to device performance [111, 173, 174] and stability.[175] However, taking into account their role in interfacial properties, studies focusing specifically on surface defects are also of great importance. This can be seen by the surge of research into defect and surface passivation engineering as a strategy for improving performance.[176-180] Different types of defects have been proposed to co-exist in OHPs, such as (i) cation-vacancies (e.g., Cs+, MA^+, FA^+, etc.),[179] (ii) halide-vacancies (e.g., I^- and Br^-) leading to exposure of under-coordinated Pb^{2+} ions,[177-180] (iii) metallic lead (Pb^0),[176] (iv) halide-excess (e.g., I_2)[181, 182] and (v) anti-site PbI_3^- defects.[110]

Traps can be caused by defects in the crystal lattice, at the perovskite grain boundaries, and/or at the interface between the perovskite layer and adjacent layers,[183] thus understanding the nature of these defects is of great importance for further device optimization and stability improvement.[83, 175] Understanding the behavior and effect of surface defects is especially important because the perovskite surface comprises half of the interface in a device. Additionally, density functional theory (DFT) results have shown that Frenkel defects (e.g., Pb^{2+}, I^-, Br^-, MA^+) lead to both deep and shallow trap states in OHPs,[92, 184-186] while Schottky pair defects (e.g., PbX_2 vacancies and MAX vacancies) do not generate trap states within the band gap.[187] Intrinsic vacancy defects have also been suggested to provide pathways for both cations and anions to move within OHPs.[91, 97, 98, 188] This ion migration phenomenon has been implicated as a possible cause for material degradation and current-voltage hysteresis.[85, 189] Although evidence supporting ion migration in perovskite films and devices has been reported,[101, 190-192] the exact chemical nature of the defects, the mechanism of ion migration, and how this motion affects the local structure, are still unclear.

Adapted and reproduced with permission from Ref. 170. Copyright 2019, American Chemical Society. DFT calculations performed by collaborators in Prof. Guofeng Wang's group at The University of Pittsburgh.

Surface defects are of particular interest since they may have a direct impact on charge transfer properties at the interface between the perovskite film and adjacent layers in a device, typically a charge selective layer or an electrode. Interfaces are thought to be a major site of charge recombination,[193] and understanding how their structure affects charge transfer is essential for establishing rational interface engineering strategies. As described in Section 2.5, STM has been demonstrated to be an ideal tool to study the atomic structure and stability of the surface of OHPs,[150, 151, 154] and it is also a suitable tool for studying dynamics at the atomic scale.[194] STM studies have resolved defects in the perovskite crystal lattice for both $MAPbBr_3$ and $MAPbI_3$,[150, 151] and theoretical studies have been performed to address the migration of the intrinsic defects[90] and to simulate their appearance in STM.[90, 195] In particular, a theoretical study showed that for $MAPbBr_3$ the defects visualized by STM are likely MABr or Br^- vacancies, and that the electronic states associated with them are highly localized around the defect sites.[195] However, defect dynamics in OHPs has yet to be explored with STM. Experimental support for ion migration has been shown at the device level, but atomic scale verification of this phenomenon and confirmation of the mechanism at the origin of it is lacking. In this chapter, the nature and dynamics of surface defects in the perovskite crystal lattice, as well as their impact on local electronic properties, are explored via STM experiments and DFT calculations. Several defect species at the atomic scale are observed, and the first atomic scale observation of ionic motion in OHPs is presented.

3.2 Methods

Both single crystal and thin-film perovskite samples were used for this study, and similar results were obtained for both sample types. As described in detail in Section 2.2, the single crystals samples were grown by the solvent-exchange method and cleaved *in situ* whereas thin film samples were prepared by precursor co-deposition onto an Au(111) single crystal. $MAPbBr_3$ thin films were obtained by co-evaporation of MABr and $PbBr_2$ species at evaporation temperatures of 361 K and 498 K, respectively, for 10 min. The STM measurements were performed at a range of temperatures (4.6 − 180 K), which were achieved by cooling with either liquid nitrogen or liquid helium followed by counter heating of the STM sample stage controlled by a Lakeshore 335 Temperature Controller. Cut Pt/Ir tips were used to acquire the STM images. The bias voltage was applied to the sample. It has been reported that high-energy electrons from the tip can induce surface degradation under UHV conditions in single crystal $MAPbBr_3$ during

conductive atomic force microscopy imaging.[196] In order to confirm STM imaging did not induce generation and diffusion of atomic defects and surface degradation during the imaging process, we scanned the same area consecutively for 117 times, and no surface degradation or defect generation was observed. Additionally, the effect of the tip on diffusion events has been previously shown to be negligible when using the "movie" technique of taking consecutive images of the same area.[197]

DFT calculations were performed using the Vienna ab initio simulation package code.[198, 199] The projector augmented wave pseudopotential[200, 201] was used to describe the core electrons, and a plane wave basis set with a kinetic energy cutoff of 400 eV was used to expand the wave functions. Electronic exchange and correlation was described within the framework of generalized gradient approximation of Perdew, Burke, and Ernzernhof functionals.[202] The $MAPbBr_3$ (010) surface was represented using a periodic slab based on the space group Pnma containing four atomic layers and a vacuum thickness of 14 Å. Specifically, two supercells were used; one is a 2 × 2 supercell used for the vacancy calculations, while the other is a 3 × 1 supercell for the Br^- pair orientation shift calculations. Respectively, Brillouin zone sampling was done using 3 × 1 × 3 and 6 × 1 × 2 Monkhorst−Pack[203] grids. The bottom layer of atoms was kept fixed, while the other atoms were allowed to relax. All structures were fully relaxed until the force on each atom was <0.01 eV/Å. Transition states for MABr migration along the surface were located by climbing image nudged elastic band method[204] using three images with a convergence of 0.05 eV/Å for the force components both along and perpendicular to the tangent of the reaction path.

3.3 Defects at the $MAPbBr_3$ surface

The work by Ohmann et al. first showed the surface reconstruction of $MAPbBr_3$ originating from the relative position and orientations of the dipole of neighboring MA cations.[150] Here, similar STM images of the pristine surface (Fig. 3.1a) are obtained on MAPbBr3 samples prepared by both the single crystal cleavage method and the co-evaporation method. Reiterating from Section 2.5, Br^- ions are seen as bright protrusions in STM images, and the electrostatic interaction of the partially positive nitrogen atoms (blue atoms, Fig. 3.1a) with two neighboring Br anions causes "pairing" of the Br^-. The Br^- pairs have two possible orientations at the (010) surface, which are orthogonal to each other.

Defects can occur on the paired reconstruction surface, and our STM investigation revealed multiple types of intrinsic defects at the atomic scale. The first defect type is an unpaired Br anion (gray dot in Fig. 3.1b), which occurs when there is a pair orientation mismatch in the same row (blue and green rectangles in Fig. 3.1b). The orientation mismatch results in a single Br- that has bromide neighbors in each adjacent lattice position, but is paired with none of them. In most cases, the unpaired Br^- defects are isolated from one another. However, it was also observed that two adjacent unpaired Br^- defects can occur when there is a vacancy nearby (Fig. 3.1c). These vacancies constitute the second type of defect observed, and they appear as a dark depression in STM images (Fig. 3.1d). Here, multiple types of vacancies, including single, double, and triple defects (Fig. 3.1d-f, respectively) were observed. A recent DFT study provided theoretical evidence showing that these depressions in STM images are likely either a charged Br^- vacancy or a neutral MABr vacancy.[195]

Adapted and reproduced with permission from Ref. 170. Copyright 2019, American Chemical Society. DFT calculations performed by collaborators in Prof. Guofeng Wang's group at The University of Pittsburgh.

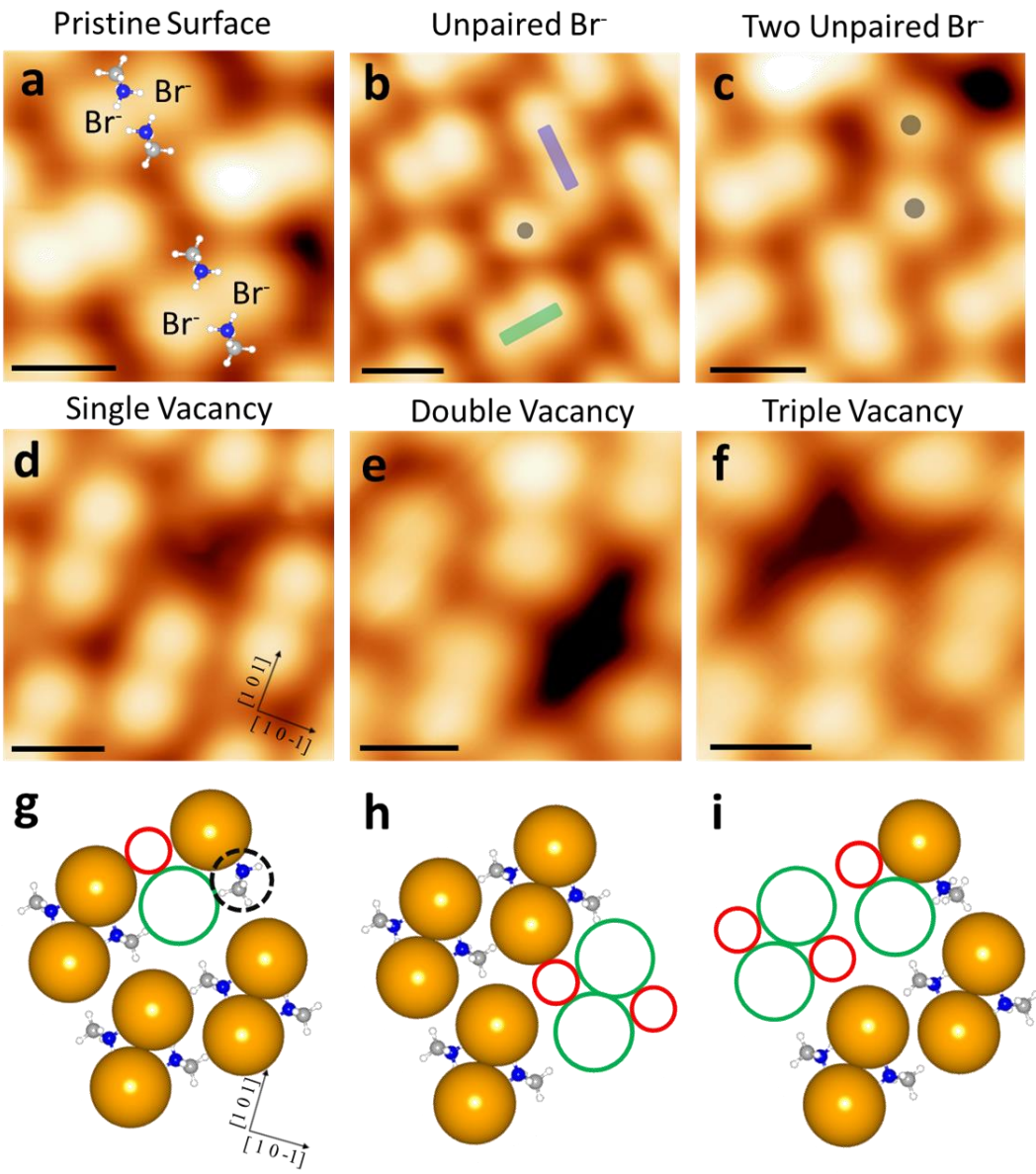

Figure 3.1 Intrinsic defects on the surface of $MAPbBr_3$. STM images of (a) the pristine $MAPbBr_3$ surface, (b) an unpaired Br^- (gray dot) at the point where two Br pair orientations (green and blue rectangles) meet, (c) two adjacent unpaired Br^- (two gray dots), located near a vacancy. d-f) STM images of single, double and triple vacancy defects, respectively. g-i) Top view of the model slab used for DFT defect formation energy calculations for the single, double, and triple vacancy defect cases, respectively. Solid green and red circles denote Br^- and MA^+ vacancies, respectively. Dashed black circle in (g) highlights a rotated MA^+ molecule. Image sizes: a) 1.6×1.6 nm^2 b) 2.0×2.0 nm^2 c) 1.8×1.8 nm^2 d) 1.8×1.8 nm^2 e)1.7×1.7 nm^2 f)1.6×1.6 nm^2. Imaging parameters: sample bias a-c,e,f) V = -9.0 V d) V = -3.0V ; tunneling current a-c,e,f) I = 20 pA d) I = 100pA. Sample Type: a-c,e,f) single crystal d) thin film. Color code: N (blue), C (gray), H (white), Br (brown). All scale bars are 5.0Å.

Adapted and reproduced with permission from Ref. 170. Copyright 2019, American Chemical Society. DFT calculations performed by collaborators in Prof. Guofeng Wang's group at The University of Pittsburgh.

To further characterize the above observed defects, energies of formation were calculated by DFT calculations. The formation energies for MABr and Br^- vacancies are, respectively, calculated by

$$E_{form}(V_{MABr}) = E_{MABr} + E_{V_{MABr}} - E_{MAPbBr_3}$$

and

$$E_{form}(V_{Br}) = E_{Br} + E_{V_{Br}} - E_{MAPbBr_3}$$

where E_{form} is the formation energy, E_{MABr} and E_{Br} are the electronic energies of MABr and Br^- species, respectively, $E_{V_{MABr}}$ and $E_{V_{Br}}$ are the electronic energies of the defective MAPbBr3 surface with MABr and Br^- vacancies, respectively, and E_{MAPbBr_3} is the electronic energy of the pristine $MAPbBr_3$ surface. A formation energy of 1.94 eV was obtained for a single MABr vacancy, compared to 2.48 eV for a Br^- vacancy, suggesting a preference for the formation of MABr vacancies. This trend is consistent with previous calculations in the literature.[195] Comparison calculations were performed with and without van der Waals forces taken into account, and the same trend was obtained. Thus, subsequent calculations were performed without van der Waals corrections to conserve computational resources. Additionally, hereafter vacancies are treated as MABr vacancies since those had a lower energy of formation (1.94eV). We do not, however, use this as a basis to rule out the possibility of charged vacancies in perovskite films. Rather, we focus on the neutral defect due to computational concerns related to the influence of image charge in the case of a charged vacancy. For a single MABr vacancy, calculations show that there is a 90º rotation of the MA cation adjacent to the defect (Fig. 1g, dotted black circle), with the positive nitrogen end of the dipole near the unpaired Br^-. The formation energies for double and triple MABr vacancies were also calculated and found to be 3.49 eV and 5.26 eV, respectively.

As mentioned earlier, the MA cation is typically not resolved in STM images, making an experimental distinction between MABr and Br^- vacancies challenging. However, with fortuitous tip conditions, it is possible to resolve the MA cation on rare occasion, as previously reported.[150] During this study, there was one instance of such favorable tip conditions. Figure 3.2a shows a larger area image in which MA cations can be seen as smaller protrusions that occur just above and just below the middle of a Br^- pair (red dots, Fig 3.2a), which agrees well with reported simulated STM images (Fig 3.2b).[150] As a guide for the eye, one repeating motif has an overlay where the Br^- and MA^+ protrusions are marked with black and green circles, respectively. A zoom-

Adapted and reproduced with permission from Ref. 170. Copyright 2019, American Chemical Society. DFT calculations performed by collaborators in Prof. Guofeng Wang's group at The University of Pittsburgh.

in on a vacancy defect is shown in Figure 3.2c. This vacancy defect differs from the circular depressions seen in other STM images. Here the vacancy seems to be a large and small depression conjoined, taking a "light bulb" shape. The circles on Figure 3.2c highlight that the repeated motif near the vacancy is missing one of its smaller MA^+ protrusions. This "light-bulb" shaped depression matches well with previously reported simulated STM images for an MABr vacancy (Fig. 3.2d).[195] While this image does not allow for a definitive assignment of the vacancy identity, it does provide some measure of experimental support for the DFT-based assignment of an MABr vacancy.

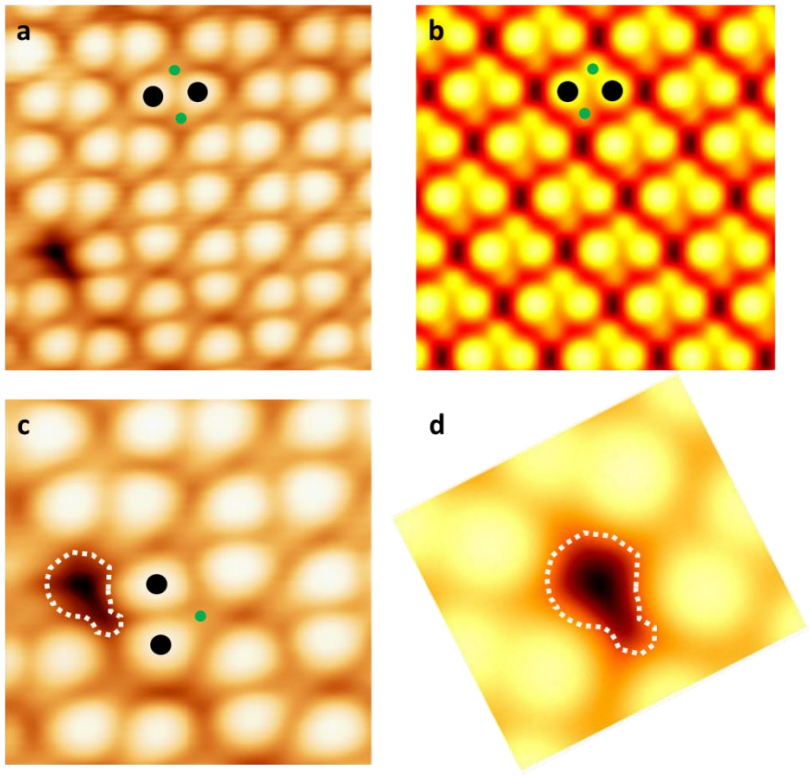

Figure 3.2 MA-resolved STM images. STM image (a) and DFT simulated STM image (b) of $MAPbBr_3$ surface with MA^+ resolved. Fig. b adapted with permission from Ref. 2 under the *ACS AuthorChoice* Usage Agreement. Copyright 2015, American Chemical Society. Zoomed-in STM image (c) and DFT simulated STM image (d) of an MABr vacancy. Fig. d adapted with permission from Ref. 193. Copyright 2017, American Chemical Society. Br^- and MA^+ labeled with black and green circles, respectively. White dashed lines denote shape of MABr vacancy depression. Imaging parameters: (a,c) V=8.3 V; I=600 pA. Image size: (a) 3.8×3.8 nm^2; (c) 2.5×2.5 nm^2.

Adapted and reproduced with permission from Ref. 170. Copyright 2019, American Chemical Society. DFT calculations performed by collaborators in Prof. Guofeng Wang's group at The University of Pittsburgh.

3.4 Reorientation of Br^- pairs

Having characterized the surface defects observed on the $MAPbBr_3$ surface in the previous section, the next two sections will focus on dynamic events involving surface defects. The first manifestation of dynamics at the perovskite surface consists of Br^- pair re-orientation, which was observed in consecutive STM images of the same area. In the (010) surface reconstruction, Br^- pairs are oriented along either the [101] or [10-1] axes, which are orthogonal to each other (green and blue rectangles in Figs. 3.3a and b). Strikingly, Br^- pairs could dissociate and re-associate with neighboring Br^- ions, thus forming pairs rotated 90° (blue rectangles in Fig. 3.3b) compared to their original orientation (green rectangles in Fig. 3.3b). In the case shown in Fig. 3.3, the re-orientation occurs within a single "orientation domain" (i.e., all rows start with the same orientation). Br^- pair reorientation can also occur at the edge of two orientation domains.

A DFT simulation of the Br^- pair reorientation process shows that a rotation of the MA molecules is accompanied by a separation of Br- pairs (Fig. 3.3d). Further rotation in the same direction then results in those separated Br^- creating a pair with their other neighbor. The initial and final states were found to have the same energy, indicating that there is no preferred orientation for the Br^- pairs at the perovskite surface. This result is consistent with our experimental observation where the same row may re-orient but then later return to its original orientation. In addition to a rotation within an orientation domain as shown in Fig. 3.3, re-orientation events were observed occurring along an orientation domain boundary (i.e., one of the rows adjacent to the re-orienting row is of the opposite orientation). DFT simulations found Br^- pair re-orientation has a lower transition state energy barrier of 0.13 eV when it occurs at an orientation domain boundary, compared to 0.31 eV when it occurs within a single orientation domain. The lower energy barrier means that re-orientation is more likely to occur at the boundary of two orientation domains.

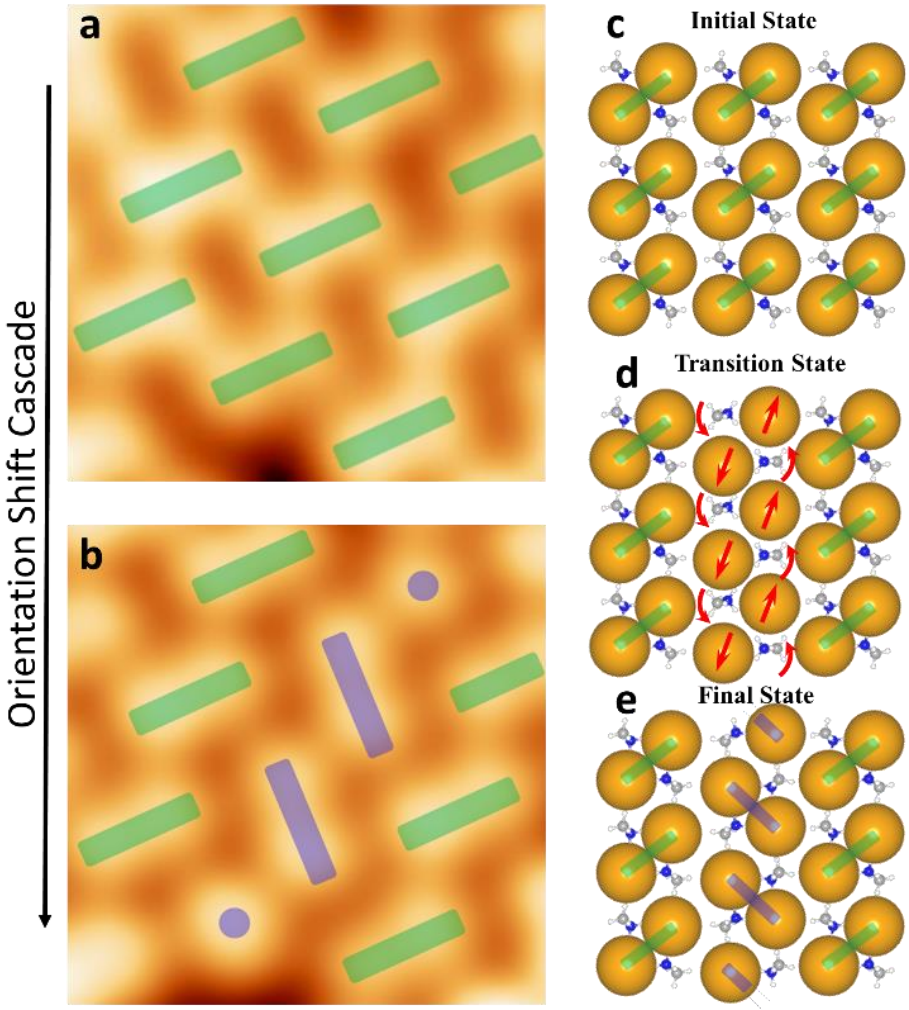

Figure 3.3 Br^- pair orientation shift. a,b) Consecutive STM images of single crystal $MAPbBr_3$ showing a Br^- pair orientation shift. The three rows start in the same orientation (a, green rectangles), but the middle row undergoes an orientation shift to form pairs rotated 90° (b, blue rectangles) from the original orientation. Image size: a-b) 2.3 × 2.3 nm^2. Imaging parameters: a-b) sample bias voltage = –9.0 V; tunneling current = 20 pA. c-e) DFT simulations of Br dimer re-orientation showing the initial (c), transition (d) and final states (e). The transition state energy is 0.31eV higher than the initial and final states, which were found to have the same energy. Color code: N (blue), C (gray), H (white), Br (brown).

Additionally, from experimental observation, re-orientation cascades tend to start and terminate more often near defects. DFT calculations compared the energy of separation of a Br^- pair on a pristine surface versus a surface with a vacancy defect. A lower energy of separation was found when the Br^- pair is near an MABr vacancy, suggesting that the proximity of a vacancy facilitates the Br^- pair separation (Fig. 3.4).

Adapted and reproduced with permission from Ref. 170. Copyright 2019, American Chemical Society. DFT calculations performed by collaborators in Prof. Guofeng Wang's group at The University of Pittsburgh.

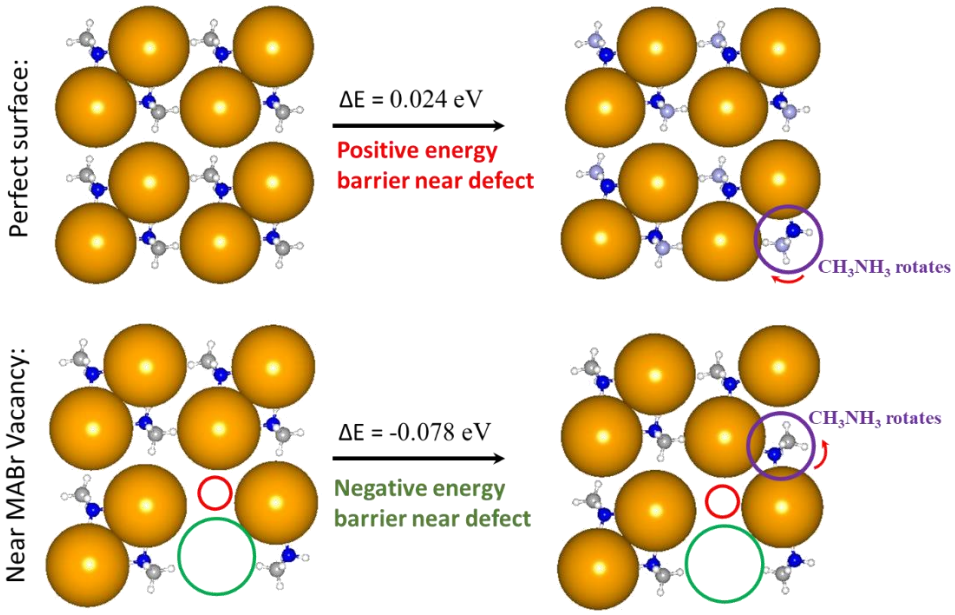

Figure 3.4 Vacancies promote Br^- pair separation. Initial and final states for separation of Br^- pairs in pristine $MAPbBr_3$ surface (top) and when the Br^- pair is near an MABr vacancy (bottom). The presence of a vacancy lowers the energy of separation by approximately 0.1 eV.

This calculation result can explain the two adjacent unpaired Br^- ions close to an MABr vacancy in Fig. 3.1c. The calculation shows that the separation of the Br^- ions is also accompanied by a rotation of the MA cation on the defective surface. The MA rotation and Br pair separation are also necessary for allowing the Br^- pair re-orientation event. This suggests that a re-orientation event is more energetically favorable when occurring near a vacancy defect. It is worth noting that these re-orientations were observed occurring in cascades covering distances on the order of tens of nanometers (Fig. 3.5). Thus, it could be possible that defect movement in one area of the perovskite surface could cause an orientation shift that then affects a remote area of the film.

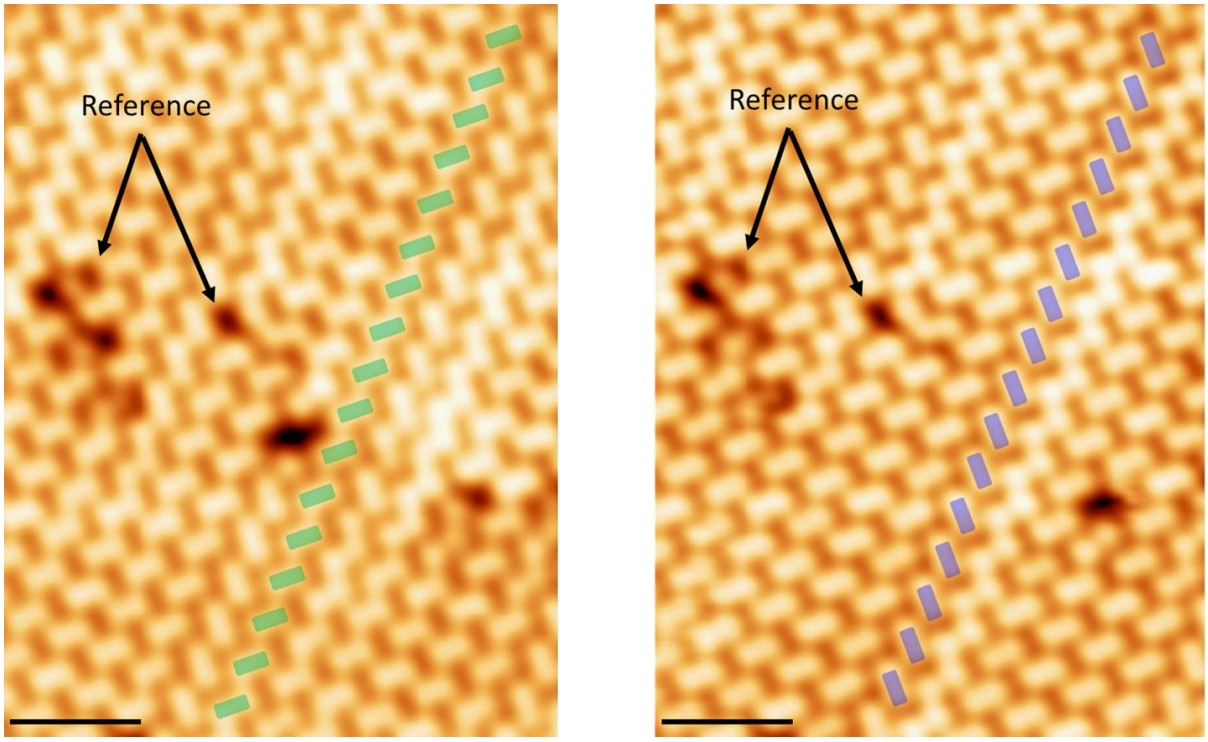

Figure 3.5 Long-range reorientation cascade of Br^- pairs. Consecutive STM images taken at 30K showing a reorientation cascade spanning over 10 nm. Imaging parameters: sample bias voltage = -9.0 V, tunneling current = 20 pA. Scale bars are 2.0 nm.

3.5 Vacancy-assisted ion transport

In addition to Br^- pair re-orientation, MABr vacancy-assisted ion transport along the surface was also imaged. Consecutive STM images (Figs. 3.6a and b) show mobility of the vacancies along the perovskite surface. Multiple ion transport paths were identified and DFT simulations were performed. Importantly, a substantial difference in energy barrier was found depending on the mechanism. To simulate the ion transport process, a sequential mechanism in which Br^- moves first, followed later by MA^+, was envisaged by DFT. In the first step, when Br^- moves alone, there is a higher transition energy of 0.91eV and an increase in system energy of 0.14 eV (Fig. 3.6c-f). This energy increase is likely due to an increase in electrostatic potential energy from the creation of isolated charges. In contrast, when a simultaneous transport mechanism is considered, where MA^+ and Br^- migrate together, the transition energy barrier is lowered to 0.46 eV and there is no increase in the system energy (Fig. 3.6g-j). This finding is significant as it suggests that once an MABr vacancy exists at the surface, the MA^+ and Br^- tend to diffuse together when moving along the (010) surface layer. This result unambiguously shows

Adapted and reproduced with permission from Ref. 170. Copyright 2019, American Chemical Society. DFT calculations performed by collaborators in Prof. Guofeng Wang's group at The University of Pittsburgh.

that defects migrate not just at the grain boundaries, but also along the perovskite interface with other layers in a device. This implies that there is temporal change of local interfaces properties.

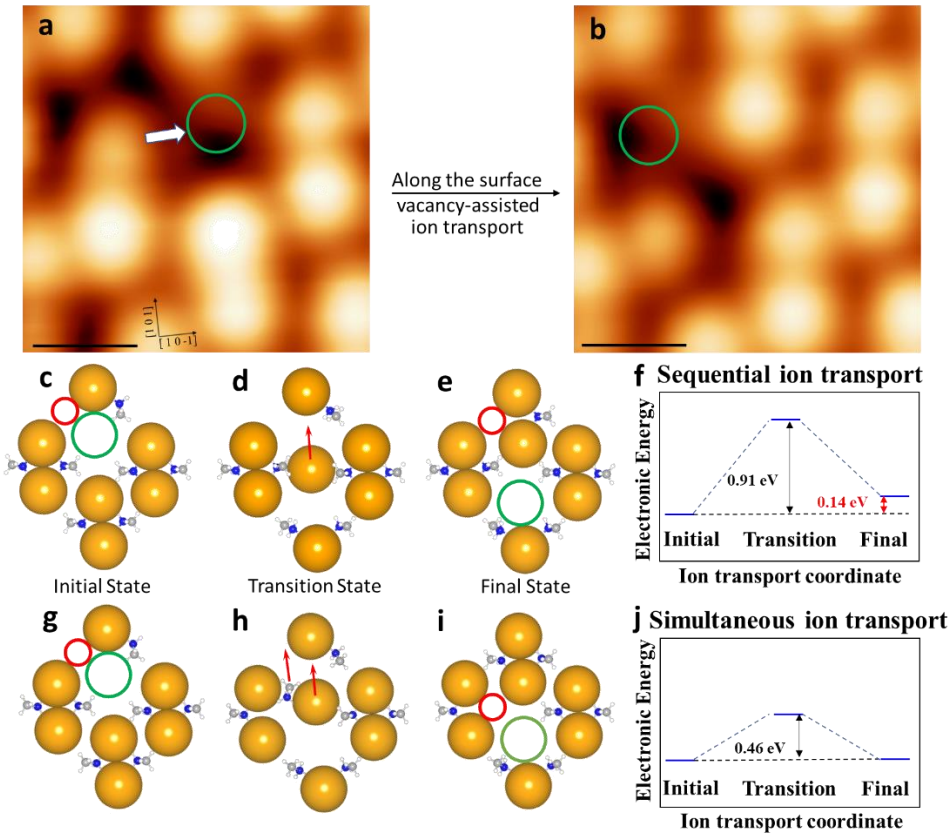

Figure 3.6 MABr vacancy-assisted ion transport along the surface of $MAPbBr_3$. (a,b) Consecutive STM images showing vacancy defect movement along the surface of an ultrathin film of MAPbBr3 at 180 K. Models and energy diagrams calculated via DFT of a sequential migration (c−f) and simultaneous migration (g−j) of MABr. The sequential migration is simulated by a Br− migration as the first step. Image sizes: (a,b) 1.7 × 1.7 nm2. Imaging parameters: (a,b) sample bias voltage = 1.4 V; tunneling current = 50 pA. Color code: N (blue), C (gray), H (white), Br (brown). Scale bars in (a) and (b) are 5.0 Å.

Aside from ion transport along the perovskite surface, it was also observed that vacancies and ions can move in the z-direction, through the perovskite film. This is significant since such ion migration has been suggested as a potential cause of hysteresis and material degradation in the device,[85, 189] although the mechanism has been unclear. Here, in consecutively recorded STM images (Fig. 3.7a and b), a single vacancy defect appears at the surface (i.e., the vacancy assists ion transport from the surface to the bulk).

Adapted and reproduced with permission from Ref. 170. Copyright 2019, American Chemical Society. DFT calculations performed by collaborators in Prof. Guofeng Wang's group at The University of Pittsburgh.

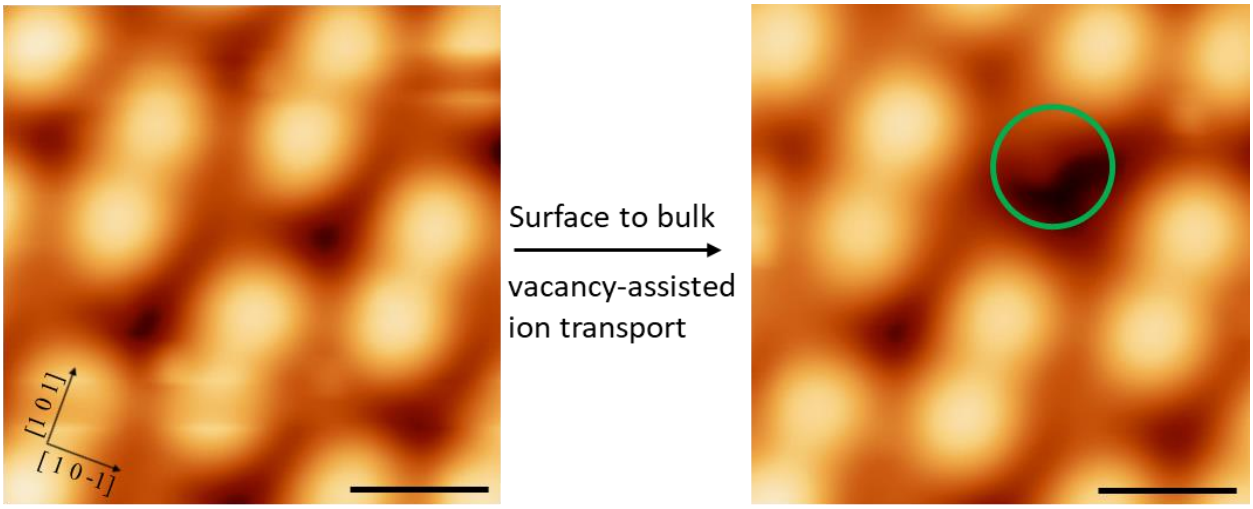

Figure 3.7 MABr vacancy-assisted ion transport in the z-direction. Consecutive STM images acquired at 77 K on thin film $MAPbBr_3$ showing an MABr vacancy-assisted ion transport from the surface layer (a) to the bulk (b). Image sizes: (a,b) 1.8 × 1.8 nm2. Imaging parameters: (a,b) sample bias voltage = −3.0 V, tunneling current = 100 pA.

This observation strongly supports the hypothesis that these vacancies provide a pathway for ion migration in perovskite materials. The opposite event was observed as well, wherein a single vacancy assists ion transport from the bulk to the surface, which is consistent with device level measurement indicating ion migration to be reversible.[190,205] Importantly, the fact that the surface layer structure changes means that the interface in a device can change as defects appear and disappear. Although it is challenging to perform a rigorous determination of ion transport event frequency via STM, a rough range of one event per 10^1-10^3 seconds can be estimated based on the STM image acquisition time and line scan speed. More importantly, these events can occur at a much higher frequency at the fabrication and operation temperatures of a device, which are significantly higher than the STM imaging temperatures in this work. It should be noted that attempts were made to gauge the effect of temperature on these dynamic events. However, imaging conditions became progressively more unstable at higher and higher temperatures, and obtaining enough images to make a comment on temperature dependence was not feasible. It is worth pointing out that the paired reconstruction was seen at temperatures up to 290K (Fig. 3.8), which suggests that the perovskite's surface reconstruction is qualitatively similar in the cubic phase as in the low-temperature orthorhombic phase. This is important because $MAPbBr_3$ exists in the cubic phase during operation of a solar cell. The similar nature of the surface reconstruction in both

orthorhombic and cubic phases means that the phenomena seen in the low temperature orthorhombic phase likely also occur in the device relevant cubic phase.

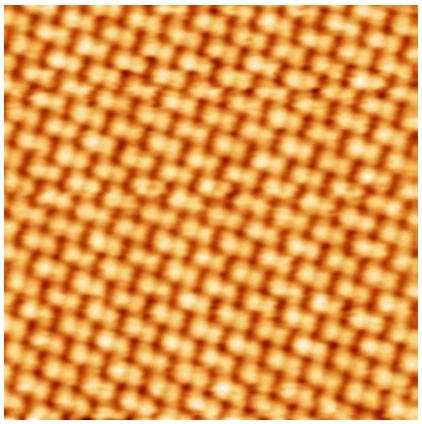

Figure 3.8 $MAPbBr_3$ surface in the cubic phase temperature range. STM image of the surface of an $MAPbBr_3$ ultrathin film taken at 290K. The surface exhibits a surface reconstruction qualitatively similar to that seen in the low-temperature orthorhombic phase. Imaging parameters: V = 0.69V; I = 700pA.

Of the dynamic events observed, the surface to bulk movement is of special interest because it more closely corresponds to the widely studied but not well understood phenomenon of ion migration in perovskite solar cells. One question that remains is the mechanism by which ion migration occurs. DFT calculations were performed to identify the possible mechanism of the ion transport observed via STM. The calculation considers a cell in which a single MABr vacancy defect exists in the bulk layer. Thereafter, a simulation of the transport of the MABr vacancy was performed. It was found that it is energetically more favorable by 0.75 eV for the MABr vacancy to be in the surface layer than in a bulk layer. Simulations of multiple migration mechanisms were tested, and it was found that a sequential mechanism is energetically favored (Figure 3.9a and b). In this sequential process, a Br^- ion moves from the subsurface layer to the bulk layer. This is followed by an MA molecule crossing from the surface layer to the bulk layer via the Br^- vacancy left in the subsurface layer. Finally, in the last step of the process, a Br^- ion travels from the surface layer to the subsurface layer. The energy barrier for a multistep process is determined by the highest barrier for an individual step. An energy diagram showing the barrier for each step (Fig. 3.9c) reveals that the highest barrier is 0.55 eV and occurs during the second step, as the MA^+ crosses through the subsurface layer. For the reversed sequential mechanism that describes the MABr vacancy migrating from surface to bulk, 1.09 eV is the overall energy barrier. Simulation

Adapted and reproduced with permission from Ref. 170. Copyright 2019, American Chemical Society. DFT calculations performed by collaborators in Prof. Guofeng Wang's group at The University of Pittsburgh.

of a simultaneous transport mechanism in which MA^+ and Br^- migrate together resulted in an energy barrier above 2.3 eV, over quadruple that of the sequential mechanism. The preference for the sequential mechanism can be explained by a decrease in steric hindrance. During the first step of the sequential mechanism, the Br^- vacancy formed in the subsurface layer provides a larger gap

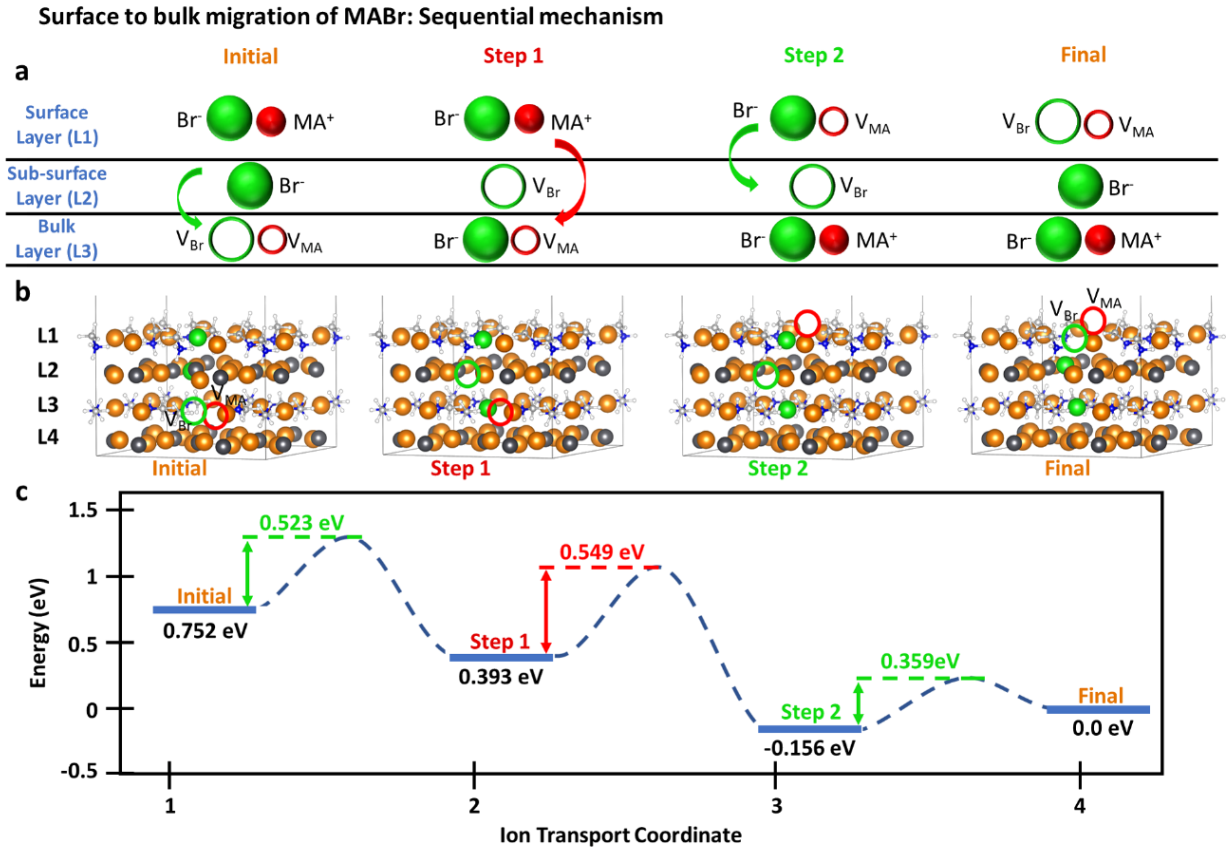

Figure 3.9 Sequential migration mechanism. (a) Schematic drawing showing MA+ and Br− movement for each step of the mechanism. Empty circles represent vacancies. (b) Crystal structures from DFT simulation of the sequential mechanism. Empty circles represent vacancies. (c) Illustration of the energy profile for the sequential mechanism showing the energy barrier for each step. The highest energy barrier, and thus the barrier for the entire mechanism, is highlighted in red.

through which the MA^+ can cross the atomic layer. Additionally, this mechanism is sterically favorable because only the MA^+ is crossing the subsurface layer, rather than the larger MABr passing through the layer as one unit.

It bears mentioning that there was no external stimulus (e.g., external bias, light, temperature, or chemical gradient) considered in our calculations. Many factors are at play

Adapted and reproduced with permission from Ref. 170. Copyright 2019, American Chemical Society. DFT calculations performed by collaborators in Prof. Guofeng Wang's group at The University of Pittsburgh.

contributing to ion transport in an operating device, and multiple pathways for transport have been suggested.[206] The sequential mechanism examined here provides one answer to the question of how ion transport occurs in perovskite films. Ion migration induced by the built-in electric field of devices has been shown to be reversible, and the transport seen here can provide clues about how the ions re-establish their original equilibrium distribution after a device is turned off.[98, 207] Specifically, we contrast the z-direction ion transport case, where MA^+ and Br^- move sequentially, with the case of along the surface transport, where the MA^+ and Br^- ions were found to move simultaneously. Transport along the surface does not require the MA^+ ion to pass through the sterically constrained $PbBr_2$ subsurface layer, which allows simultaneous movement of MA^+ and Br^- to be energetically favorable (Figs. 3.6c–j). Although our calculation describes cases of ion transport that involve surface layers, some information regarding transport in the bulk can be extracted. The energy profile in Figure 3.9c shows that the highest energy transition state occurs when the MA^+ crosses through the defective $PbBr_2$ subsurface layer. If we consider a similar model but in the bulk of the material, we can also expect a high transition state barrier for ion migration along the z-direction, that is, the [010] direction. Although the magnitude of the difference in energy barriers between ion migration along the [10 ± 1] and [010] directions may be different for the bulk case, it is reasonable to expect migration along the [010] direction will have a higher energy barrier, as the hurdle of crossing the $PbBr_2$ layer still exists when we consider the bulk scenario. That energy barrier is expected to increase in the case where an MA^+ alone is migrating and there is no Br vacancy nearby to facilitate the crossing of the $PbBr_2$ layer, making ion migration along the [010] direction even less favorable.

It should be noted that both the thin film and single crystal samples are terminated with the (010) plane at the surface.[150, 167] In contrast, polycrystalline films used in devices may have crystalline grains with orientations that vary from grain to grain,[208, 209] which could result in different migration energies. The dependence of the migration energy on the direction of migration has important consequences for perovskite devices, which are made from polycrystalline films with grains of varying orientation.

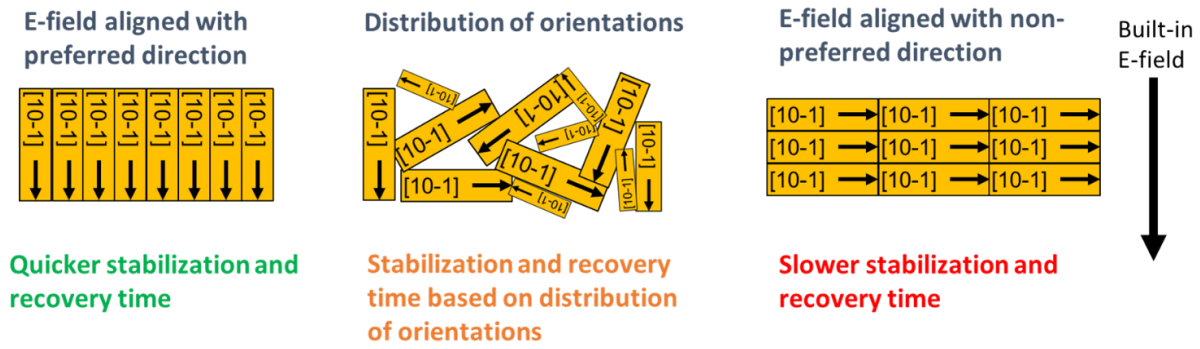

Figure 3.10 Effect of crystal orientation on ion migration. Schematic drawing showing the impact of crystal orientation alignment with the built-in electric field in devices. The change in ion migration energy barrier could lead to variation in the time needed to achieve steady-state operation and to re-establish dark condition equilibrium.

Specifically, the orientation of the individual grains with respect to the vertical axis of the device, along which the photo-induced built-in electric field occurs, will affect paths along which ions migrate under illumination and subsequently diffuse back to equilibrium during dark conditions (i.e., at night). The paths along different crystal directions will have different migration energies, and thus different time constants for achieving steady-state operation and for returning back to dark condition equilibrium (Figure 3.10). It has been reported that perovskite solar cells have reversible losses under illumination due to cation migration and that a certain recovery time in the dark is needed to return to original efficiency.[98] This recovery time depends on the energy barrier for ions to diffuse back to equilibrium, which would be affected by the distribution of grain orientations. Identifying a specific orientation that enables quick device recovery could provide a valuable research avenue for creating perovskite solar cells that have an overall higher performance and better stability and are well suited to locations with rapidly changing sun irradiance.

3.6 Effect of vacancy defects on interfacial properties

In addition to the dynamics of intrinsic defect species and the mechanisms of defect-assisted ion migration, it is also of interest to understand how the surface defects observed in STM affect the surface properties of the perovskite, which would in turn affect the interface of the perovskite with an adjacent layer in a device. Such interfaces are seen as a key to optimizing device performance, as they play an important role in charge transport and recombination. To better

Adapted and reproduced with permission from Ref. 170. Copyright 2019, American Chemical Society. DFT calculations performed by collaborators in Prof. Guofeng Wang's group at The University of Pittsburgh.

understand the effect of these vacancies on the interface, the electronic potential was calculated as a function of position along the [010] direction (Fig. 3.11). Significant separation of the potential curves occurs around 0 Å, which corresponds to the perovskite surface. This may be due to defect energy levels introduced by dangling bonds. The inset of Figure 3.11 shows in detail the area used for identifying the vacuum level. A linear fit was used, and the value of this fit at 7.5 Å (middle of the vacuum slab) was taken to be the vacuum level. This also determines the work function, which is the difference in energy between the Fermi level and the vacuum level. Importantly, a trend was identified in which an increasing number of vacancies raised the work function from 5.29 eV (the pristine surface case) to 5.45 eV (the triple MABr vacancy case).

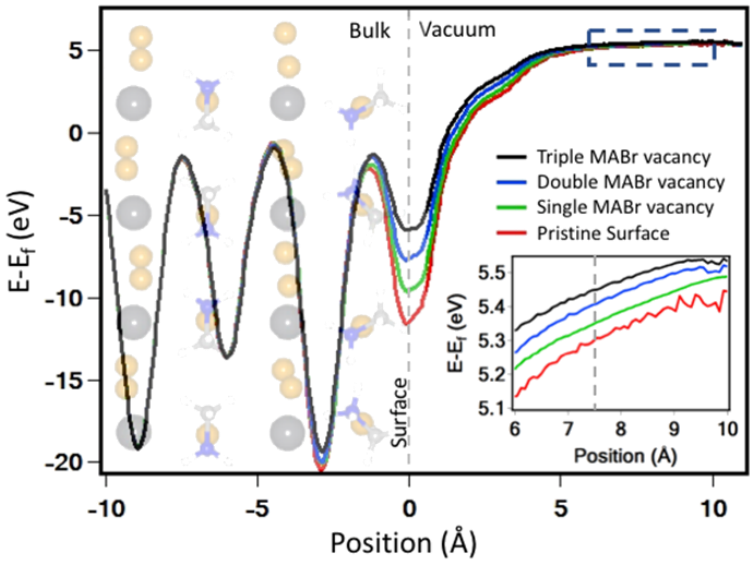

Figure 3.11 Surface defect-induced work function modification. Electric potential plotted as a function of position relative to the surface. Position of −10 Å corresponds to the bottom of the slab. (Inset) Zoom in on the vacuum region to highlight differences in the work function. After linear fitting, the work function was taken to be the potential value (relative to the Fermi energy) at a distance of 7.5 Å (gray dashed line).

It is important to note that the size of the super cell used for the calculation is limited. For the pristine surface there are 8 Br^- ions and 8 MA^+ cations in the surface layer of the supercell used for DFT. Thus, the single, double, and triple MABr vacancy defect surfaces have 1/8, 2/8, and 3/8 of the atoms missing and correspond to an overall MABr surface vacancy defect concentration of 12.5%, 25%, and 37.5%, respectively. It has been suggested that ion migration leaves one end of the perovskite film deficient in the migrating halide species (i.e., rich in halide vacancies).[101] Thus, such high defect concentrations may occur at the interface during device

Adapted and reproduced with permission from Ref. 170. Copyright 2019, American Chemical Society. DFT calculations performed by collaborators in Prof. Guofeng Wang's group at The University of Pittsburgh.

operation. Additionally, the variation of the local work function could potentially alter charge transfer to adjacent layers (i.e., electron or hole transport layers, top electrode) in a solar cell or light emitting device. It is important to take this effect into account when evaluating efficiency loss mechanisms. Understanding interfaces in perovskite devices and engineering energy level alignment between layers have been identified as one of the keys to unlocking higher efficiencies and better stability.[210] As further work on energy level alignment between layers is conducted, it should be kept in mind that this work function variation at the interface exists due to surface defects. This variation may limit the accuracy of energy level alignment attainable if the issue of reducing or controlling the number of defects in the perovskite film is not addressed. As seen in the migration mechanisms investigated, there could be spatial variation in work function not only due to the presence of defects but also spatial and temporal variation as vacancies migrate to and from the surface as well as along the surface. Such variation of the electronic properties of perovskite in space and in time could in turn affect the charge transfer at the interface.

The increase of the work function as the surface contains more defects can be attributed to one or a combination of the following three fundamental mechanisms: 1) The surface dipole that occurs with vacancy defect presence. A recent theoretical study by Jacobs et al. examining 20 different perovskite oxides found that the BO_2 surface terminations had higher work functions than the AO surface terminations.[211] This was attributed to a work function lowering surface dipole caused by the AO layer. Albeit a different material system, it is reasonable to consider that a similar trend may exist in halide perovskites, where termination at a BX_2 layer would have a higher work function than an AX termination. This type of trend is consistent with the result found in this work, that an increasing number of surface vacancy defects (i.e. an increasing exposure of the BX_2 layer) leads to an increase in work function. A systematic theoretical study on OHP work function trends, similar to the one Jacobs et al. reported for perovskite oxides, is needed for further clarification of the fundamental principle behind the trend seen here; 2) This local fluctuation in charge can also be considered to effect the work function via a change in the screening effect due to the introduction of the vacancy defect. A theoretical study shows that MA cations can reorient themselves to screen vacancy defects, and that this rearrangement results in non-zero polarization values at the surface. This uncompensated dipole near the vacancy defect could also be contributing to the work function change reported in this thesis;[212] 3) Vacancy defects may also result in a change in the polaron binding energy due to local lattice distortions. According to

Coropceanu et al.,[213] lattice distortions can lead to an increased polaron binding energy for a charge carrier over a given lattice site. Vacancy defects could cause lattice distortions that increase the polaron binding energy at nearby lattice sites. Thus, the energy required for an electron localized over the vacancy defect site to escape to the vacuum level would increase, resulting in an increased work function.

3.7 Summary

In this chapter, an atomic-scale investigation of surface defect dynamics in organic−inorganic hybrid perovskite was carried out by combining experimental techniques (STM) with theoretical calculations (DFT) performed by collaborators. Numerous defect types were observed by STM at the surface of $MAPbBr_3$ perovskite, including vacancy clusters, as well as unpaired Br^- defects caused by the orientation mismatch of Br^- pairs in a single row. Vacancy defects were shown to enable Br^- pair separation, thus potentially facilitating Br^- pair reorientation events and long-range surface dynamics. From energy of formation calculations and experimental images, vacancy defects were identified as MABr vacancies. STM measurements visualized the vacancy-assisted motion of single ions in real space, both in the z-direction as well as along the perovskite surface, strongly supporting the hypothesis of a vacancy-assisted ion migration pathway in perovskite materials. Based on these STM observations, DFT calculations were performed to identify favorable ions migration mechanisms. It was demonstrated that in the z-direction it is energetically favorable for MABr migration to occur via a sequential mechanism. The transition energy barrier found is small enough for ion migration to occur via this mechanism in an operating perovskite solar cell. Furthermore, the impact of vacancy defects on the local work function at the surface of the perovskite was revealed. The modification of local work function induced by clusters of vacancies observed here is expected to strongly affect charge transport and recombination at the interface of a device. The results in this chapter provide a fundamental understanding of the interfacial effects of surface vacancy defects, and also atomic scale insight into the ion migration mechanism. Equally important, this work reveals useful information for device improvement from the perspective of defects and interface engineering.

However, defects are only part of the picture. As discussed in Section 2.3, passivation of surfaces is also a topic of importance for optimizing devices. One such strategy is to add chlorine to the perovskite material, but exact function of chlorine, and in what fashion and to what extent

it is incorporated into the perovskite lattice, is unclear. In this context, the effects of modifying the perovskite surface with chlorine and iodine will be discussed in the next chapter.

Adapted and reproduced with permission from Ref. 170. Copyright 2019, American Chemical Society. DFT calculations performed by collaborators in Prof. Guofeng Wang's group at The University of Pittsburgh.

Chapter 4: The Surface of Mixed halide Methylammonium Lead Perovskites[167]

4.1 Introduction

In the previous chapter, modifications to the $MAPbBr_3$ surface caused by defects were explored. However, perovskite films used in devices often employ more complex formulations involving a mixture of halides in the X site of the perovskite structure, therefore understanding the surface of these systems is also of prime importance. Having a mixture of halide species in the perovskite material can provide multiple benefits, including band gap tuning, improved stability, and improved film morphology. By changing the relative ratio of iodine and bromine, the band gap can be modified from 1.55 eV to 2.3 eV,[139] with this tunability being particularly useful in tandem solar cells.[28] Fine control of the bandgap is also advantageous for color tuning[214] in emissive applications such as LEDs[215] and lasers.[5] Additionally, addressing perovskite instability is a major issue, and mixing in a small percentage of bromine[1,216, 217] or chlorine[11] can improve device stability over those based on $MAPbI_3$.

Incorporation of Cl has been shown to advantageously affect the crystallization process,[164, 218] improve open-circuit voltage[219, 220] and reduce carrier recombination.[221] However, there is still an open debate regarding whether or not Cl actually incorporates into the perovskite lattice, and if yes, to what extent.[40, 222-227]

In this chapter, the effect of mixing I or Cl into an already fabricated $MAPbBr_3$ film is explored at the atomic scale, utilizing STM imaging to clarify the incorporation behavior of these two halides at the perovskite surface. DFT calculations based on the STM results demonstrate the effect of halide mixing on the surface stability of the perovskite and identify an optimal ratio of Cl incorporation that provides an increase in stability without sacrificing performance due to band-gap widening. XPS and UPS techniques are also employed to investigate the effect of halide mixing on the stability and interfacial electronic properties of the material on a larger scale.

4.2 Methods

$MAPbBr_3$ thin films were fabricated by dual-source physical vapor deposition inside a UHV chamber. $PbBr_2$ and MABr were co-evaporated at 361K and 498K, respectively, for 10min onto a cleaned and cooled Au(111) substrate (see section 2.2 for details). For $MAPbBr_{3-y}I_y$ ($MAPbBr_{3-z}Cl_z$) perovskite films, PbI_2 ($PbCl_2$) was heated via Knudsen cell to 525 K (560 K) and deposited on top of the as-prepared $MAPbBr_3$ film. For this step, the substrate was not cooled, but left at ambient temperature. For STM measurements, the sample was cooled to 5K and at cut Pt/Ir tip was used. Bias voltage was applied to the sample. The XPS and UPS instrumentation is connecting to the same UHV system as the STM, and the sample was transferred between the instruments without exposure to ambient air.

4.3 Substitution and distribution of mixed halides

$MAPbBr_3$ thin films created using the above co-deposition method were atomically flat, with a thickness of 4±1 nm. The surface exhibited a reconstruction featuring a Br^- pair pattern (Fig. 4.1a), consistent with results previously reported for cleaved single crystal $MAPbBr_3$.[150] As described in Section 2.5, the protrusions in the STM images are Br^- ions. It is important to note that for $MAPbBr_3$ all the Br anions have the same apparent height and width.

Upon subsequent sublimation of PbI_2 onto the $MAPbBr_3$ thin film, STM images showed a perovskite surface that maintained the basic pair motif, but had brighter protrusions with a larger width and an apparent height that is 40±10 pm higher than the surrounding Br^- ions (Fig. 4.1b). Conversely, after sublimation of $PbCl_2$ onto an $MAPbBr_3$ film, there are dimmer protrusions, with smaller widths and an apparent height that is 20±10 pm lower than the surrounding Br^- ions (Fig. 4.1c). These protrusions of different heights and widths could originate from a wide variety of scenarios, including adsorption or substitution of an entire lead halide molecule, or of an individual ion (Pb^{+2}, I^-, or Cl^-) after dissociation of the lead halide. DFT calculations were performed to determine which scenario is most plausible, and it was found that dissociation of the lead halide followed by halide substitution best matched experimental data. Simulated STM images of I^- and Cl^- substitution are shown in Figures 4.1e and f and agree well with the experimental STM images (Figs. 4.1b and c). A simulated STM image of the $MAPbBr_3$ surface is also shown for comparison

(Fig. 4.1d). Interestingly, the halide mixing did not result in a significant modification of unit cell dimensions. Figure 4.1g provides a schematic for the scenario of PbI_2 dissociation followed by iodide substitution. Based on these results, the brighter and darker protrusions in Figures 4.1b and c are assigned to I^- and Cl^- substitution, respectively, of Br^- at the $MAPbBr_3$ surface.

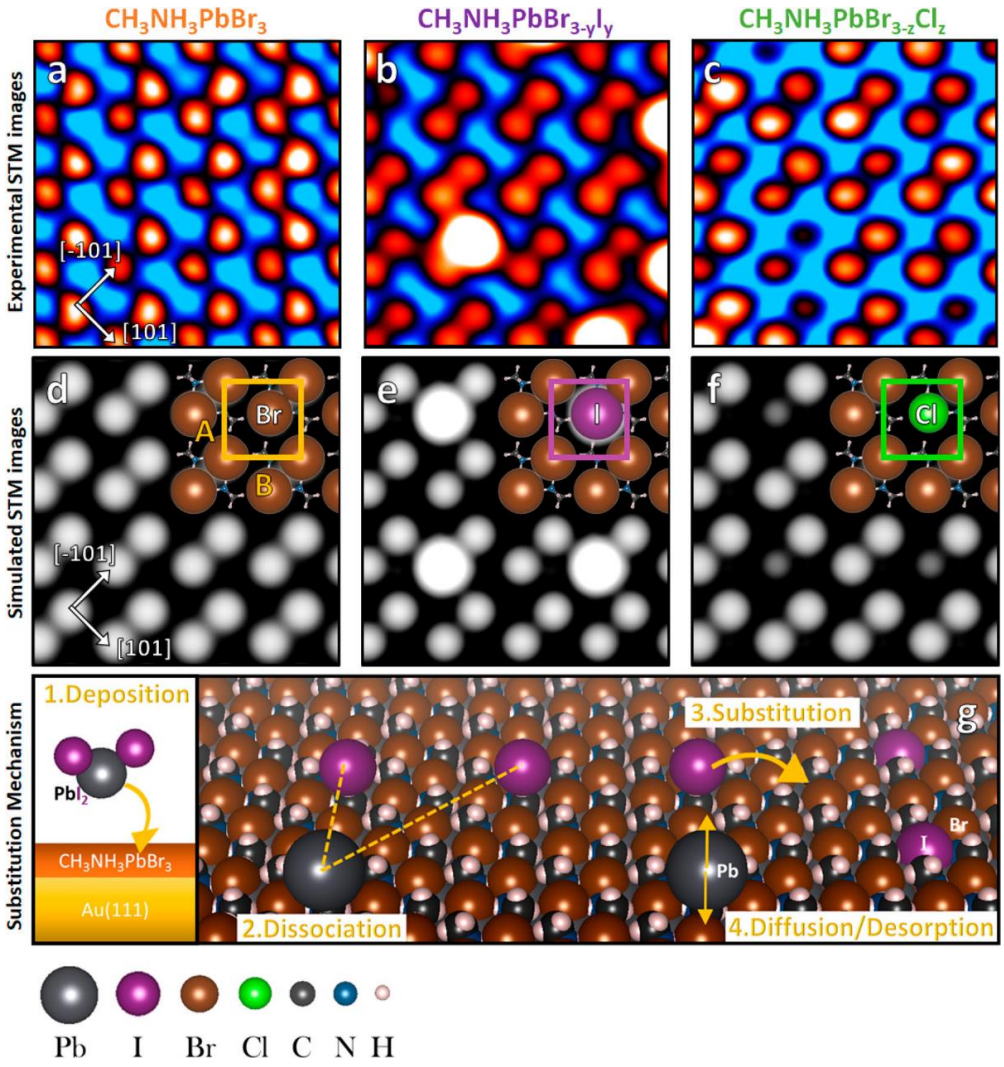

Figure 4.1 Halide substitution at the $MAPbBr_3$ surface. a) Experimental STM images (a-c) and DFT simulated STM images (d-f) of pure $MAPbBr_3$ (a, d), iodine-substituted $MAPbBr_3$ (b, e), and chlorine-substituted $MAPbBr_3$ (c, f). In upper-right corners of (d-f) the crystal structure is overlaid and the unit cell is denoted by a solid square. Unit cell size is unchanged after substitution. The Br^-, Cl^- and I^- sizes were enlarged by a factor of 4.5 to emphasize the halide pair pattern. g) A schematic drawing of PbI_2 dissociation at the $MAPbBr_3$ surface followed by iodide substitution. An analogous process occurs for $PbCl_2$. Imaging parameters: a) V=1.3 V, I=80 pA; b) V=2.0 V, I=120 pA; c) V= -1.9 V, I=19 pA. Image size: a-c) 2.3×2.3 nm^2.

Adapted and reproduced with permission from Ref. 199. Copyright 2019, American Chemical Society. The thesis author was a co-author and contributed to sample preparation, STM and XPS data acquisition and overall data interpretation and analysis. Figures provided by and modified with permission from Dr. Jeremy Hieulle.

In order to examine the distribution and arrangement of substituted halides, larger area STM images were also acquired (Figs. 4.2a-c). For the mixed halide samples, many protrusions which are brighter (Fig. 4.2b) and darker (Fig. 4.2c) were seen to be randomly distributed across the perovskite surface. This random nature of the I^- and Cl^- substitution was confirmed via fast Fourier transform analysis of the images (inset, Figs 4.2a-c). The lack any additional bright spots in the low-k region for the $MAPbBr_{3-y}I_y$ and $MAPbBr_{3-z}Cl_z$ samples in comparison to the pure $MAPbBr_3$ sample indicates there was no low-frequency, long-range order of the substituted halide species.

The larger area images also enabled a statistical analysis of the apparent height distribution. Histograms of the apparent height distribution in each image (Figs. 4.2d-f) show that there was only one peak for $MAPbBr_3$, but that a clear second peak appeared for $MAPbBr_{3-y}I_y$ and a pronounced shoulder was evident in the distribution for $MAPbBr_{3-z}Cl_z$, which arises from a Cl peak. Although the lateral position of the halide was not changed by substitution, DFT calculations did confirm the experimental observation of a change in the substituted halide's vertical position compared to the Br plane of $MAPbBr_3$ (Figs. 4.2g-i). It should be noted that in addition to the vertical position shift, the differing ionic radii of the substituted halides also contributes to the observed change in apparent height in the STM images.

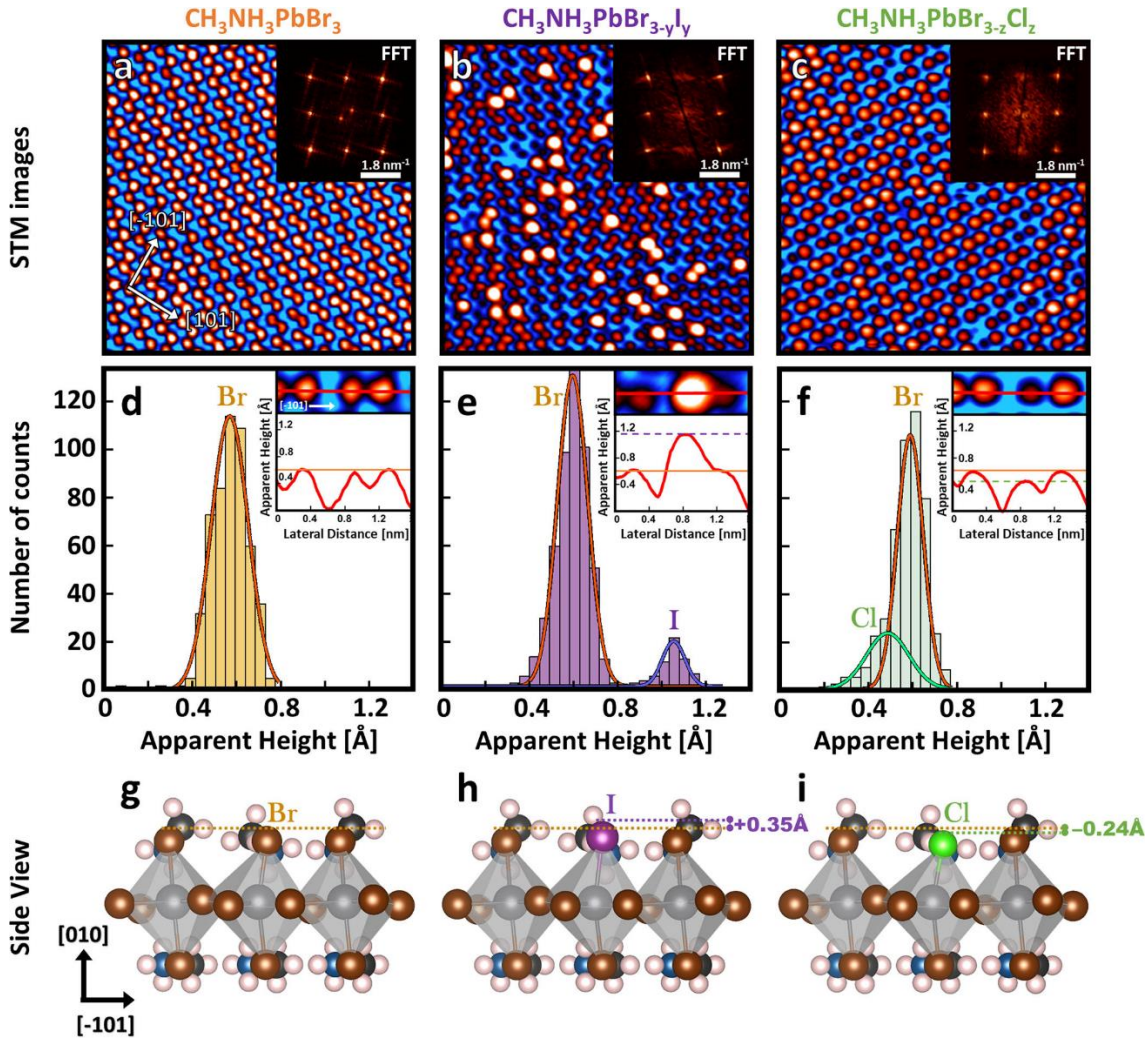

Figure 4.2 Position and height distribution of substituted halides in $MAPbBr_{3-y}I_y$ and $MAPbBr_{3-z}Cl_z$. a-c) Large area STM images of (a) $MAPBr_3$, (b) $MAPbBr_{3-y}I_y$ and (c) $MAPbBr_{3-z}Cl_z$ showing random distribution of substituted halides. Inset: FFT of each image confirming the lack of long-range order in the images. d-f) Histograms of height distributions for each perovskite sample. (Inset) Representative line profile for each sample showing apparent height difference between the substituted halide and the Br plane. g-i) Side view of crystal structure from DFT simulations showing the calculated difference in vertical position of the substituted halides. Imaging parameters: a) V=1.3 V, I=80 pA; b) V=2.0 V, I=120 pA; c) V= -2.0 V, I=100 pA. Image size: a-c) 10.0×10.0 nm^2.

The overall arrangement of substituted halides was found to be random over a large area. Within this random arrangement there were a few different phenomena involving multiple halide substitutions in adjacent lattice positions. For both $MAPbBr_{3-y}I_y$ and $MAPbBr_{3-z}Cl_z$, double substitution in the same halide pair (Figs. 4.3a and e), double substitution in adjacent halide pairs

Adapted and reproduced with permission from Ref. 199. Copyright 2019, American Chemical Society. The thesis author was a co-author and contributed to sample preparation, STM and XPS data acquisition and overall data interpretation and analysis. Figures provided by and modified with permission from Dr. Jeremy Hieulle.

along both the [-101] direction (Figs. 4.3 b and f) and [101] direction (Figs. 4.3c and g), and clustered triple substitution (Figs. 4.3d and h) were observed. DFT calculations comparing the single substitution and the double substitution in a single halide pair scenarios found that the energy of formation for two separate Cl-Br (I-Br) halide pairs is less than that for a Cl-Cl (I-I) pair. This energetic preference for separated substitution sites explains why large halide-substituted domain are not formed and is consistent with the disordered distribution seen in the large area images.

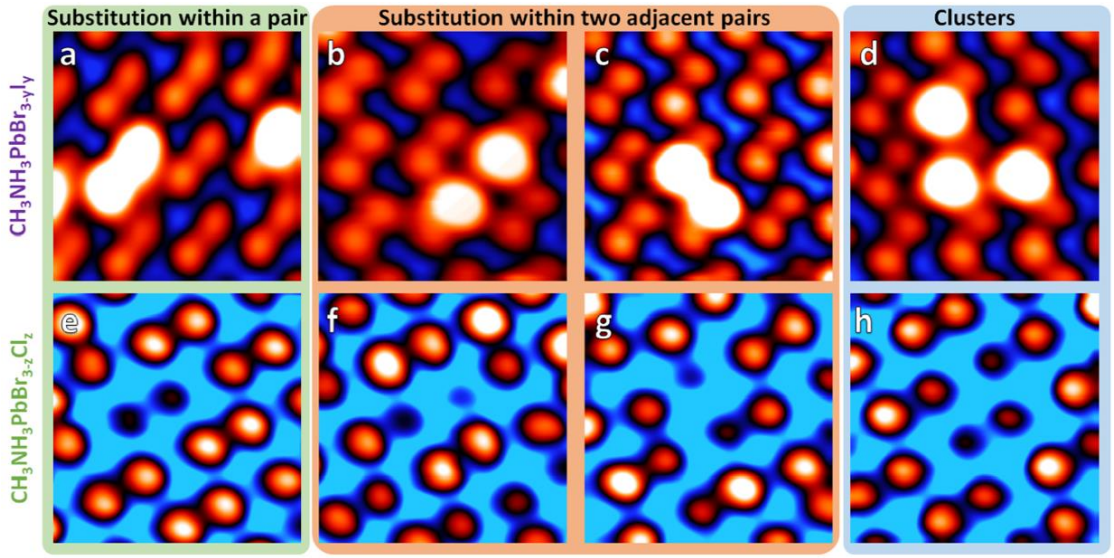

Figure 4.3 Adjacent halide substitutions. Double halide substitution in the same pair (a, e), in adjacent pairs along the [-101] (b, f) and [101] (c, g) directions, and triple substitution clusters for iodide and chloride substitution cases, respectively. Imaging Parameters: a-d) V= 2.0 V, I= 120 pA; (e-h) V= -2.0 V, I= 100 pA. Image size: a-h) 2.2×2.2 nm^2.

4.4 UPS measurements of mixed halide perovskites

The changes in electronic properties caused by halide substitution were invested with UPS. Work functions were determined from the secondary electron cutoff of the UPS spectra (Fig. 4.4a). Substitution of Cl^- resulted in a work function of 4.57 eV for $MAPbBr_{3-z}Cl_z$, lowered by 0.2 eV compared to $MAPbBr_3$. In contrast, substitution of iodine yielded a work function of 4.79 eV, nearly the same as the 4.77 eV pure $MAPbBr_3$. DFT calculation determined the work function change is a result of a shift in the vacuum level (not shown) caused by surface dipole modification after halide substitution. The potential to modify both the work function and the vacuum level

through halide substitution provides engineers with an interesting avenue for controlling energy level alignment between adjacent layers in a device.

Six different peaks can be identified in the valence band region of the UPS spectra for the different perovskite samples (Fig. 4.4b). A significant change in the valence band line-shape occurs both the $MAPbBr_{3-y}I_y$ and $MAPbBr_{3-z}Cl_z$, samples compared to pure $MAPbBr_3$. DFT calculations for pure bromide perovskite revealed that the VB is dominated by Br *4p* states (Fig. 4.4c). For the mixed halide perovskites, calculations were performed for the cases where the surface layer is completely substituted by either I^- or Cl^-. Contributions to the VB from iodine for $MAPbBr_{3-y}I_y$ were at binding energies comparable to or slightly lower than bromine, depending on the individual Br 4p orbital, whereas contributions from chlorine for $MAPbBr_{3-z}Cl_z$ were at higher binding energies than bromine (Fig. 4.4c). This is consistent with the higher stability found for Cl-substituted perovskite, which will be further discussed in Section 4.5.

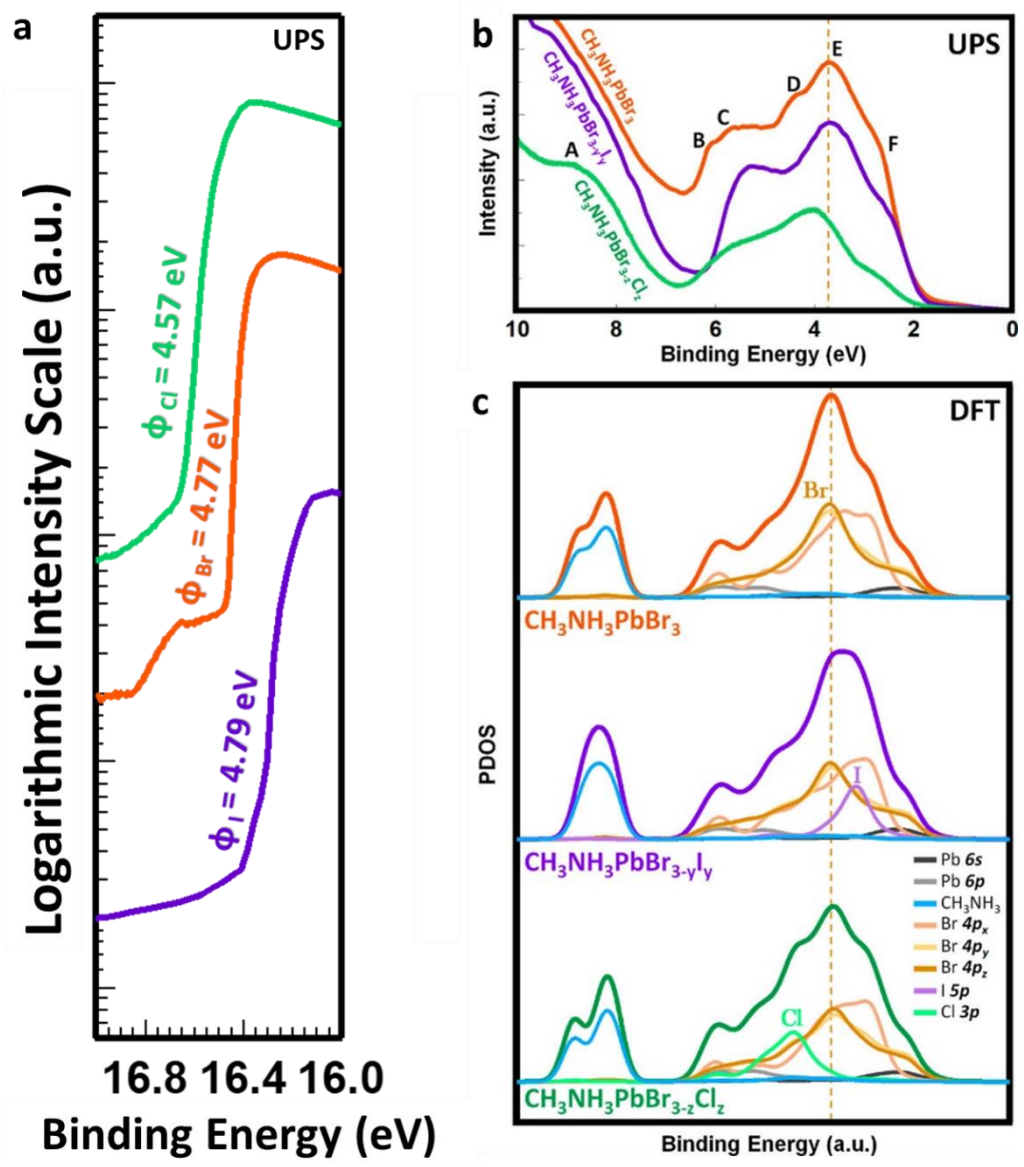

Figure 4.4 Analysis of work function and valence band by UPS and DFT. Secondary electron cutoff region (a) and valence band region (b) of UPS spectra for $MAPbBr_3$ (orange), $MAPbBr_{3-y}I_y$ (purple) and $MAPbBr_{3-z}Cl_z$ (green), showing changes in work function and valence band. (c) Valence band PDOS calculated via DFT. The thicker curves represent the total contribution of all component orbitals shown. PDOS was calculated for a complete substitution of the surface layer of the perovskite.

Adapted and reproduced with permission from Ref. 199. Copyright 2019, American Chemical Society. The thesis author was a co-author and contributed to sample preparation, STM and XPS data acquisition and overall data interpretation and analysis. Figures provided by and modified with permission from Dr. Jeremy Hieulle.

4.5 Stability of mixed halide perovskite surfaces

In order to correlate the effects of halide mixing on both the electronic properties and the stability of $MAPbBr_3$, the decomposition energy and the band gap was calculated by DFT as a function of % halide substitution of the surface layer (see Ref. 199 for calculation details). For $MAPbBr_{3-y}I_y$, increasing iodide substitution results in a sharp, monotonic decrease in decomposition energy (i.e. a decrease in stability) accompanied by a slight decrease in the band gap (purple and orange curves, respectively, Fig. 4.5a). However, $MAPbBr_{3-z}Cl_z$, exhibits a different trend. An increase in decomposition energy (i.e. an increase in stability) occurs for low Cl substitution below 25%. Importantly, there is no significant widening of the band gap in this low Cl substitution range, which would negatively affect photovoltaic device performance. Given the initial increase in the decomposition energy, it is expected that judicious Cl incorporation should result in higher stability against temperature, X-ray beam damage, and other external factors.

The level of Cl substitution is critical, as the decomposition energy decreases sharply when exceeding 25% Cl-substitution. This complex behavior can be attributed to the balance of two competing factors. On the one hand, the initial increase in stability can be related to relative bond strengths, where the Pb-Cl bond is stronger compared to that of Pb-Br and Pb-I.[228] On the other hand, excessive incorporation of the smaller Cl ion introduces a level of strain in the lattice that outweighs the positive effect of the superior Pb-Cl bond strength. This results in a net decrease in decomposition energy (i.e., material stability). This is proposed to be trend that holds in general when a smaller halide with stronger Pb-X bond strength is substituted into a perovskite, with the exact optimal substitution ratio changing depending on the balance of the gain in bond strength and the severity of lattice strain (i.e., the difference in ion size). Although the cases presented here focus on the surface layer, both of these factors, bond strength and lattice strain, should have a similar counterbalancing influence even in the bulk of the material. Considering this, the results presented here support the idea that there also exists an ideal bulk Cl-substitution ratio that imbues higher stability without a detrimental widening of the perovskite's band gap.

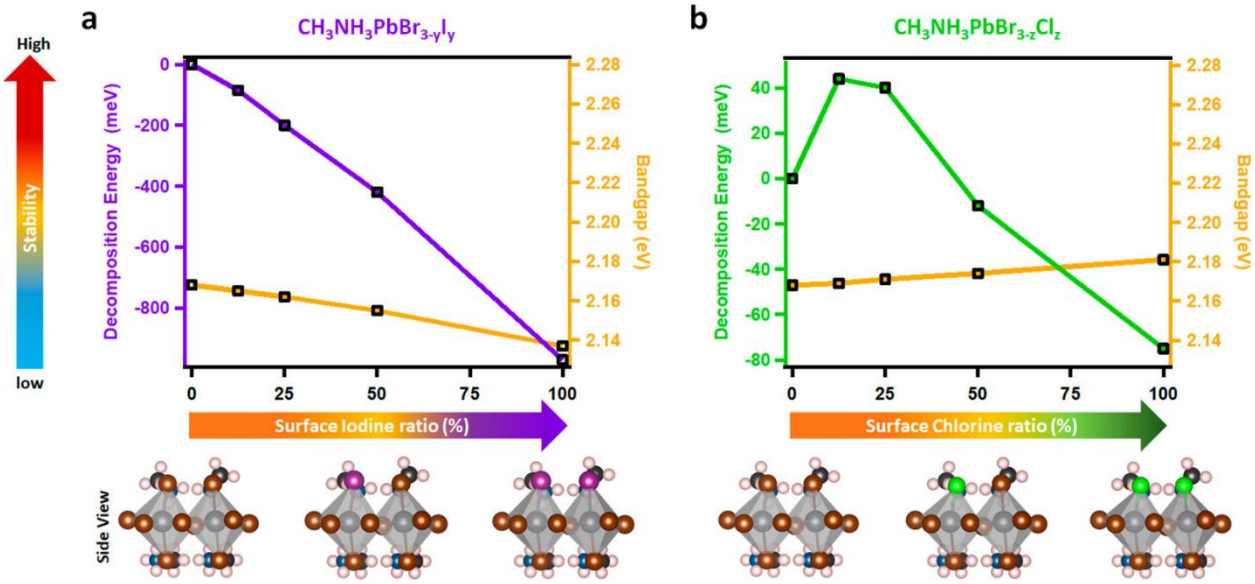

Figure 4.5 Decomposition energy and band gap of mixed halide perovskites. Decomposition energy (purple and green curves, respectively) and band gap (orange curves) as a function of surface halide substitution ratio for (a) $MAPbBr_{3-y}I_y$ and (b) $MAPbBr_{3-z}Cl_z$. Bottom panels show the near-surface structure of the 0%, 50% and 100% substituted scenarios. Color code: Same as Figure 4.1.

To test the relationship between Cl substitution and stability, XPS spectra of $MAPbBr_{3-z}Cl_z$ films in a half solar cell architecture (PVK/TiO_2/FTO/Glass) were monitored over time. After fabrication of a half-cell with a 300nm $MAPbBr_3$ film (see Ref. 199 for details), the half-cell was introduced to the UHV system. $PbCl_2$ was then evaporated onto the half-cell to create the $MAPbBr_{3-z}Cl_z$ mixed halide perovskite films. The Pb 4f signal of samples with a 0%, 12% and 18% Cl substitution ratio at the surface was monitored over time (Figs. 4.6a-c, respectively). These ratios were calculated from the ASF-corrected Cl:Br peak area ratio in the t=0 XPS spectra. The appearance of Pb(0) oxidation state peaks was used here as a measure of perovskite degradation, as it has been previously associated with perovskite decomposition.[229]

The Pb 4f signal initially consists of two peaks originating from the spin orbit split $4f_{7/2}$ and $4f_{5/2}$ peaks, seen centered at 137.9 eV and 142.8 eV, respectively, in the top curve of Figure 4.6a. These peaks are assigned to the Pb^{2+} oxidation state expected from lead in perovskite. In the curve immediately below, measured after the $MAPbBr_3$ half-cell had been stored in UHV for 4h, small peaks attributable to the Pb(0) oxidation state appear at slightly lower binding energies than the Pb^{2+} peaks, consistent with literature.[229] The intensity of the Pb(0) peak increases steadily over time, indicating further deterioration of $MAPbBr_3$. After Cl incorporation, the onset of the

Adapted and reproduced with permission from Ref. 199. Copyright 2019, American Chemical Society. The thesis author was a co-author and contributed to sample preparation, STM and XPS data acquisition and overall data interpretation and analysis. Figures provided by and modified with permission from Dr. Jeremy Hieulle.

degradation was delayed and the severity of the degradation lessened. For 12 % Cl substitution at the surface, Pb(0) peaks appeared after 28h (Fig. 4.6b and d). A more pronounced delay was seen for the 18% Cl substitution sample, which developed Pb(0) peaks only after 116h (Fig. 4.6c and d). In Figure 4.6e, the area of the Pb^{2+} peaks is used as a measure of the remaining, not degraded perovskite. This analysis shows that not only was the degradation onset delayed, but the extent of degradation after a given amount of time was suppressed. A similar phenomenon is expected for Cl incorporation into $MAPbI_3$, possibly with a narrower peak than Fig. 4.6b since a steeper slope would be expected both for the stability increase and subsequent decrease considering the larger magnitude of the difference in Pb-X bond strength and halide ion size, respectively. Overall, these findings shed light on the effect of chlorine mixing on stability and provided some guidance on the how to best utilize chlorine to optimize perovskite-based devices.

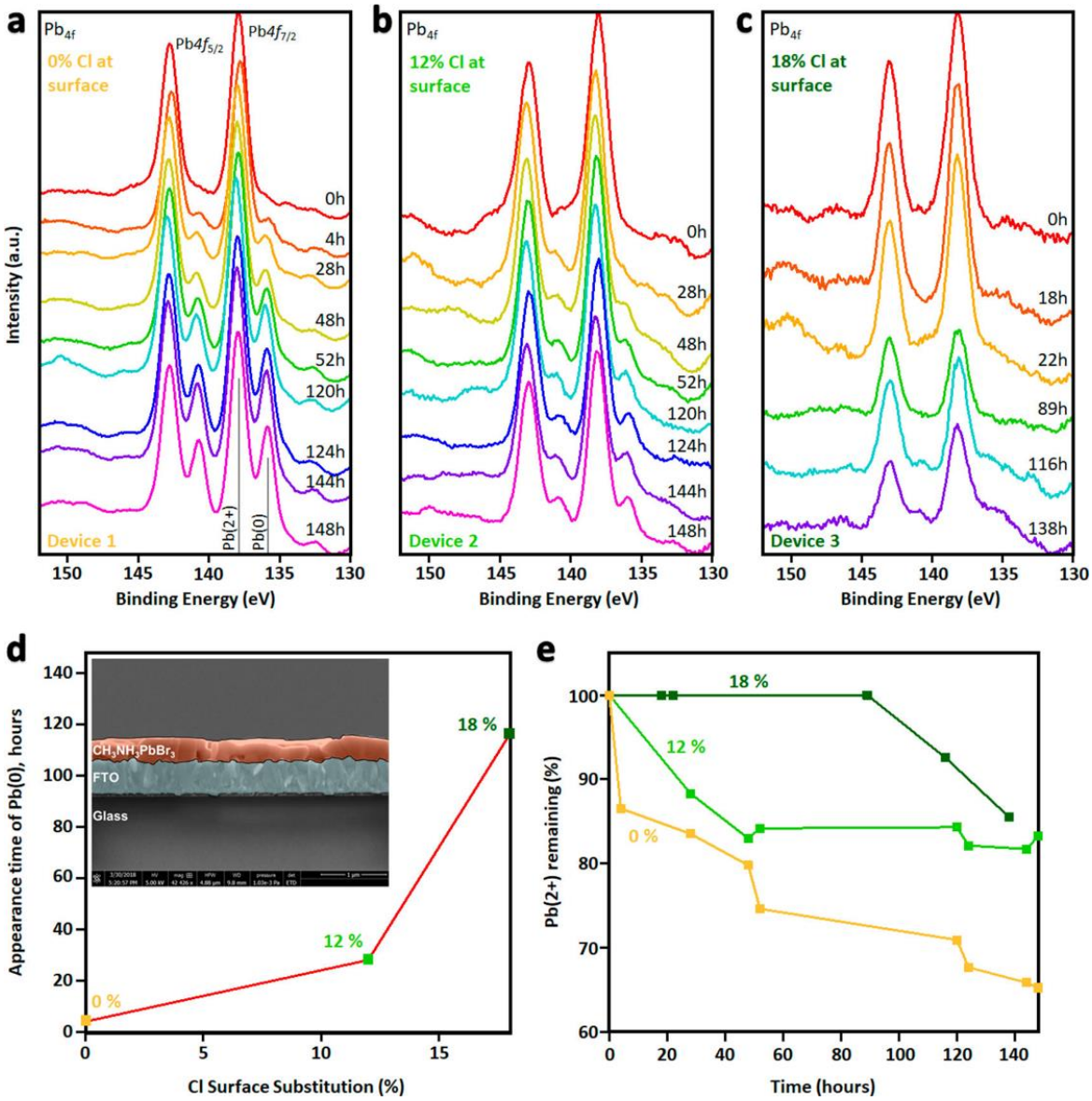

Figure 4.6 Effect of Cl substitution on perovskite half-cell stability. The Pb 4f XPS spectra of $MAPbBr_3$-based half-cell devices with (a) 0%, (b) 12% and (c) 18% Cl substitution at the surface monitored over time. d) Appearance time of Pb(0) peak as a function of Cl substitution raito. e) Percentage of initial Pb^{2+} peak intensity remaining as a function of time for different Cl substitution ratios.

4.6 Summary

In this chapter, the atomic structure of the surface of the mixed halide perovskites $MAPbBr_{3-y}I_y$ and $MAPbBr_{3-z}Cl_z$ was determined in real space by STM imaging and was corroborated by DFT simulations. Both iodine and chlorine were found to substitute at bromine

Adapted and reproduced with permission from Ref. 199. Copyright 2019, American Chemical Society. The thesis author was a co-author and contributed to sample preparation, STM and XPS data acquisition and overall data interpretation and analysis. Figures provided by and modified with permission from Dr. Jeremy Hieulle.

lattice locations after sublimation of the corresponding lead halide onto the $MAPbBr_3$ surface. Many adsorption and substitution scenarios were tested via DFT and individual halide substitution best reproduced the experimental STM images. The substituted halides did not form large substituted domains, but rather had a disorder distribution which was confirmed by FFT analysis of large area STM images. This finding was further supported by comparison of DFT calculated formation energies for single substitutions and for substitution pairs.

UPS measurements revealed that halide mixing is a viable strategy for modifying the work function of the perovskite, and DFT calculations revealed that this stems from a shift in the vacuum level. Fine control of these two parameters is of key interest to device engineers optimizing the energy level alignment between adjacent layers in a device. Modification of the valence band was also observed via UPS, and DFT calculations showed that the valence band is dominated by contributions from the Br 4p orbitals.

The effect of halide substitution on stability was investigated by DFT and then confirmed experimentally by XPS. DFT calculations showed that low levels (below 25%) of Cl substitution induce an increase in the perovskite's stability without causing a detrimental widening of the bandgap. This finding was confirmed experimentally via monitoring the appearance and evolution of Pb(0) peaks in the Pb 4f XPS spectra as a function of time for various Cl substitution ratios. Both 12% and 18% Cl substitution at the surface was found to provide an increase in stability compared to the pure $MAPbBr_3$ perovskite. DFT calculations showed that this stability increase at low Cl substitution ratios is due to the higher Pb-X bond strength of chlorine. However, Cl substitution higher than 25% caused a decrease in stability due to lattice strain induced by incorporation of the smaller sized ion. The counterbalance of these two factors results in the existence of an optimal Cl substitution ratio for stability improvement. A similar trend can be expected for Cl substitution in $MAPbI_3$, although a narrower peak is expected around the optimal ratio due to the higher difference in Pb-X bond strength and ion size. The identification of an optimal Cl substitution ratio and its origin provides device engineers with useful fundamental insight and an interesting avenue for optimization of perovskite-based solar cells and other devices.

Chapter 5: The $MAPbX_3$/CuPc interface

5.1 Introduction

In previous chapters, the surfaces of methylammonium-based lead halide perovskites were explored. Although understanding the surface properties of these systems is important, the perovskite surface only constitutes half of an interface that would occur in a photovoltaic device. Solar cells typically have the OHP absorber layer sandwiched between two CSLs, an ETL and an HTL. The interfaces between the perovskite layer and these CSLs are potential areas of higher charge recombination.[121, 193] Interfacial engineering via passivation of the perovskite surface has proven a viable strategy for improving device performance. Additionally, studies have found that non-stoichiometric precursor ratios, achieved during the perovskite film preparation[230] or via post-annealing treatment,[50] can significantly affect performance. Such non-stoichiometric ratios in the perovskite material are expected to strongly impact the interfacial properties. Using thin interlayers of MAI precursor at the perovskite interface was also shown to be a useful method for tuning energy level alignment at the interface between the OHP layer and the HTL.[53] Proper engineering of these interfaces can also result in increased stability.[145] Obtaining a clear understanding of the perovskite/CSL interface is crucial for rational interface engineering and further device improvement.

Transition metal phthalocyanines (TMPcs) have been identified as viable hole transport layers (HTLs) that feature a higher thermal stability than spiro-MeOTAD.[60-63, 65] TMPcs have also been utilized as additives in HTLs.[231] Undoped copper phthalocyanine (CuPc) derivatives have been shown to enable PCEs up to 18.8% in OHP-based solar cells.[66] CuPc itself has shown excellent compatibility with low-cost carbon electrodes as well, both as a distinct HTL[232] and as an additive in the carbon electrode,[81] resulting in performance increases. Furthermore, the relatively hydrophobic nature of CuPc enables it to act as a blocking layer from moisture in the environment, delivering impressive stability for unencapsulated devices.[60, 61, 232] Thus, CuPc was chosen for this investigation as an HTL with the potential to increase the thermal and moisture stability of OHP solar cell devices.

Here, utilizing two materials well-suited for STM study, we investigate an OHP/HTL interface by examining sub-monolayer CuPc sub-monolayers deposited on perovskite thin films. In contrast to previous chapters, the bulk of the data and discussion for this chapter are regarding the iodide perovskite, $MAPbI_3$, although a qualitatively similar interface was found for $MAPbBr_3$ as well. We reveal that CuPc forms a self-assembled layer on $MAPbI_3$ and that it behaves very differently on domains of precursor that may exist in non-stoichiometric perovskite films. This differing behavior has important consequences for interfacial properties and charge transfer in devices.

5.2 Methods

$MAPbI_3$ films were prepared in UHV by co-evaporation of PbI_2 and MAI at 513K and 378K, respectively, for 5 minutes onto a cleaned Au(111) substrate held at 130K (see Section 2.2 for details). Samples were annealed at room temperature for at least 3 hours before being transferred into the STM setup. After the success of the perovskite deposition was confirmed via STM imaging, the sample was transferred in UHV to a preparation chamber where CuPc was deposited onto the perovskite sample. The commercial CuPc powder (Sigma Aldrich, triple sublimated grade) was further purified by vacuum sublimation *in situ* before performing any deposition. CuPc was deposited via vacuum sublimation using a K-cell at 638K for varying durations to achieve different coverages. The perovskite/Au(111) substrate was held at room temperature during this deposition, and the sample was transferred to the STM chamber without any further treatment. During CuPc deposition, the chamber pressure was 6×10^{-8} torr. Narrow-mouthed crucibles were used, and a shutter was used to prevent unintended deposition onto the sample during transfer within the preparation chamber.

Some issues occurred during initial trials of CuPc deposition that are worth mentioning. When the crucible was filled with only a small amount of CuPc (approximately ¼ of the total volume of the crucible), a blocking layer of CuPc would form near the top of the crucible. This was due to the shape of the filament wrapping around the crucible, which resulted in a temperature gradient where the top of the crucible was cooler than the bottom, allowing the sublimated CuPc to re-condense on the top of the crucible, eventually forming a blocking layer. This phenomenon was also exacerbated by having the shutter of the K-cell closed over the crucible during temperature ramping. To remedy these issues, CuPc was filled almost to the top of the crucible, so

that sublimation would not start until the entire crucible had reached the sublimation temperature. Additionally, the K-cell shutter was left open during temperature ramping so that any material sublimated during the ramping would not collect near the mouth of the crucible. The shutter was only closed for the 2-3 minutes immediately before deposition, while the sample was being transferred into the deposition chamber.

5.3 Adsorption of Single CuPc on $MAPbI_3$

An initial deposition of 30 sec of CuPc was performed on an $MAPbI_3$/Au(111) sample. First, we will examine the behavior of a single, isolated CuPc adsorbed on the $MAPbI_3$ surface (Fig. 5.1a). A zoomed-in image of the CuPc (Fig. 5.1b) shows eight round outer orbitals, which surround eight smaller, inner orbitals, which are somewhat tapered in shape. This intramolecular contrast is indicative of the highest occupied molecular orbital (HOMO) of CuPc.[157] This image also shows the face-on CuPc adsorbed so that its pairs of outer orbitals are aligned along the same [10±1] directions as the I^- pairs of the $MAPbI_3$ substrate (solid white and yellow lines). The molecular dimensions are such that perfect overlap between the CuPc orbitals and the I^- lattice sites is difficult. For example, in Figure 5.1b, the CuPc outer orbital pair highlighted by the solid yellow line matches well the underlying substrate lattice, but the orbital pair highlighted by the solid white line is offset from the underlying I^- pair. It was also observed that the CuPc molecule can adsorb 45° rotated relative to the halide pairs (Fig. 5.1c), along the high symmetry [100] and [001] directions. The molecular width was measured along two axes (Fig. 5.1d), and values of 1.65nm and 1.59nm were obtained, which are consistent with the range of values found in literature. The widths of these two axes are mentioned because they correspond to the expected heights for a vertically adsorbed CuPc molecule for the cases of single and double isoindole group adsorption (dashed white and yellow lines, respectively).

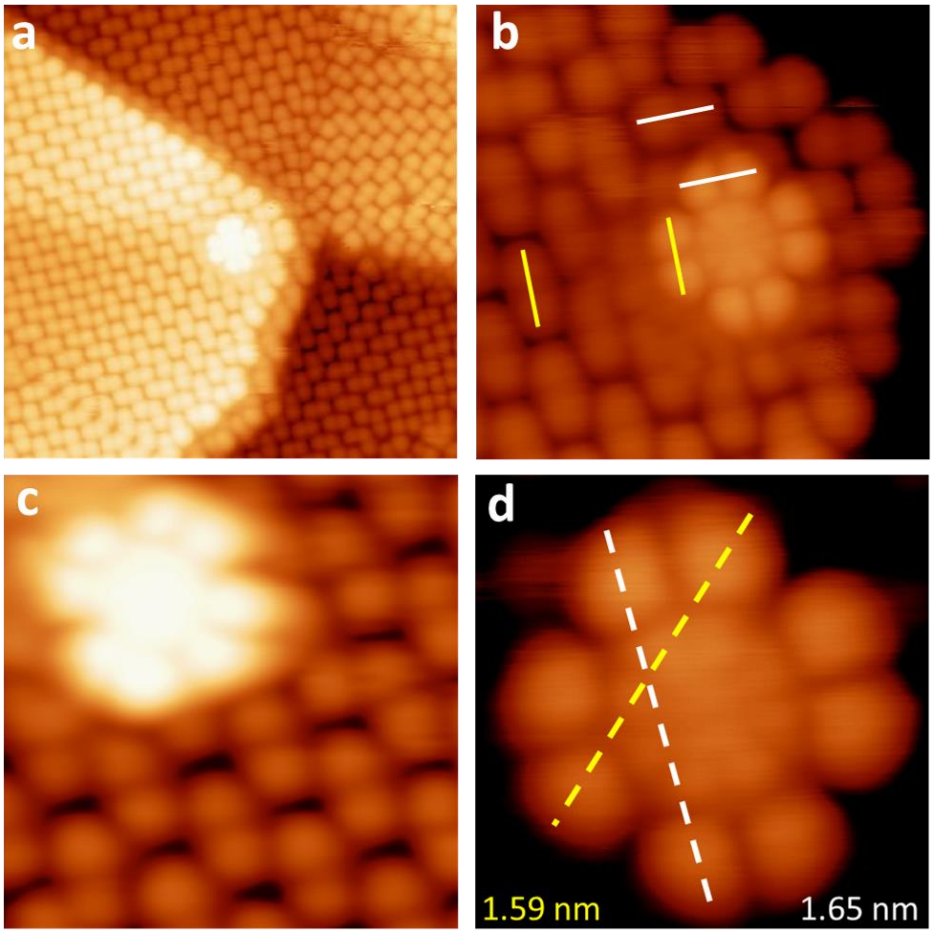

Figure 5.1 An individual CuPc molecule adsorbed on the $MAPbI_3$ surface. a) Overview image of a single, isolated CuPc molecule adsorbed on the (010) $MAPbI_3$ surface. b) Close up image showing the HOMO state of the CuPc and its face-on adsorption. The adsorption orientation relative to the substrate is denoted by solid white and yellow lines. c) Alternate adsorption orientation of CuPc where outer orbital pairs align with [100] and [001] directions. d) Measurements of the CuPc width along different axes. Image Sizes: a) 15.2×15.2 nm^2 b) 4.8×4.8 nm^2 c) 3.7×3.7 nm^2 d) 2.0×2.0 nm^2. Imaging parameters: a,b,d) V = -2.7 V, I = 300 pA; c) V = -2.5 V, I = 200 pA.

Additionally, it was found that the face-on adsorbed CuPc molecule was easily moved by the STM tip. In Figure 5.2, the STM tip is scanning from the top of the image to the bottom, and the CuPc molecule is gradually dragged toward the bottom by the tip. The ease with which the molecule is moved by the tip suggests a relatively weak molecule-substrate interaction between CuPc and $MAPbI_3$. Although of fundamental interest, the single molecule, face-on adsorption

scenario is extremely rare on $MAPbI_3$. The more common adsorption behavior of CuPc will be discussed in the next section.

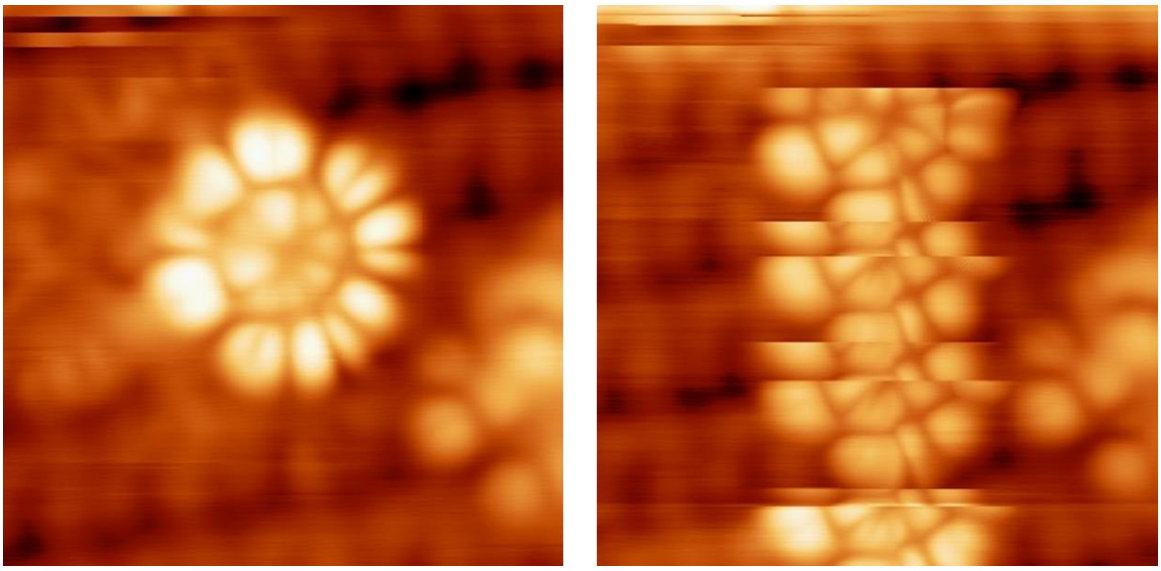

Figure 5.2 Mobility of a face-on adsorbed CuPc molecule on $MAPbI_3$. a) Upward scan of a CuPc molecule face-on adsorbed on $MAPbI_3$. Misshapen molecular orbitals are an artifact due to a non-ideal tip shape. b) Downward scan of the same molecule as in (a). The molecule is dragged by the STM tip in the direction of the scan. Image Size: 3.6×3.6 nm^2. Imaging parameters: V = -2.6 V, I = 150 pA.

5.4 Self-assembled (SA) layer of CuPc on $MAPbI_3$

After the initial 30 s deposition, sub-monolayer CuPc coverage was achieved. It was found that CuPc preferentially forms a self-assembled (SA) layer on $MAPbI_3$. In Figure 5.3a there are multiple $MAPbI_3$ grains exhibiting the previously reported paired surface reconstruction.[151] In the middle of the image there is a brighter, striped domain, which is attributed to an SA layer of CuPc molecules.

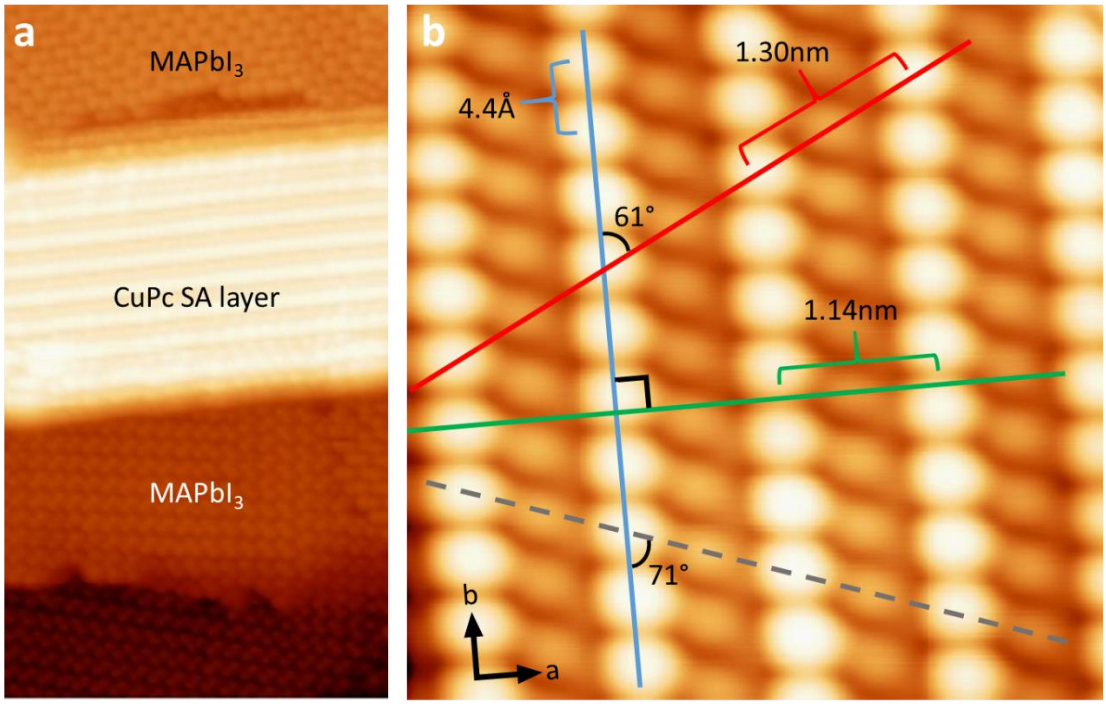

Figure 5.3: CuPc self-assembled (SA) layer on $MAPbI_3$ surface. a) Overview image showing a CuPc SA layer on top of $MAPbI_3$. b) Close-up view of a CuPc SA layer showing the alternating rows of bright and dark protrusions. Colored lines show directions of interest, with corresponding colored brackets denoting distances. Angles relative to the b-direction are noted. Image Sizes: a) 16.4×29.7 nm^2 b) 4.5×4.5 nm^2. Imaging parameters: a) V = -2.7 V, I = 100 pA; b) V = -2.6 V, I = 150 pA.

A zoomed-in image on one of these domains (Figure 5.3b) reveals there is an alternation between rows of brighter protrusions and rows of darker protrusions when going across an SA layer. The direction perpendicular to these rows will be referred to as the a-axis of the SA layer. The direction parallel to the bright and dark rows will be referred to as the b-axis. Finally, the normal to the perovskite substrate will be referred to as the c-axis. To further characterize the SA layer, the periodicities along directions of interest were measured, as shown in Fig. 5.3b. An average of 17 measurements of distinct instances of the SA layer yield periodicities of 4.4 ± 0.2 Å along the b-axis and 1.14 ± 0.04 nm along the a-axis. Additionally, a survey of images showed that there is no preferred direction of the $MAPbI_3$ film along which the CuPc SA layer aligns itself, once again indicating a relatively weak molecule-substrate interaction.

To provide context to the analysis and discussion of the experimental results, it is important to note that CuPc is polymorphic in nature. As mentioned in Section 2.6, multiple distinct

polymorphs have been reported.[161, 233] A reasonable starting point is to assume that the CuPc SA layer that forms on top of $MAPbI_3$ is one of these crystalline polymorphs. Initially, the β-phase and the α-phase of CuPc are considered, as they are the only two polymorphs for which detailed information on the stacking pattern of CuPc molecules is known. The β-phase is thermodynamically stable, and features b-axis periodicity of 4.8Å and a stacking angle relative to the b-axis of approximately 45°. The α-phase of CuPc has been known to form when films of CuPc are vapor deposited, and features b-axis periodicity of 3.8Å and a stacking angle of approximately 63°. Comparing these stacking angles to the CuPc layers formed on $MAPbI_3$, it was found there is no periodic topographic pattern along a 45° stacking angle, eliminating the β-phase as a candidate. However, there is periodicity along an angle of 61 ± 2° (red line, Fig. 5.3b), which is consistent with α-phase CuPc. By measuring the periodicity along this 61° stacking angle, a value of 1.30 ± 0.05 nm is obtained. Because stacking in α-phase CuPc does not show any intermolecular overlap in the a-direction (Fig. 2.8), the entire width of the CuPc would need to fit in this 1.30 nm periodic length. Although this value is a bit lower than the approximately 1.6 nm CuPc width measured here, it is nearly consistent with a 1.37nm width reported from LEED data.[234]

Comparing other SA layer dimensions, reported STM values of the a-axis periodicity for similar CuPc SA layers vary widely in the range of 1.18nm-1.69nm.[158-160] The 11.4Å a-axis periodicity (green line, Fig. 5.3b) measured in this study is relatively consistent with the lower end of this range, and slightly lower than the 1.20-1.31nm[158, 162] range found reported for a-axis periodicity of α-CuPc. The 4.4 Å b-axis periodicity (blue line, Fig. 5.3b) that was measured is larger than the reported 3.8 Å for α-CuPc,[158, 162] but matches extremely well with the 4.5 Å value reported by Sun et al.[160] Although there are characteristics of the CuPc SA layer on $MAPbI_3$ that are similar to α-CuPc, discrepancies exist that give reason to consider the possibility that this SA layer is a polymorph other than the α or β phase.

Another dimension to take into account is the c-axis, i.e., the height of the layer. An average height in the c-axis of 9.0 ± 0.7 Å was obtained over measurements of 13 different CuPc SA layers, with an example measurement shown in Figure 5.4. It should be noted that it is difficult to get accurate height measurements with STM because the measured apparent heights in STM are a convolution of geometric position and local density of states. Thus, the measured height values can vary depending on the gap voltage used during imaging. Slightly different voltages were used

for some of the images included in the above average, which may contribute to the variance. For comparison, when averaging height measurements of 6 SA layers all imaged at the same sample bias voltage of -2.7 V, a value of 8.6 ± 0.5 Å is obtained.

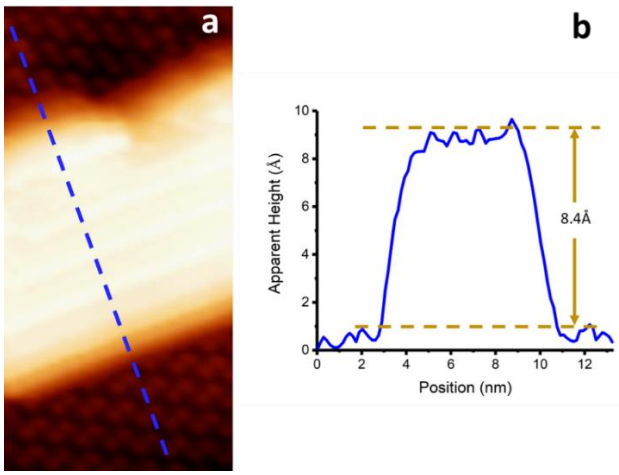

Figure 5.4: CuPc SA layer height a) STM image showing a typical CuPC SA layer on $MAPbI_3$. b) Height profile along the dashed blue line in (a). Image Size: a) 6.4×13.0 nm^2. Imaging parameters: a) V = -2.5 V, I= 200 pA.

Most models proposed in STM literature for similar CuPc films all consider edge-on adsorption of CuPc, although theoretical evidence to corroborate these models was not reported. For an edge-on adsorption model to be correct, an SA layer height close to the width of the face-on adsorbed CuPc would be expected. The expected height varies slightly depending on if one or two isoindole groups of the CuPc molecule are adsorbed on the surface (white and yellow dashed lines, Fig. 5.1c). Interestingly, the average SA layer height measurements of 8.6 Å and 9.0 Å are significantly less than the expected 1.4-1.7 nm height of an edge-on adsorbed CuPc. There are two possible explanations for this. The first is that the CuPc actually are stacking normal to the $MAPbI_3$ surface, but the measured apparent height value is strongly affected by some electronic effect. Because the apparent height measured by STM is a convolution of geometric position and local density of states, an electronic effect could be altering the apparent height to a value that does not represent the true physical height of the layer.

The second explanation is that the measured apparent height does represent the true physical height of the SA layer but that the CuPc molecules are adsorbed at some tilt angle, θ, relative to the $MAPbI_3$ film. Such a tilt angle can be estimated using the measured apparent heights

and basic trigonometric relations. Here, θ is approximated by $\theta=\arcsin((h-f)/w)$, where *h* is the apparent height of the CuPc SA layer, *f* is the apparent height of a flatly adsorbed CuPc, and *w* is the width of the flatly adsorbed CuPc molecule. A range of $19°<\theta<30°$ is obtained when using maximum and minimum measured values are used to create absolute upper and lower bounds. Using the average CuPc SA layer height value of 8.6Å, the 1.65nm CuPc width value from Figure 5.3b, and a range of values obtained for face-on CuPc height dimensions, a smaller tilt angle range of $24°<\theta<25°$ is obtained. Interestingly, these ranges are consistent with the experimental and theoretical results that Wang et al. obtained for SnPc on NaCl. In that study, molecular mechanics calculations were used to propose a model where SnPc molecules are adsorbed with a 25° angle relative to the substrate, which matches well their experimental value of 23° obtained via STM. Although that study uses a different TMPc than this work, it is feasible that the preferred tilt angle may be predominantly determined by the organic framework.

5.5 Defects in the CuPc SA layer

Analyzing the dimensions of the CuPc SA layer has given some insight about its structure, but further clues about the molecular stacking pattern can be gained by examining defects that occur in the layer. While the standard topographic pattern for the SA layer involves alternating bright and dark rows, there are some instances where there are differences in the brightness of the protrusions within a single row. This modulation within single row appears to have no discernable long-range order to its occurrence (Figure 5.5a). However, a high resolution image of defects shows a noticeable local pattern. In Fig 5.5b, it can be seen that every depression in the bright row (dashed yellow circles) is accompanied by a corresponding depression in the neighboring darker row (dashed green circles). Drawing a line through this pair of depressions, we find a stacking angle of 62° with respect to the b-direction of the SA layer (dashed black lines). This suggests that the two depressions in adjacent rows are part of one unit (i.e. belong to the same molecule). The fact that these paired depressions occur at an angle close to that of α-CuPc provides additional support to the hypothesis that the SA layer is actually α-CuPc.

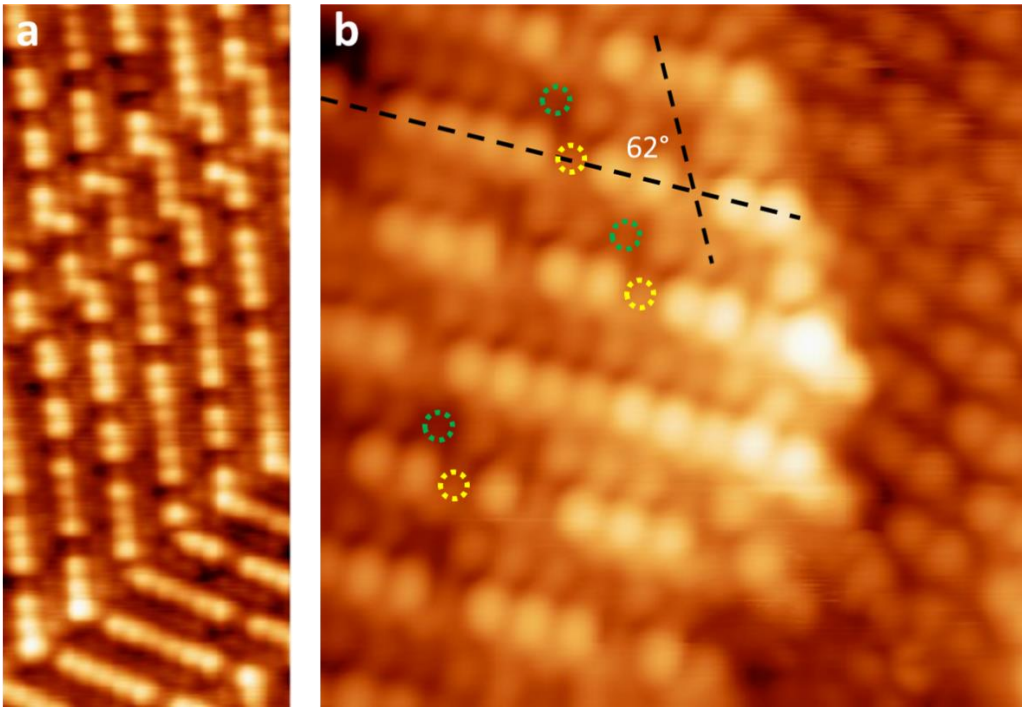

Figure 5.5 Defects in the CuPc SA layer on $MAPbI_3$. a) Image of the CuPc SA layer showing many defects in the rows of brighter protrusions. Note that there is no pattern to the frequency of defect occurrence. b) This image reveals that defects in the brighter rows (dashed yellow circles) are accompanied by defects in the darker rows (dashed green circles). The angle between the b-axis and the axis of the paired defects is denoted by dashed black lines. Image Size: a) 5.6 × 14.7 nm^2 b) 6.8 × 6.8 nm^2. Imaging parameters: a) V = -2.7 V, I = 100 pA b) V = -2.5 V, I = 71 pA.

Another peculiar irregularity of the CuPc SA layer is the zig-zag shape of the macrostructure, which features bends of 121 ± 2° (Fig. 5.6a). There is no apparent SA layer threshold width or length at which these bends occur. Similar bends have been previously reported for CuPc on Bi(111),[158] but it is not clear what triggers these bends to occur. However, the fact that the angle of the bend is approximately twice the stacking angle of α-phase CuPc gives a potential clue regarding the molecular arrangement at the bend. This suggests that the bend occurs due to the border of two domains of α-phase CuPc. Some evidence of this type of boundary arrangement can be gleaned by again looking at defects in the SA layer that occur near one of these bends.

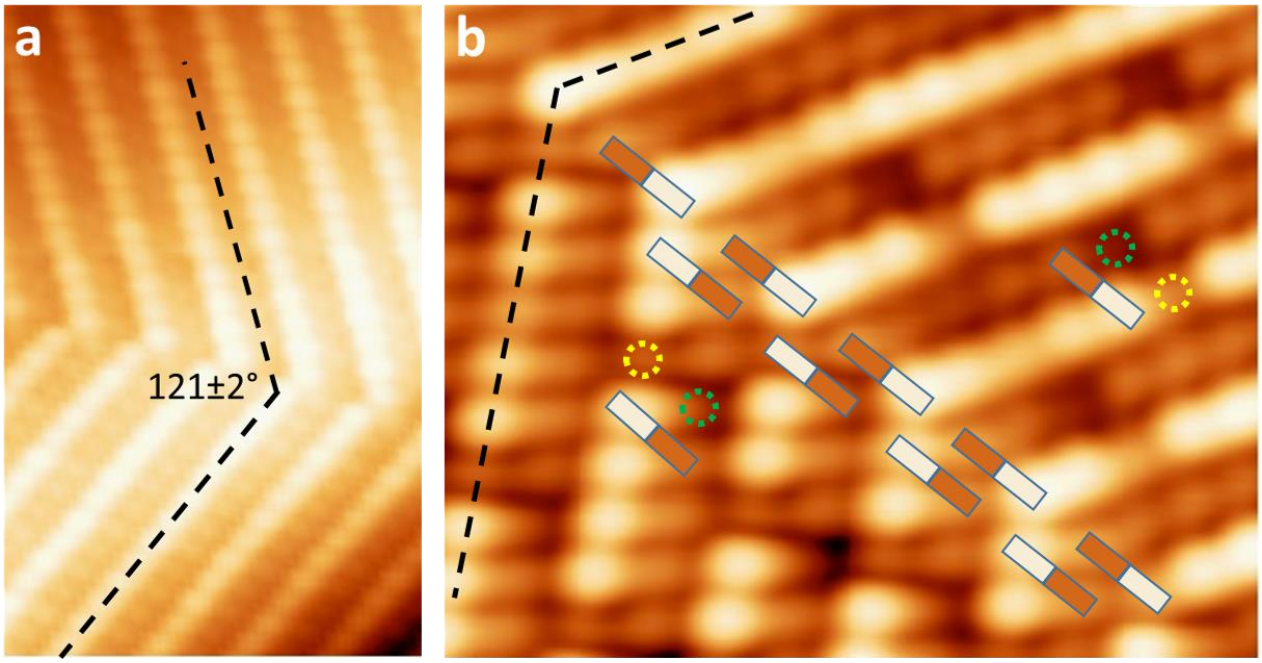

Figure 5.6 Molecular arrangement at a bend in the CuPc SA layer. a) Image of a macroscopic bend in the CuPc SA layer. Dashed black lines denote the angle of the bend. Note that the bright and dark rows are offset at the bend. b) Image of paired defects occurring near a bend in the CuPc SA layer. Depressions in the bright and dark rows are denoted by dashed green and yellow circles, respectively. The two-tone rectangles denote one CuPc molecule, and are shown at the bend to highlight that the two domains are offset by half of a molecule. Note that the bright and dark rows line up at the bend. Image Size: a) 6.6 × 10.3 nm^2 b) 6.1 × 4.8 nm^2. Imaging parameters: a) V = -2.5 V, I = 60 pA b) V = -2.6 V, I = 52 pA.

In Figure 5.6b, a zoom-in on a bend shows defects on both sides of the bend. The defects occur as pairs of depressions, with one depression in a bright row (dashed yellow circles) and an accompanying depression in the adjacent darker row (dashed green circles), just as in Figure 5.5. However, the orientation of these pairs is different on each side of the bend. On the right side of the bend, the accompanying depressions in the darker row are positioned above and to the left of the depressions in the bright row. In contrast, on the left side of the bend the accompanying depressions in the darker row are positioned below and to the right of the depressions in the bright row. This shows that the relative orientations of the paired defects, which are being tentatively interpreted as individual, depressed CuPc molecules, are rotated by 180°. This enables molecules to tightly pack in an offset arrangement at the bend itself (tan and brown rectangles, Fig 5.6b). Additionally, if the two bends shown in Figures 5.6a and 5.6b are compared closely, it is evident that there is a different arrangement occurring at each bend. In Figure 5.6b the bright and dark

rows on each side of the bend line up with each other, whereas Figure 5.6a they are offset from each other. For that offset row arrangement the model is similar as Figure 5.6b, except the molecules on each side of the bend line up with each other.

Having examined a few instances of defects in the CuPc SA layer, it is worth noting the possibility of Pb/Cu cation exchange between the perovskite layer and the SA layer, such that part of the CuPc SA layer may be composed of PbPc molecules. This could be an alternate explanation for some of the defects seen. Cu/Pb cation exchange has been reported for CuS/PbS tetrapod semiconductors under certain reaction conditions.[235] On the other hand, a study using CuI as an HTL in OHP solar cell devices showed evidence suggesting that there is no Cu/Pb cation exchange occurring, or that it is minimal in nature.[236] Nonetheless, this is a possibility that must be considered when analyzing the SA layer structure.

5.6 Behavior of additional CuPc on the 1st CuPc SA layer

Additional CuPc depositions were performed on the sample to increase coverage and examine the behavior of a 2nd layer of CuPc. After the initial 30 s deposition, subsequent depositions were performed up to a cumulative deposition time of 195 s. Two important results were obtained. First, the CuPc SA layers exhibit Volmer-Weber growth, also known as “island” growth. In this scheme, the second layer of a crystal forms before the 1st layer is completed. This can be seen in Fig. 5.7a, where a 2nd layer of CuPc is seen in the same image as bare $MAPbI_3$ substrate.

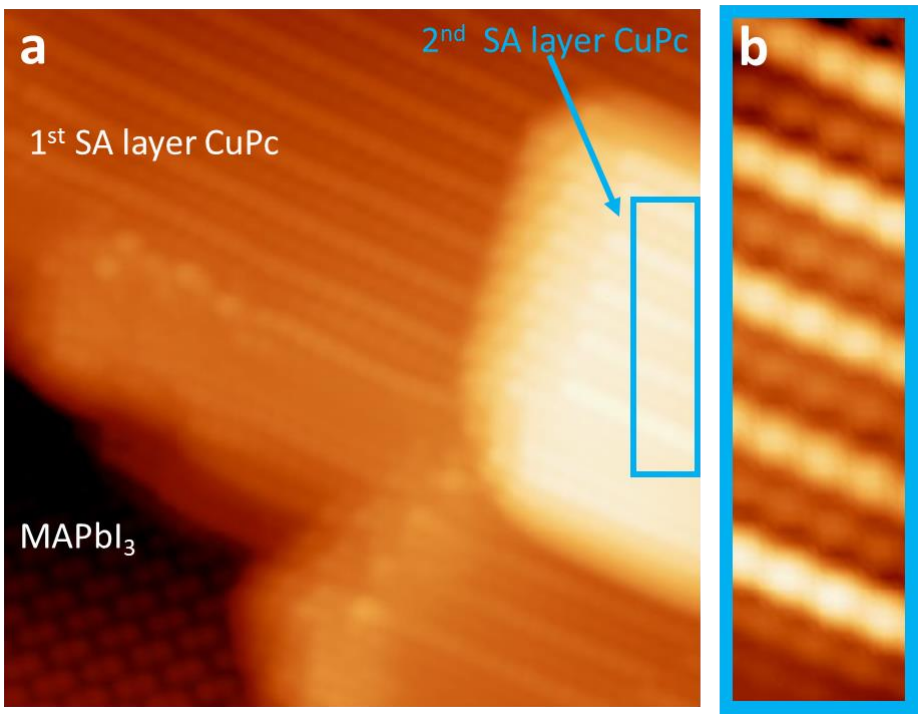

Figure 5.7 2nd layer CuPc SA layer a) Image showing Volmer-Weber or "island" type growth. The 2nd layer of CuPc has started growing while there is still a bare $MAPbI_3$ domain. b) Zoom-in on the 2nd layer of CuPc showing the same alternating bright-dark row structure. Image Size: a) 14.4 × 14.4 nm^2, b) 1.6 × 6.0 nm^2. Imaging parameters: a,b) V = -2.5 V, I = 100 pA.

The other notable finding is that the structure of the 2nd layer of CuPc is the same as the first one. Figure 5.7b shows the same bright-dark alternating rows as seen in the first layer. This means that there is no special orientation of the 1st layer that interfaces directly with the perovskite. This is consistent with the idea that the CuPc-$MAPbI_3$ interaction is weak in comparison to the intermolecular CuPc-CuPc forces. However, this is in contrast to a previous report that proposes the 1st interfacial layer of CuPc to be flat-lying on perovskite.[66] This was based on DFT calculations that showed a higher binding energy for flat-lying CuPc compared to edge-on CuPc. These calculations were done for the model case of a single CuPc adsorbing on the surface. Consistent with that result, it was observed that a single CuPc molecule on the $MAPbI_3$ surface adopts a flat-lying orientation (Fig. 5.1), rather than an edge-on orientation. It should be noted that on $MAPbI_3$, this flat-lying orientation was only observed for a lone, isolated CuPc molecule. When many CuPc molecules are present, however, a much different picture results, in which intermolecular CuPc forces dominate over molecule-substrate interactions. This explains the

discrepancy between the reported calculation and the experimental findings in this study. This distinction is important as it provides a more accurate picture of the CuPc-perovskite interface by showing the collective behavior of CuPc molecules at the atomic scale. This enables better simulation and prediction of perovskite-CuPc interfacial properties.

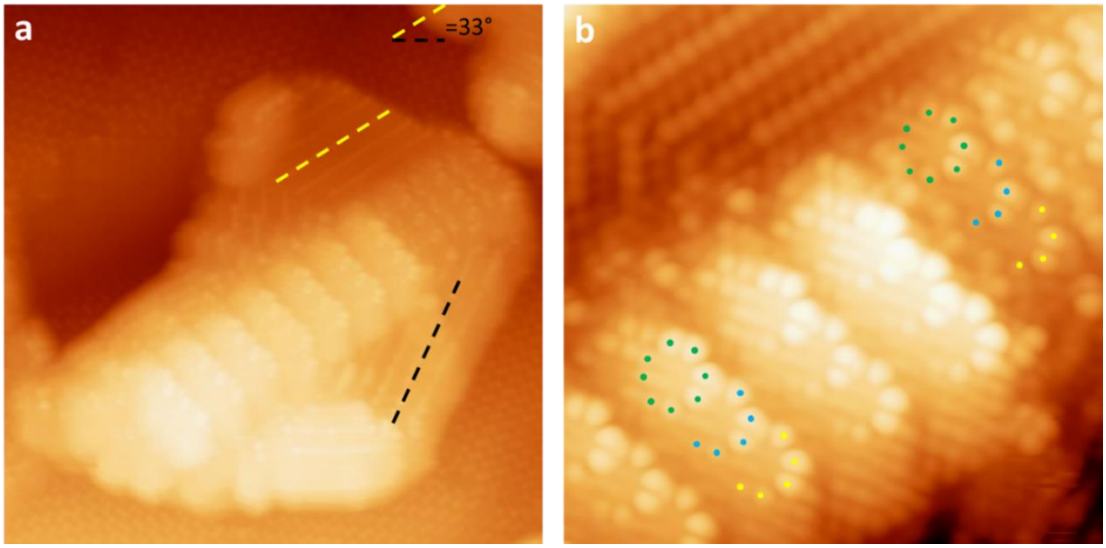

Figure 5.8 Unique CuPc stacking pattern at the SA layer junction. a) STM image showing unique CuPc stacking structure where two CuPc domains meet. Dashed black and yellow lines highlight the b-direction of each SA layer domain, which have an abnormal relative angle of 33°. b) Zoomed-in image of the CuPc stacking pattern. Different colored circles (lower left) indicate the position of the outer orbitals of different CuPc molecules. Not all eight outer orbitals are visible, indicating intermolecular overlap between adjacent molecules. Colored circles (upper right) show similar stacking in a lower layer of CuPc. Image Size: a) 27.7 × 27.7 nm^2, b) 10.1 × 10.1 nm^2. Imaging parameters: a,b) V = -2.5 V, I = 100 pA.

Although the 2nd layer predominantly forms the same structure as the 1st layer, additional behavior was observed. Just as on $MAPbI_3$, it was found that face-on adsorption is possible for a single, isolated CuPc molecule on the CuPc SA layer. More intriguingly, there was one observation of an alternate, ordered stacking pattern of CuPc on top of a CuPc SA layer. In Figure 5.8a, there are multiple rows of CuPc for which only a few of their outer orbitals are well resolved. The pattern is particularly notable because there is clearly resolved overlap of adjacent CuPc molecules, which is in contrast to the known stacking patterns of α-CuPc and β-CuPc. One possible cause for the formation of the unique stacking structure could be the discontinuous nature of the underlying CuPc SA layer. In Figure 5.8a, there are actually two different CuPc SA layers that have grown into each other at an angle of 33°, much smaller than the typical 121° bending angle. This makes

the normal bending pattern not possible, and likely results in a unique boundary topography between the two, which may cause the unique 2nd layer growth on top. This is important as it shows the viability of stacking schemes that involve intermolecular overlap, and thus a non-zero, non-normal tilt angle relative to the substrate. In the next section, an alternate CuPc stacking pattern for the SA layer potentially involving molecular overlap is considered.

5.7 Alternate CuPc stacking patterns

So far the discussion has centered around CuPc SA layers featuring the repeating pattern of two rows of protrusions, one darker and one brighter. However, it is worth noting that another, less common three-protrusion chevron-shaped motif was observed (dashed black lines, Fig. 5.9). The dimensions are roughly the same as for the two-row pattern discussed in previous sections, with values of 1.17 nm (a-direction) and 4.7 Å (b-direction). However, a stacking angle of 73° is observed (dashed blue line, Fig. 5.9a), in contrast to the 61° stacking of the two-row pattern domains.

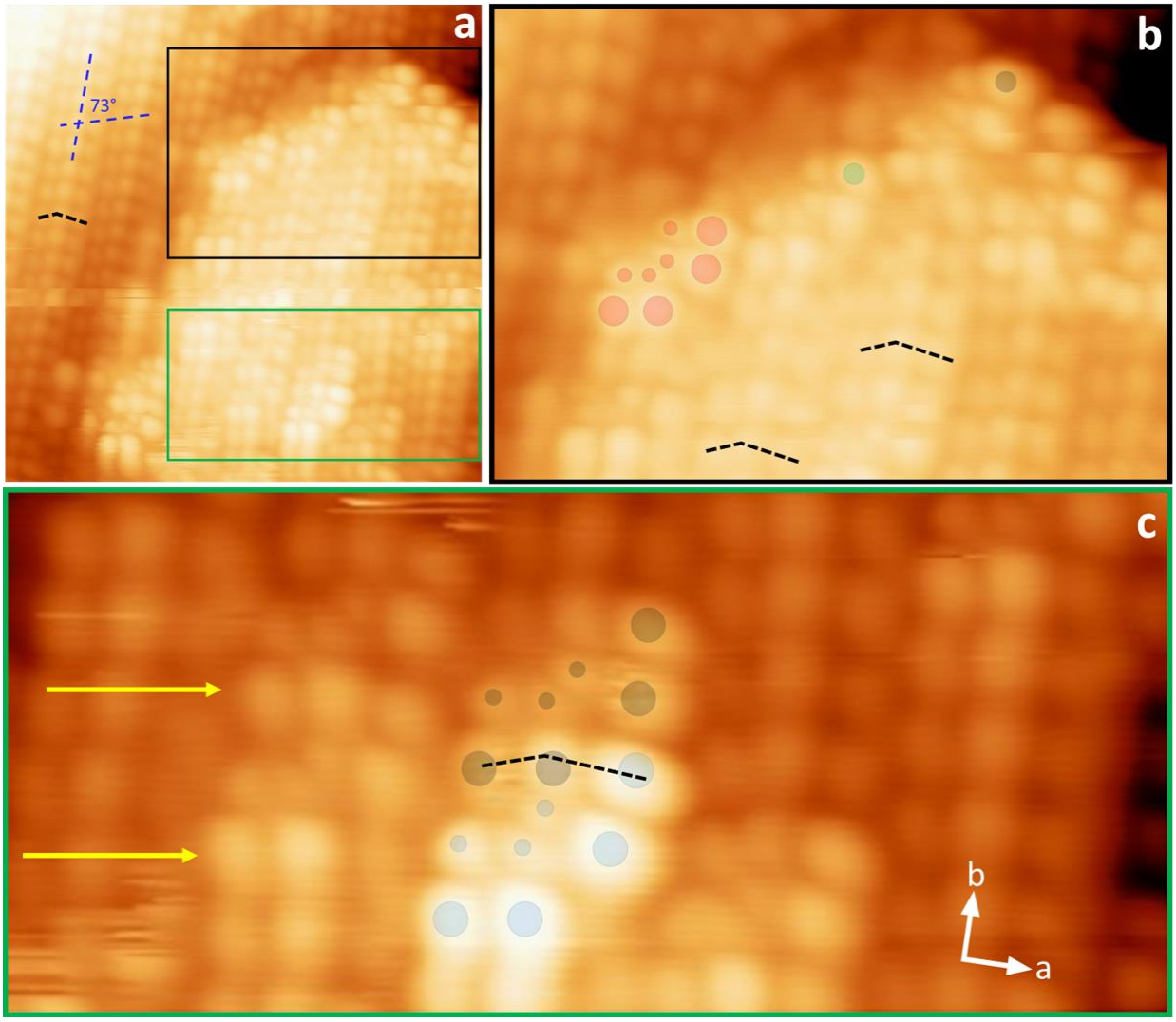

Figure 5.9 Three-protrusion motif and tilted CuPc molecules. a) STM image showing a CuPc SA layer exhibiting a three protrusion repeating pattern (dashed black line). Dashed blue lines denote stacking angle. b) Zoom-in on orbital pattern exhibited by an individual CuPc molecule at the SA layer edge (red circles). Green and black circles denote the upper-right most orbital for other CuPc molecules. Not all eight outer orbitals are visible, suggesting a tilted geometry with respect to $MAPbI_3$. c) Zoom-in on the middle of a CuPc SA layer where individual CuPc molecules are partially distinguishable. Blue and black circles denote orbitals from two different CuPc molecules. The black dashed line shows the chevron pattern created by orbitals from two different molecules. Arrows indicate similar CuPc molecules in the adjacent row. Image Size: a) 9.0 × 9.0 nm^2, b) 6.0 × 4.7 nm^2, c) 5.9 × 2.6 nm^2. Imaging parameters: a-c) V = -2.5 V, I = 100 pA.

An interesting phenomenon was observed in this domain where individual CuPc molecules are partially visible at the SA layer surface. Strikingly, the orbital lobes of the partially distinguishable CuPc molecules line up well with the macroscopic row structure of the SA layer. In Figure 5.9b, individual CuPc molecules are seen at the edge of the CuPc layer. Only four outer orbital lobes and four inner orbital lobes are clearly resolved (red circles), while the other lobes are blurred and have an apparent height comparable to the lower SA layer. This suggests that these molecules at the edge are tilted with respect to the substrate in both the a and b directions. SA layers are typically formed by molecules aligned at the same orientation, therefore it may be possible that CuPc molecules throughout the SA layer have a similar tilt as seen for the molecules on the edge.

Partially resolved individual CuPc molecules were resolved not just at the edge, but also in the middle of the SA layer (blue and grey circles, Fig. 5.9c). Interestingly, these molecules show how the repeating, 3-protrusion chevron pattern could actually be composed of orbitals from two different overlapping CuPc molecules (dashed black line, Fig. 5.9c). It is important to note that for these molecules, 3 of the teardrop-shaped inner orbital lobes are resolved, whereas this is not normally the case for a regular chevron pattern. This suggests that the exact tilt and overlap of these individually distinguishable molecules may differ slightly from the CuPc molecules producing the 3-protrusion chevron pattern. The CuPc molecules highlighted in Figure 5.9c by blue and gray circles are offset from each other by ½ molecule in the b-direction. This allows the inner orbital lobes to be resolved. These lobes are not normally seen for the chevron pattern; thus it is proposed that a smaller ¼ molecule offset in the b-direction may produce the repeating chevron pattern. The fact that the molecule appears to be tilted in both the b- and a-directions suggests that there is intermolecular overlap in the a-direction as well. However, overlap in both directions would require a complex intercalation of the CuPc molecules that is not understood at this time.

It should also be noted that evidence was observed on a chevron pattern domain that potentially supports a stacking model without intermolecular overlap in either the a- or b-directions. In figure 5.10 there are a number of defects in the SA layer, manifested as darker protrusions (yellow arrow). These do not occur as a single darker protrusion, but rather an entire 3-protrusion chevron pattern appears darker. Assuming the defect is due to geometric position of a single CuPc molecule, this would mean a chevron pattern is actually only composed of orbitals from a single

CuPc molecule. If the chevron pattern was composed of orbital lobes from 2 different CuPc molecule, as proposed based on Figure 5.9, the origin of this depression pattern would have to at least be partially electronic in nature.

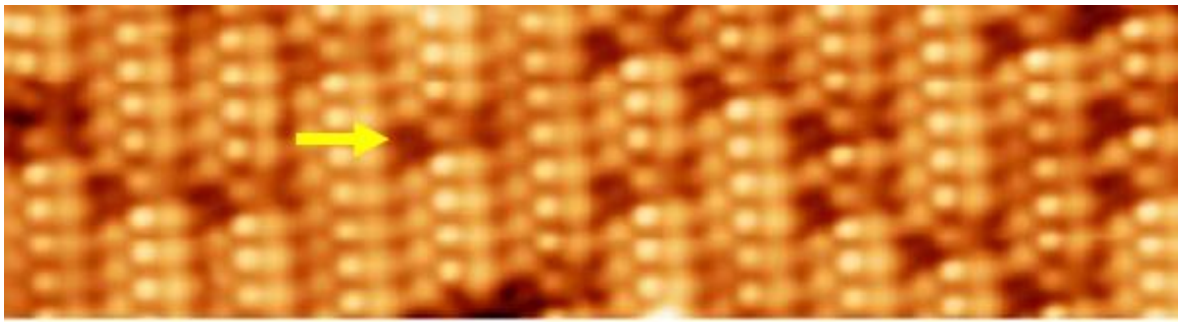

Figure 5.10 Defects in a chevron pattern domain. STM image of a chevron pattern domain with many defects. The defects appear as darker depressions and occur as a 3-depression chevron motif. Image Size: 12.4×3.3 nm^2. Imaging parameters: V = -2.64 V, I = 50 pA.

5.8 CuPc on non-$MAPbI_3$ domains

Understanding the behavior of CuPc on $MAPbI_3$ is essential for characterizing the interface in a device, but it does not provide the whole picture. The absorber layer in actual devices often does not have a perfectly stoichiometric ratio of elements, meaning that there are domains of non-perovskite material in the film. This can be incidental, due to side-effects of the fabrication process.[50] The non-stoichiometric ratio can also be by design, as there is evidence suggesting excess precursor material can improve performance.[53] The samples created here in UHV environment also have domains of non-perovskite material, and this section will focus on these domains.

Figure 5.11a shows an image of the $MAPbI_3$ surface that shows the expected perovskite surface reconstruction except for a small area in the bottom center of the image (blue square). This small area looks smooth when zoomed-out, but a closer look in Figure 5.11b reveals atomic corrugation with a hexagonal pattern and a lattice constant of 4.3 Å. The right side of Figure 5.11c shows how CuPc interacts with the unknown, non-$MAPbI_3$ surface. In stark contrast to the $MAPbI_3$ case, on the non-perovskite domains there are numerous CuPc molecules face-on adsorbed in a disordered fashion, and in close proximity to each other. A zoomed-in image shows the HOMO of an individual CuPc on this unknown material, as evidenced by the eight outer and eight inner orbital

lobes visible (Fig. 5.11d). The fact that CuPc molecules in close proximity are generally able to maintain a flat-lying orientation, rather than forming a SA layer, indicates that the molecule-substrate interaction with the non-perovskite material is stronger than with $MAPbI_3$ and can compete with SA layer formation. This behavior is particularly striking considering that there is an SA layer extremely close to the individual CuPc molecules. It is also worth noting that the $MAPbI_3$ surface is completely devoid of individual, face-on CuPc molecules. This difference in behavior has important implications for the perovskite-HTL interface in devices that have a non-stoichiometric perovskite film. Different adsorption geometries would have a dramatic effect on the orbital overlap between adjacent layers, which can be expected to significantly alter charge transfer at the absorber layer-HTL interface in devices.

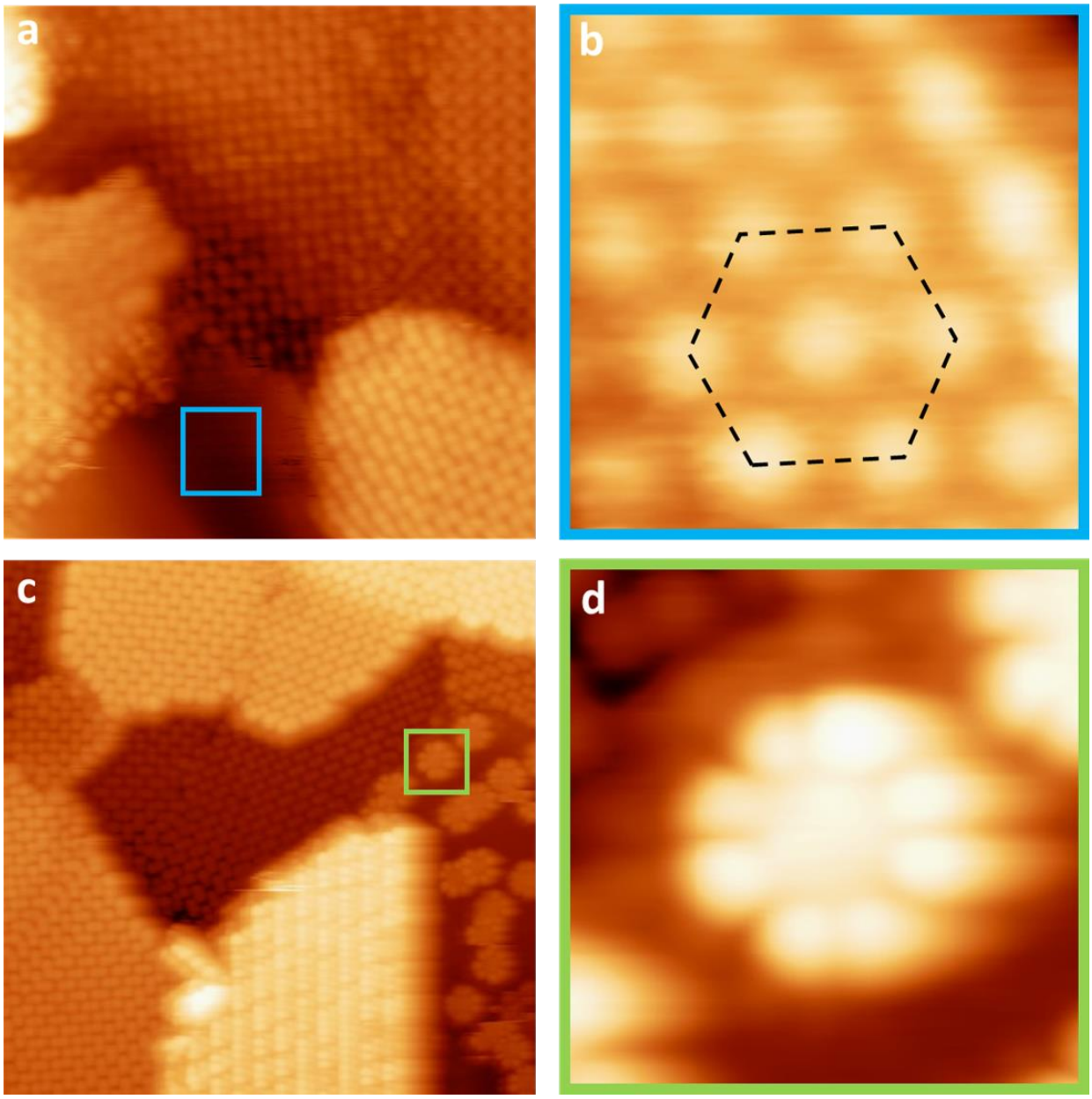

Figure 5.11 CuPc adsorption on non-$MAPbI_3$ surface. a) Overview image showing an $MAPbI_3$ film before CuPc deposition. The bottom of the image features a smooth, featureless area. b) Zoom-in of the blue box area from Fig. (a) revealing atomic corrugation with a hexagonal pattern and a lattice constant of approximately 4.3 Å. c) A similar area featuring $MAPbI_3$ and non-$MAPbI_3$ domains after CuPc deposition. Very different behavior of CuPc molecules is seen depending on the domain where it is adsorbed (i.e perovskite or not). d) Zoom-in of face-on adsorbed CuPc on the non-MAPbI3 domain. Image Sizes: a) 17.6 × 17.6 nm^2 b) 1.6 × 1.6 nm^2; c) 26.4 × 26.4 nm^2; d) 3.3 × 3.3 nm^2. Imaging parameters: a,c-d) V = -2.5 V, I = 100 pA; b) V = -2.2 V, I = 100 pA.

5.9 Evaluation of non-$MAPbI_3$ domain identity

To provide a more detailed picture, it is important to understand the identity of this unknown domain. Five candidate materials are considered here: PbI_2, MAI, an iodine adlayer, Pb, and bare Au(111). To examine the possibilities of PbI_2 and MAI, precursor-only depositions were performed on cleaned Au(111) using the same deposition temperatures and times as for the co-deposition trials.

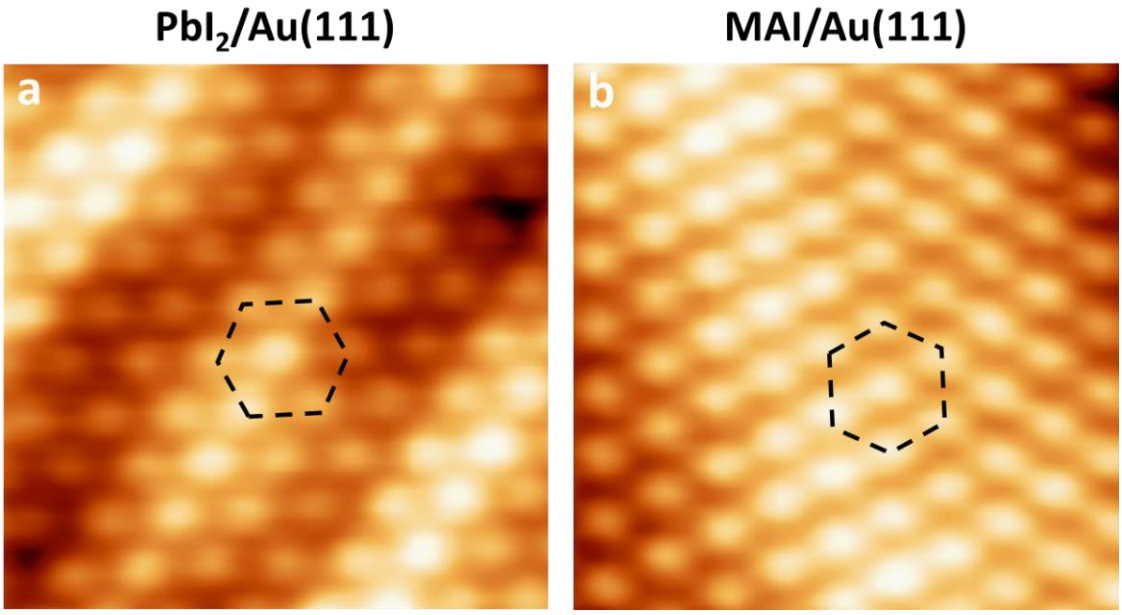

Figure 5.12 Non-$MAPbI_3$ domain candidate material characterization. a) PbI_2 deposited on Au(111). b) MAI deposited on Au(111). In both figures, the hexagonal lattice is denoted by dashed black lines. Image Sizes: a) 3.5 × 3.5 nm^2 b) 3.6 × 3.6 nm^2. Imaging parameters: a-b) V = -2.7 V, I = 300 pA.

First, only PbI_2 was deposited, resulting in a hexagonal atomic pattern (Fig. 5.12a). The average nearest neighbor distance between atoms is between 4.4 Å, with some variation depending on the direction in which the line profile is taken. This average value is comparable with literature values for PbI_2 films ranging from 4.5-4.6 Å.[152, 237-239] Importantly, this lattice constant is consistent with that of the hexagonal pattern seen on the non-$MAPbI_3$ domain. Therefore, PbI_2 is considered to be a viable candidate for the non-perovskite domain.

Next, an MAI-only deposition was performed on cleaned Au(111). Although a tetragonal unit cell is expected from MAI,[240] the resultant film exhibits a hexagonal pattern with a lattice constant of 4.6Å (Fig. 5.12b). This is slightly smaller than the hexagonal lattice constant of 4.9Å

reported by She et al.,[152] who proposed that this hexagonal pattern is formed by iodine atoms leftover after MAI dissociates upon reacting with the metal Au(111) surface. This explanation is also feasible for the result obtained in this study. Based on this interpretation, MAI is eliminated as a candidate for the non-$MAPbI_3$ domains observed. However, the possibility of an iodine network formed after MAI dissociation must now be considered.

Evidence supporting the hypothesis of an iodine layer was found in STM images of a non-optimized $MAPbI_3$ deposition trial, in which only approximately 30% of the sample surface was perovskite. In Figure 5.13a, a region of this sample with both $MAPbI_3$ and non-perovskite domains is shown. Even in this overview image, some faint long-range corrugation is evident in the non-$MAPbI_3$ domain. Smaller area images of such a non-perovskite domain reveal a hexagonal superstructure with a spacing of 2.61 nm (Fig. 5.13b) and a hexagonal atomic pattern with a lattice constant of 4.3 Å (Fig. 5.13c). The superstructure is found to be rotated by 9° relative to the atomic hexagonal lattice (black and yellow lines, Fig. 5.13b).

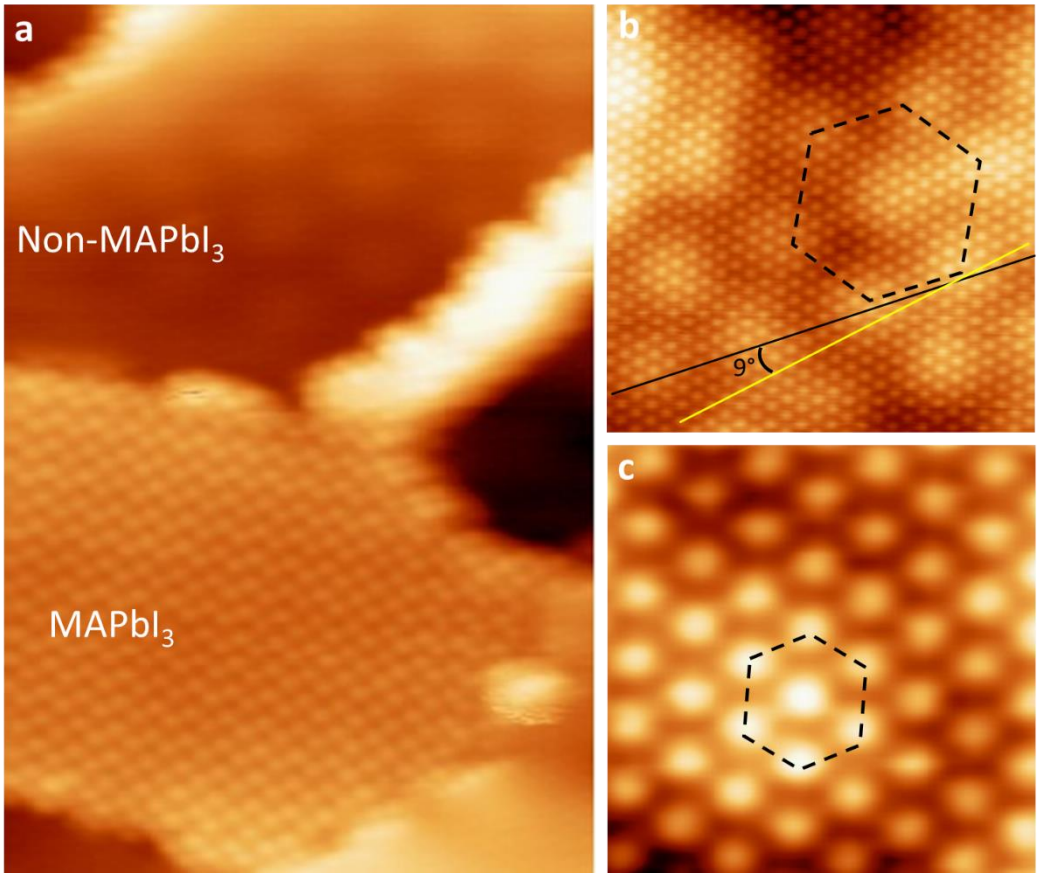

Figure 5.13 Hexagonal superstructure on unoptimized $MAPbI_3$ co-deposition. a) Overview image of unoptimized $MAPbI_3$ showing $MAPbI_3$ and non-$MAPbI_3$ domains. b) Image on non-$MAPbI_3$ domain showing a hexagonal atomic lattice as well as a hexagonal superstructure. The black and yellow lines follow the periodicity of the superstructure and atomic lattice, respectively, showing the relative rotation of the two features. c) Zoom-in of atomic lattice from (b). Dashed black lines show the hexagonal superstructure and atomic lattice in (b) and (c). Image Sizes: a) 13.4 × 19.7 nm^2; b) 10.3 × 10.3 nm^2; c) 2.7 × 2.7 nm^2. Imaging Parameters: a-c) V = -2.7 V, I = 300 pA.

Notably, there are reports in the literature of hexagonal superstructures forming when an iodine adlayer is formed on Au(111).[241-243] The reported superlattice constants (19-22 Å) are somewhat smaller than that measured in this work, but the relative angle of rotation between the atomic and superstructure lattices observed in these studies (7-10°) matches extremely well. Literature values for the nearest neighbor spacing of iodine adlayers on Au(111) vary depending on coverage. Lower coverages can yield a spacing of 5Å, the expected value for an iodine adlayer with a $(\sqrt{3} \times \sqrt{3})R30°$ symmetry with respect to the Au(111) substrate.[241-243] With higher coverages, compression of nearest neighbor spacing can occur, and I-I distances of 4.3-4.5Å have been

reported,[242, 243] which is more consistent with the lattice constant of 4.3 Å measured in this study. Polyiodide chains and multilayer iodine can be ruled out as they exhibit different patterns than what is seen here.[243] Finally, a survey XPS scan taken before STM imaging showed excess iodine, further supporting the hypothesis of the non-$MAPbI_3$ domain being an iodine adlayer. Based on these results and comparison with existing literature, it is determined that an iodine adlayer is a viable candidate for the identity of the non-$MAPbI_3$ domain observed in the CuPc/$MAPbI_3$/Au(111) samples.

Next, Pb is evaluated as a possible candidate for the non-$MAPbI_3$ domain. Comparison with literature shows that a Pb monolayer on Au(111) exhibits a hexagonal pattern with the a nearest neighbor distance of 3.5Å,[244] which is somewhat smaller than the periodicity measured here on the unknown hexagonal structure. A hexagonal moiré pattern was also reported for Pb on Au(111), but this pattern is rotated 26.5° relative to the atomic lattice of Pb, which is much larger than the relative angle of 9° measured between the atomic lattice and super lattice on the non-$MAPbI_3$ domains. Due to these inconsistencies, Pb is deemed to not be a suitable candidate for the identity of the non-perovskite domain.

Finally, bare Au(111) can be quickly eliminated as a possibility for the non-$MAPbI_3$ domain. The spacing between neighboring atoms in the non-$MAPbI_3$ domain is 4.3 Å, while the nearest neighbor distance in the Au(111) surface measured by STM is known to be 2.8 Å.[245] Additionally, based on literature and in-lab reproduction, CuPc appears as a cross shape on Au(111), rather than in the 16-lobed HOMO state seen on the non-$MAPbI_3$ domains.

It should also be noted that a number of defects were observed in the unknown hexagonal pattern. Representative images of defects found on various sample types are shown in Figure 5.14. Two different types of single depression defects were found in the hexagonal pattern from the MAI/Au(111) deposition trial. In one type the depression is surrounded by a perimeter of higher DOS (Fig. 5.14a), whereas in the other type, no modulation of the surrounding area DOS is seen (Fig. 5.14b). Interestingly, these two cases were imaged at the exact same imaging parameters, suggesting these are distinct defect types, rather than just an electronic effect due to different gap voltage. On the non-optimized 30% $MAPbI_3$ sample, a triple bright protrusion defect can occur (Fig. 5.14c) as well as triple and single dark depression defects (Fig. 5.14d, top and bottom, respectively).

Lastly, on the optimized $MAPbI_3$ sample on which the CuPc depositions were performed, two types of triple depression defects were imaged. In Figure 5.14e the depressions are separated from the other depressions by a single atom in each direction, while in Figure 5.14f the three depressions are nearest neighbors. A survey of the literature did not yield any STM reports on defects that occur in PbI_2 or in an iodine adlayer with which to compare the images obtained here. Notably, a separated triple depression defect similar to Figure 5.14e was reported for Gd-substituted Bi_2Te_3 and attributed to sub-surface layer substitutional defects.[246] At this time, the defect patterns seen in this study do not enable any strong conclusions regarding the identity of the non-$MAPbI_3$ domain. However, they may provide important clues, especially in conjunction with future theoretical studies.

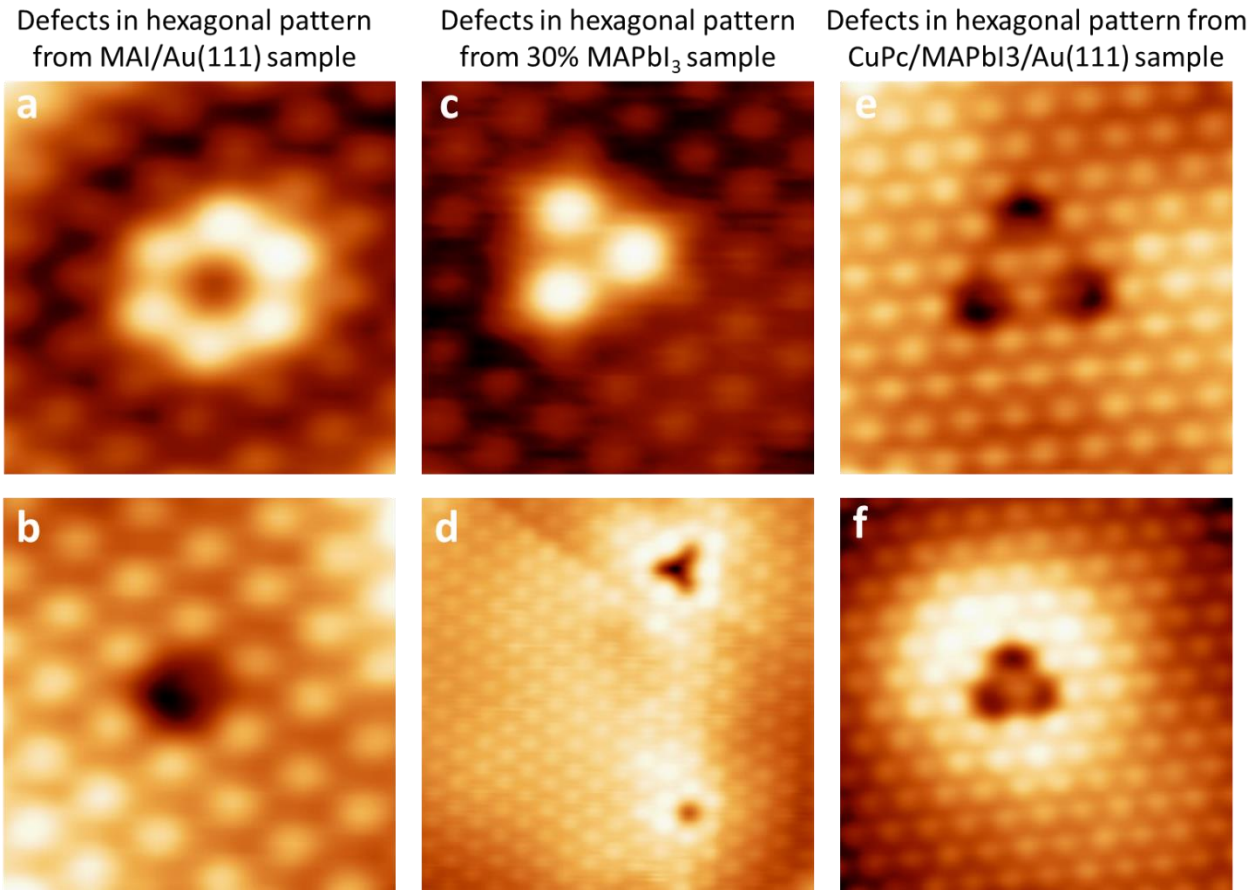

Figure 5.14 Defects in non-$MAPbI_3$ domains. a-b) Single depression defects in the hexagonal pattern on an MAI/Au(111) sample. Image (a) shows increased DOS around depression, whereas (b) does not. c-d) Defects in the hexagonal pattern on an approximately 30% $MAPbI_3$ sample. Image (c) shows a cluster of three bright protrusions. Image (d) shows both triple depression (top) and single depression (bottom) defect types. e-f) Separated (e) and clustered (f) triple depression defects in the hexagonal pattern on a CuPc/$MAPbI_3$/Au(111) sample. Image Sizes: a-c) 2.4 × 2.4 nm^2; d) 6.3 × 6.3 nm^2; e) 3.3 × 3.3 nm^2; f) 4.2 × 4.2 nm^2. Imaging parameters: a-d) V = -2.7 V, I = 300 pA; e-f) V = -2.5 V, I = 155 pA.

5.10 CuPc on $MAPbBr_3$

To check whether the behavior of CuPc is dependent on the identity of the halide in the perovskite, CuPc was also deposited onto bromine-based perovskite. $MAPbBr_3$ thin films were prepared using a similar protocol as for $MAPbI_3$. $PbBr_2$ and MABr were co-evaporated at 533K and 376K, respectively, for 4 minutes onto a cooled Au(111) substrate. CuPc deposition was performed by the same protocol described in Section 5.2. Similar results were obtained as on $MAPbI_3$, with the CuPc forming a zig-zag SA layer exhibiting a repeating pattern of alternating

bright and dark rows of protrusions (Fig. 5.15a). These SA layers exhibited 121° bends and periodicity along a 60° stacking angle, consistent with the SA layers formed on $MAPbI_3$. Thus, the formation of such a CuPc SA layer does not seem to be sensitive to the halide used in the perovskite film. Consequently, the OHP-CuPc interface structure shown in this work is representative for a wider variety of perovskite-based solar cell devices.

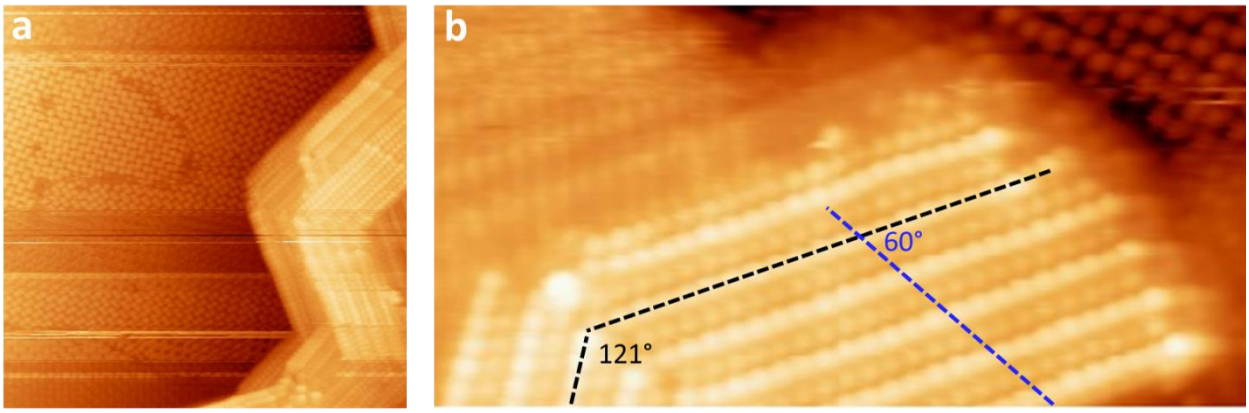

Figure 5.15 CuPc SA layer on $MAPbBr_3$. a) Overview STM image showing a CuPc SA layer on $MAPbBr_3$. Note there is a shadowing effect on the CuPc SA layer caused by a multi-tip. b) Close-up image of the CuPc SA layer on $MAPbBr_3$. The black and blue dashed lines show the bend angle and stacking angle of the CuPc SA layer, respectively. Both are consistent with the CuPc SA layer on $MAPbI_3$. Image Size: a) 30.0 × 30.0 nm^2, b) 16.5 × 7.7 nm^2. Imaging parameters: a) V = 5.3 V, I = 400 pA; b) V = 6.7 V, I = 600 pA.

5.11 Summary

The results of this chapter show that the CuPc HTL forms a SA layer on top of the light absorber layer $MAPbX_3$ (X=I, Br). It was found there is no unique, face-on adsorption of the 1st interfacial layer of CuPc with perovskite, contrary to a previous report.[66] After a thorough analysis of the collected data, there are two main hypotheses regarding the stacking structure of the CuPc SA layer observed on $MAPbI_3$. The first hypothesis is that the SA layer is a modified version of α-CuPc. Support for this hypothesis comes from the observed periodicity at a 61° stacking angle and from the 11.4Å spacing between the rows of bright protrusions (i.e. along the a-axis), which match reasonably well with literature values for α-CuPc. The tendency for defects in the SA layer to occur in pairs along a stacking angle consistent with α-CuPc also support this proposal. However, there is some mismatch with literature for the b-axis periodicity. Additionally, the SA layer height

measured here suggests a tilted adsorption geometry, which would require a departure from the reported α-CuPc stacking schemes.

An additional parameter to consider is that the CuPc molecule could adsorb such that either one or two isoindole groups are contacting the underlying $MAPbI_3$. A study by Gardener et al. observed CuPc SA layer formation on silicon and concluded that double isoindole group adsorption was occurring because the rows were all the same apparent height.[158] The alternating bright and dark rows seen in this chapter suggest a situation closer to single isoindole group adsorption is occurring. However, the relative width of the dark and bright rows doesn't match what would be expected from single isoindole adsorption, so a definitive assignment is still premature. Future calculations from a theoretical collaborator will hopefully shed more light on this question.

The second hypothesis involves a stacking scheme where there is intermolecular overlap in the SA layer in both the a and b axes. This is supported by STM images showing partially resolved individual CuPc molecules in an SA layer with a repeating 3-protrusion chevron pattern. These partially resolved CuPc molecules line up well with the macroscopic rows of the SA layer and can form the chevron pattern via orbitals from two different molecules, necessitating overlap of neighboring molecules. Additionally, the unique stacking pattern seen in Figure 5.8a shows that an overlapped stacking pattern is possible.

It should be stressed that the chevron pattern was a rare observation, and it is not clear yet if this pattern constitutes a distinct polymorph from the usual bright-dark alternating row pattern. It has been shown that more than one polymorph can exist in the same sample preparation for TMPcs,[247] therefore this possibility must be considered. The difference in observed stacking angle between the two-row pattern (61°) and the chevron pattern (73°) supports the idea that these are distinct polymorphs. However, despite the difference in appearance, the periodicity along both the a and b axes is similar for both the bright-dark two row pattern and the chevron pattern domains, suggesting they may actually be the same polymorph. The topography measured via STM can change dramatically depending on the shape and composition of the tip apex. Although a well-resolved image involving a change in tip-shape showing direct correlation of the two-row and chevron patterns was not obtained, this remains a possible explanation for the two domains being the same polymorph even though they have different repeating motifs.

Irrespective of the stacking scheme of the CuPc molecules, observations suggest a relatively weak interaction between the CuPc SA layer and the underlying perovskite. The CuPc SA layer was found to exist at many different angles relative to the high symmetry directions of $MAPbI_3$, indicating no preferred relative orientation and thus a weak coupling of the SA layer and $MAPbI_3$. CuPc SA layers were observed to pass over $MAPbI_3$ grain boundaries of the perovskite without being perturbed, further indicating weak interaction between the two layers. This idea is also supported by the rarity of individual face-on adsorbed CuPc molecules and by the mobility of such molecules. A similar CuPc SA layer has been observed forming as the 2nd layer of CuPc after an initial 1st layer of face-on CuPc was formed on Bi(111), suggesting that this striped SA layer forms when the CuPc is sufficiently decoupled from a substrate.[160] This corroborates the idea that the interaction between $MAPbI_3$ and CuPc is relatively weak.

Conversely, CuPc exhibited a much different behavior on non-$MAPbI_3$ domains present in the film. On these domains, CuPc exhibited a comparatively stronger interaction with the substrate, as evidenced by face-on adsorption geometry and the fact that multiple CuPc molecules could exist in close proximity without forming an SA layer. CuPc molecules on the non-$MAPbI_3$ domain could also stay in their disordered arrangement without attaching to nearby a CuPc SA layer.

Multiple candidates for the identity of the non-$MAPbI_3$ domain were evaluated and compared with the observed hexagonal atomic packing and nearest neighbor spacing of 4.3 Å. A PbI_2 only deposition yielded a hexagonal atomic lattice with 4.4Å. This is consistent with the non-$MAPbI_3$ domain and with literature values for PbI_2, thus PbI_2 is considered a viable candidate. An MAI only deposition resulted in a hexagonal pattern with a lattice constant of 4.6Å. The hexagonal pattern is not consistent with literature for MAI, thus it was eliminated as a candidate. The hexagonal pattern could potentially be from dissociated MAI creating an iodine adlayer. Supporting this hypothesis, non-$MAPbI_3$ domains on $MAPbI_3$ deposition samples showed a hexagonal superlattice rotated 9° from the hexagonal atomic lattice, consistent with literature for an iodine adlayer on Au(111). Thus an iodine adlayer is also considered a viable candidate for the non-$MAPbI_3$ domain. Pb was eliminated as a possibility since the reported relative rotation angle of the superlattice and atomic lattice (26°) is much larger than that measured on the non-$MAPbI_3$ domain (9°). Au(111) was eliminated since its nearest neighbor spacing of 2.8Å is smaller than

that of the non-$MAPbI_3$ domain. In summary, both PbI_2 and an iodine adlayer were determined to be possible candidates for the non-$MAPbI_3$ domain.

The strikingly different behavior of the CuPc on the $MAPbI_3$ and non-$MAPbI_3$ domains has important consequences for perovskite solar cells with a non-stoichiometric perovskite film. This change in adsorption geometry can be expected to alter interfacial properties,[129] including energy level alignment and charge transfer between the absorber layer and the CuPc HTM. The different CuPc orientations also lead to a less ordered HTM layer near the interface, which may negatively affect device performance. This study shows that the adsorption orientation and uniformity of the HTM (CuPc) at the molecular level depends strongly on the uniformity of the active absorber layer (i.e., $MAPbI_3$).

Currently, there is not enough evidence to conclusively determine whether PbI_2 or an iodine adlayer is the more appropriate assignment for the non-$MAPbI_3$ domain. Defects observed in the non-perovskite domain may provide clues for clarifying the identity of this domain with the help of theoretical support. In either case, there is merit in theoretical characterization of PbI_2-CuPc and iodine adlayer-CuPc interfacial properties, as both PbI_2 and I_2 can exist in non-ideal perovskite films. Such theoretical investigations are planned and will provide further insight into the complex interface observed here and clarify the implications for charge transfer and energy level alignment at the device interface.

Chapter 6: Atomic structure of the $CsPbBr_3$ surface[248]

6.1 Introduction

The previous chapters have focused on surfaces and interfaces that involve perovskites with the methylammonium cation in the A site. The methylammonium lead halide perovskites have shown high PCE in photovoltaic devices, but the organic nature of the methylammonium cation has contributed to material instability issues that hinder commercialization.[131, 132, 249] Incorporation of fractional amounts of cesium into the A site has improved phase stability of mixed halide perovskites[28] and has also led to higher overall device stability.[46] Understanding the surface structure of mixed cation perovskites will enable better modeling of device-relevant interfaces and their effect on key performance indicators. As an initial step toward this, it is prudent to first understand the surface of the simpler systems, $MAPbBr_3$ and $CsPbBr_3$, before attempting to understand the composite system, $MA_xCs_{1-x}PbBr_3$.

This chapter details our work on exploring the $CsPbBr_3$ surface with STM and PES techniques. The $CsPbBr_3$ surface is of high interest on its own, as this material has shown promise in a wide-range of applications. $CsPbBr_3$-based solar cells have gained attention thanks to excellent stability and improved performance.[47, 250, 251] $CsPbBr_3$ has also shown strong promise being used to create LEDs,[2-4] and perovskite interfaces in such LEDs have been shown to be crucial to device performance. Additionally, applications in nanowire-based laser cavities[5, 6] and in x-ray and γ-ray detectors[252] make $CsPbBr_3$ a material of general fundamental interest to a broad spectrum of fields. Understanding the surface structure can lead to more accurate band structure calculations and enable more targeted interface engineering in devices.

Some progress on understanding the $CsPbBr_3$ surface was recently made in a scanning transmission electron microscopy (STEM) study showing that manipulating grain boundaries of nanocrystals could enable improved control of charge transfer between perovskite and neighboring layers in a device.[253] Although atomic resolution was achieved with this study, the high annular dark field (HAADF) imaging technique used measures a signal based on the atomic number of an

Adapted and reproduced with permission from Ref. 236. Copyright, 2020. American Chemical Society. The thesis author was a co-author and contributed to sample preparation, STM and XPS data acquisition and overall data interpretation and analysis. Figures provided by and modified with permission from Dr. Jeremy Hieulle.

element. This means that some Br^- at the surface are not observable due to the much stronger signal from the underlying Pb cations. Thus, an accurate picture of the $CsPbBr_3$ surface remains unreported. In this chapter, STM is used to determine the surface structure of $CsPbBr_3$ and reveals two different surface reconstructions, and the stability of $CsPbBr_3$ in UHV was monitored via XPS. DFT calculations were performed by a collaborating theory group at Jilin University.

6.2 Methods

The perovskite film was created via the co-deposition method in UHV onto a cleaned Au (111) substrate, using methods analogous to those described in earlier chapters. CsBr and $PbBr_2$ were co-evaporated at 670K and 515K, respectively, for 5 minutes onto an Au(111) substrate cooled to 132K. Low temperature STM was used to characterize the atomic-scale structures of the perovskite thin films at 4 K. The bias voltage was applied to the sample. XPS measurements were performed on half-cell architectures (Glass/FTO/TiO_2/$CsPbBr_3$) prepared according to the method described in reference 236.

6.3 Overview of the CsPbBr3 surface

$CsPbBr_3$ films produced using the methods described above were atomically flat and showed layer-by-layer growth (Fig. 6.1a). Connected grains, approximately 10nm in diameter, form a network that constitutes the uppermost layer of the film (light blue color, Fig. 6.1a). The inset in Figure 6.1a shows a step height of 5.3±0.3 Å, which will later be shown to be attributable to a single $CsPbBr_3$ layer. A smaller area image shows atomic resolution of the $CsPbBr_3$ top layer and underlying layer (orange and blue color, respectively, Fig. 6.1b). From this image, bright protrusions are distinguishable, which in a later section will be shown to be Br^- ions in the (010) surface of $CsPbBr_3$. These anions form pairs similar to the Br^- pairs found on the surface of $MAPbBr_3$. However, the Br^- pairs in $CsPbBr_3$ form two different arrangements, both of which are distinct from the surface reconstructions found on $MAPbBr_3$. Both the “stripe” and “armchair” domains are shown in Figure 6.1b, where their long-range pattern is highlighted in white. These two domains typically occur rotated by an angle of ±45° or ±90° relative to each other. A boundary between these two domains is also visible (Fig. 6.1b), nearby which multiple defects occur. In contrast, defects are rare within a single domain.

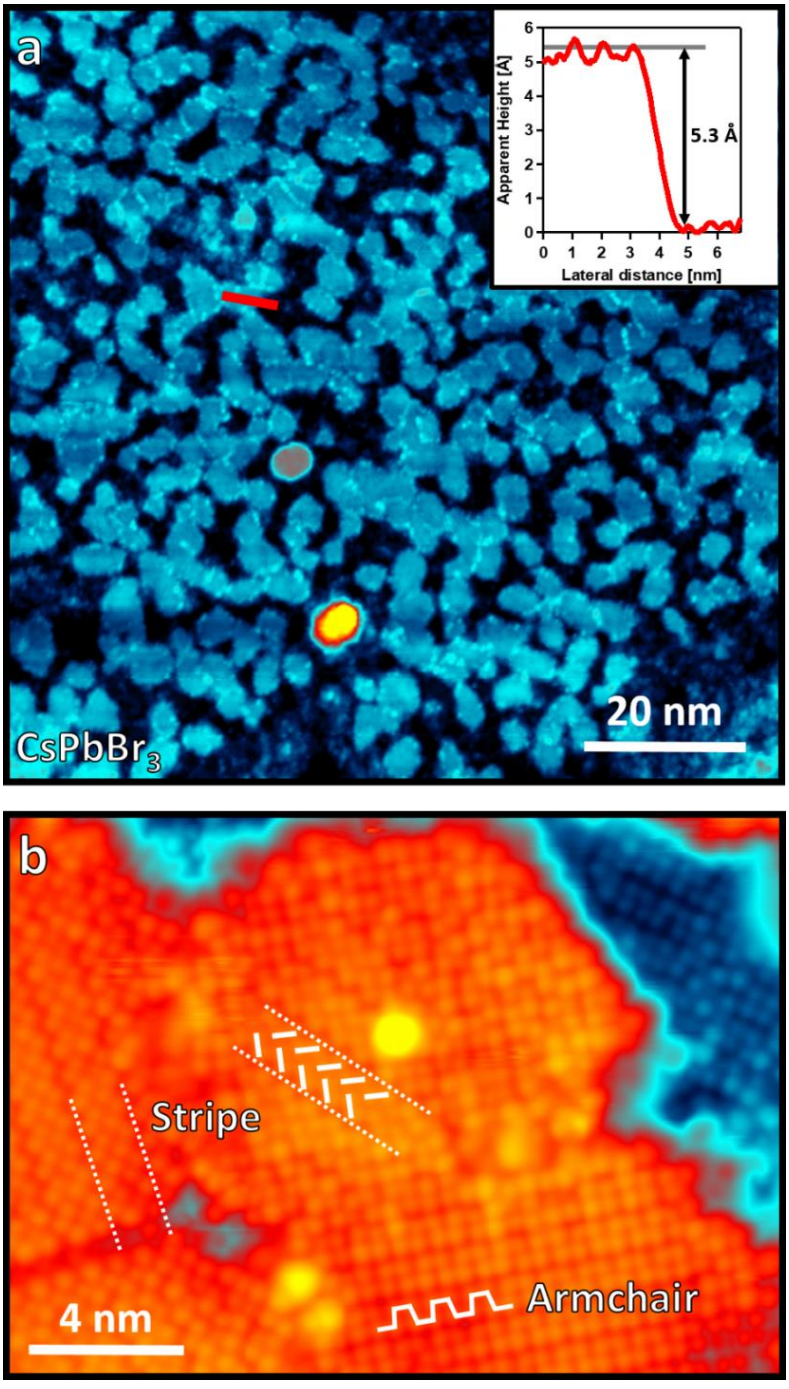

Figure 6.1 Overview of $CsPbBr_3$ surface. a) Large area STM image showing island growth of $CsPbBr_3$. Inset: Profile of the red line in (a), measuring the step height of the topmost layer. b) Atomic resolution image of the surface revealing two different "stripe" and "armchair" domains. White lines are guides for the eye showing the pattern of protrusions in each domain. Imaging parameters: (a) V = 3.0 V; I = 22 pA (b) V= 2.0 V; I = 30 pA. Image size: (a) 96 × 96 nm^2 (b) 20 × 14.5 nm^2.

Adapted and reproduced with permission from Ref. 236. Copyright, 2020. American Chemical Society. The thesis author was a co-author and contributed to sample preparation, STM and XPS data acquisition and overall data interpretation and analysis. Figures provided by and modified with permission from Dr. Jeremy Hieulle.

6.4 The "stripe" and "armchair" surface reconstructions

In this section, a closer look will be taken at the stripe and armchair domains. Combined with support from DFT calculations, models were proposed for these two atomic arrangements. It was found that the (010) surface, based on an orthorhombic $CsPbBr_3$ crystal structure in the *Pnma* space group,[254, 255] best matched the experimental STM images. From this calculation, it was possible to assign the bright protrusions in the STM images to be Br anions. Although Cs cations also are present in the (010) surface layer, they have not been resolved in experiment due to their density of states being lower than that of Br^-. A similar phenomenon was observed for $MAPbBr_3$, in which MA cations, despite being present in the (010) surface layer, were not visualized via STM except on very rare occasions. With the (010) surface layer assignment for $CsPbBr_3$, it is possible to characterize the stripe and armchair domains as two different surface reconstructions of this surface.

First, the stripe domain of the $CsPbBr_3$ surface is examined. From the STM images (Figs. 6.1b and 6.2a), it was seen that the protrusions in this domain are all of the same apparent height, and that each stripe comprises two columns of Br^- pairs. These two columns ran along the same macroscopic stripe direction (i.e. the A-axis of the unit cell denoted by the white rectangle in Fig 6.2a), but the Br^- pairs appeared rotated by approximately 76° with respect to the Br^- pairs in the other row in the same stripe (red and black lines, Fig. 6.2a). DFT calculations were consistent with this, showing pairing due to two different Br-Br distances, 5.2Å and 5.4Å, in the same row, and a relative angle of 77° with Br pairs in the adjacent row within the same stripe. Although well resolved in Figure 6.2a, the orientation of the Br^- pairing is not always obvious from STM imaging since the difference in nearest neighbor distances within a single row was near the instrumental resolution limit.

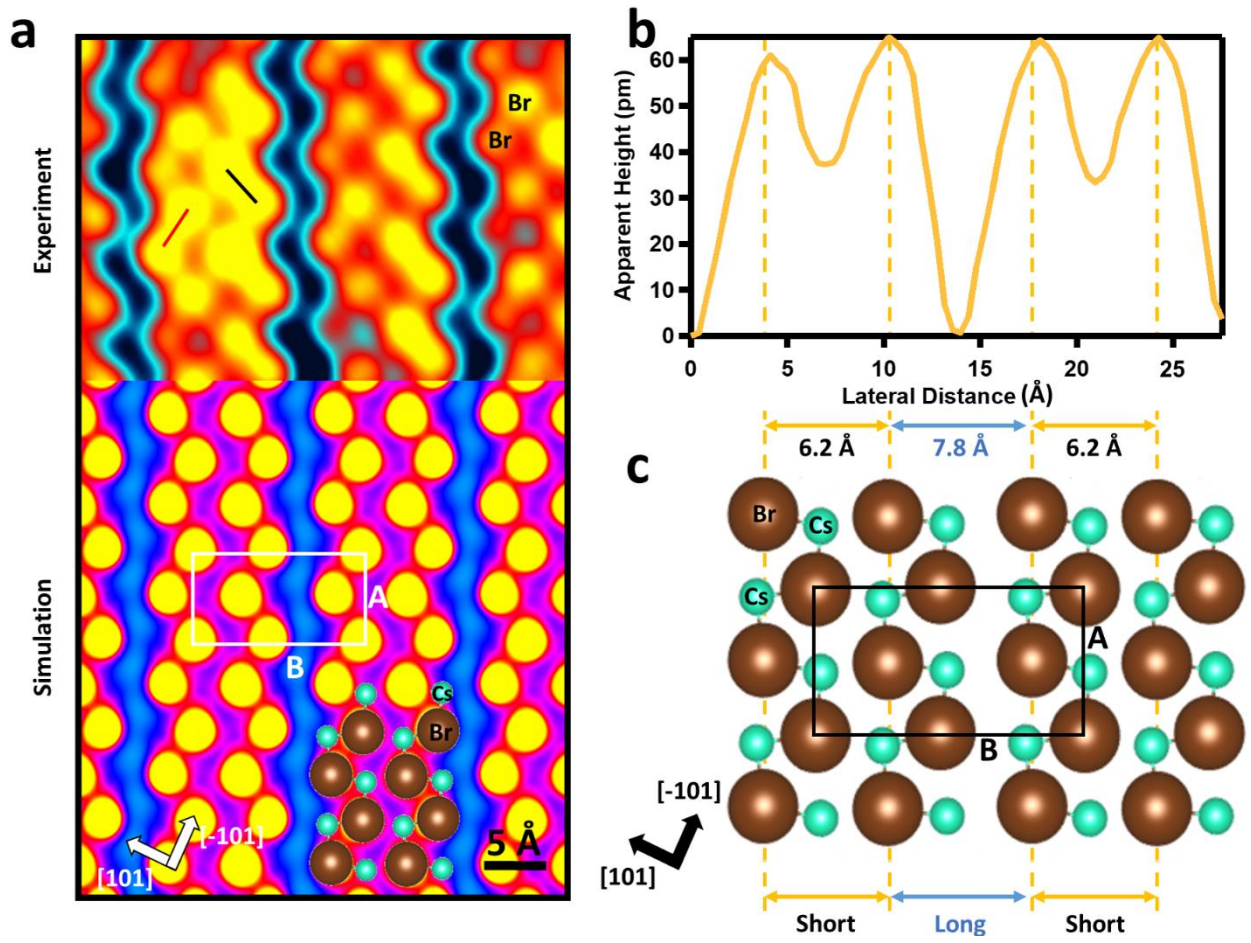

Figure 6.2 Stripe reconstruction of $CsPbBr_3$ surface. a) Experimental STM image of the "stripe" surface reconstruction (top) and corresponding simulated STM image determined by DFT (bottom). Each stripe consists of two rows of Br^- pairs with a relative orientation of 76° denoted by red and black lines. The white rectangle shows the unit cell. b) Line profile along the "B" axis of the unit cell. c) Surface structure of stripe reconstruction as calculated by DFT. The Br^- have been artificially enlarged in the model to help visualize the Br^- pairing. Alternating short and long distances between rows along the "B" axis result in the stripe motif. The unit cell is denoted by a black rectangle. Color code: Br^- (brown), Cs^+ (green). Imaging parameters: V = 2.3 V; I = 50 pA. Image size: 3.9 × 2.8 nm^2.

In the direction perpendicular to the stripe (B-axis of unit cell, Fig. 6.2a), there is an alternating short and long spacing between Br^- pairs (Fig. 6.2b-c). A distance of 6.2 Å was measured between Br^- pairs in the same stripe, and a longer 7.8 Å spacing was measured between Br^- pairs in neighboring stripes. The surface unit cell of this reconstruction (white box, Fig. 6.2a) is rectangular, with lattice parameters of A=7.3Å and B=14Å. Each unit cell contains $4Br^-$ and Cs^+ ions (black square, Fig. 6.2c) Calculations show that the Br^- pairs are caused Coulomb interaction

Adapted and reproduced with permission from Ref. 236. Copyright, 2020. American Chemical Society. The thesis author was a co-author and contributed to sample preparation, STM and XPS data acquisition and overall data interpretation and analysis. Figures provided by and modified with permission from Dr. Jeremy Hieulle.

between the Br^- and the two Cs^+ cations in close proximity. Calculations also confirm that the alternation in Br^- pairs' spacing is what causes the striped appearance of the surface reconstruction.

Next, a closer look is taken at the armchair domain. In contrast to the stripe domain where all protrusions had the same apparent height, STM images of the armchair domain show an alternating pattern with rows of Br^- pairs that have differing apparent heights (Fig 6.3a, top). These rows of brighter and darker Br^- pairs occur along the [-101] direction of $CsPbBr_3$, and are offset from each other along this direction. The other main feature of the armchair domain is the asymmetric spacing between the Br^- pairs along the [101] direction, which alternates between 5.6Å and 6.0Å (Figs. 6.3a-b). This difference in spacing, combined with the offset of the bright and dark rows, creates the armchair motif.

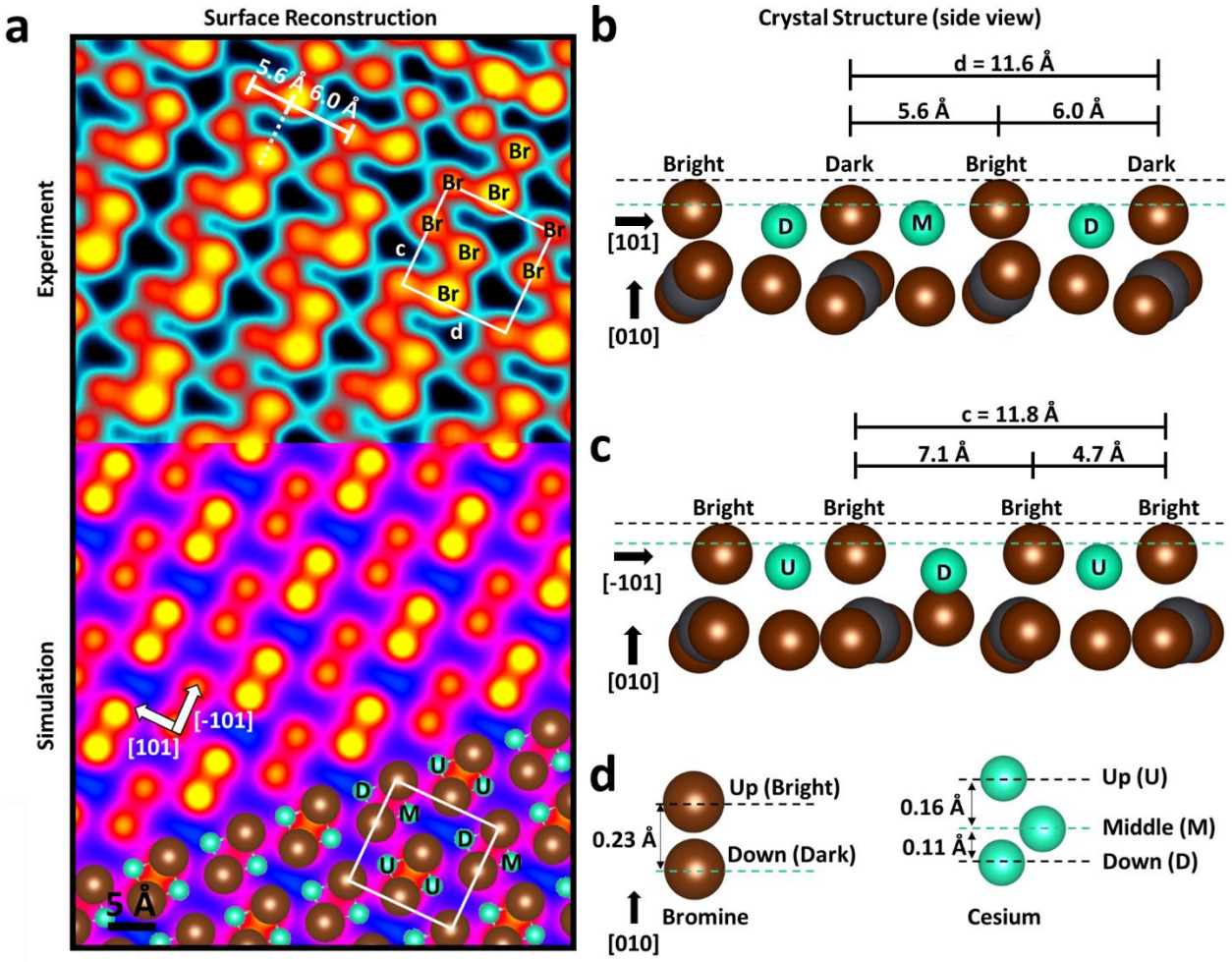

Figure 6.3 Armchair reconstruction of $CsPbBr_3$ surface. a) Experimental (top) and simulated (bottom) STM images of the armchair surface reconstruction of $CsPbBr_3$. The surface layer crystal structure is overlaid on the simulated image at the bottom, showing the arrangement of differently positioned Cs cations. The Br^- have been enlarged to emphasize Br^- pairing. The white square denotes the unit cell of the armchair reconstruction. b-c) Side view of the crystal structure for the armchair reconstruction of $CsPbBr_3$. Along the [101] direction (b), Br^- and Cs^+ ions occupy different vertical positions, while along the [-101] direction (c), only Cs^+ ions differ in height. d) Summary of the different vertical positions of Br^- and Cs^+ ions. Imaging parameters: V = 2.0 V; I = 100 pA. Image size: 5.2 × 4.2 nm^2.

DFT calculations that match well experimental images confirm the asymmetric spacing, and also reveal the bright and dark rows to be caused by a difference in the vertical position of the surface layer ions (Fig 6.3a-b). The calculated surface reconstruction shows Br anions in two different positions, with one position 23pm lower than the other (Figs. 6.3b and d), which is in agreement with the bright and dark protrusions seen in the experimental images (Fig. 6.3a). The

Adapted and reproduced with permission from Ref. 236. Copyright, 2020. American Chemical Society. The thesis author was a co-author and contributed to sample preparation, STM and XPS data acquisition and overall data interpretation and analysis. Figures provided by and modified with permission from Dr. Jeremy Hieulle.

Cs^+ ions show an even greater variety, occupying three different vertical positions, referred to as up (U), middle (M), and down (D) in Figures 6.3c-d. The relative arrangement of these differently positioned Cs cations is overlaid on the DFT simulated image at the bottom of Figure 6.3a, where the unit cell is also marked by a white rectangle. Bright Br^- pairs result when the two closest Cs^+ ions are both in the up position, while the darker Br^- pairs occur when the two nearest Cs^+ ions are in a middle and down position, respectively. The unit cell contains one bright Br^- pair with two Cs^+ ions in the up position and one dark Br^- pair with a Cs^+ in the middle position and another Cs^+ in the down position. The total number of ions in the armchair domain's surface unit cell (4 Br^- and 4 Cs^+) is the same as in the stripe domain's unit cell. At the top of Figure 6.3a, the unit cell is also marked (white rectangle) in the experimental STM image, from which lattice constants of c=11.8 Å and d=11.6 Å were obtained. In experimental images, the armchair reconstruction was less common than the stripe reconstruction, and this observation is supported by DFT calculations showing the stripe domain to be lower in energy than the less compact armchair domain. Finally, the calculated height of a single $CsPbBr_3$ layer is 5.69 Å, which matches well with the measured island height of 5.3±0.3 Å (Fig. 6.1a). Therefore, these islands are assigned to be a single layer of $CsPbBr_3$.

6.5 Comparison with $MAPbBr_3$ surface reconstructions

Now that the surface reconstructions of $CsPbBr_3$ have been clarified, it is useful to provide some comparison with its previously studied organic-inorganic counterpart, $MAPbBr_3$. In low temperature STM studies, both perovskites were found to have an orthorhombic crystal structure with the (010) plane exposed at the surface. Both $MAPbBr_3$ and $CsPbBr_3$ feature two surface reconstructions as well. $MAPbBr_3$ features the "zig-zag" and "paired" reconstructions, while $CsPbBr_3$ has "stripe" and "armchair" reconstructions. For $MAPBr_3$, the occurrence of two reconstructions is explained by two different relative orientations of the asymmetric, dipolar MA cations relative to each other and to the Br anions. These two different rotated positions of the MA^+ only affect the relative x-y positions of the Br anions, with their relative vertical positions remaining the same. Considering the origin of the two reconstructions lies in the dipolar nature of the MA cation, it would be logical to expect only one surface reconstruction for $CsPbBr_3$, given the spherically symmetric nature of the Cs cation. However, two different reconstructions have been unambiguously resolved in this study, with differences in the vertical positions of the Cs

cations resulting in differences in the vertical position of the Br anions. Such a difference in the apparent height of the halides was not seen for the reconstructions of either $MAPbBr_3$ or $MAPbI_3$. Considering the similar nature of the reconstructions for both MA-based perovskites, it is reasonable to hypothesize that reconstructions similar to what was imaged here on $CsPbBr_3$ will also occur on $CsPbI_3$.

It is also worth mentioning mixed halide systems. As discussed in Chapter 4, different halides substituted into the $MAPbBr_3$ perovskite lattice showed a random distribution and exhibited a difference in apparent height in STM images. It would be especially interesting to perform a similar study on mixed halide Cs-based perovskites, as the greater asymmetry in the surface reconstructions of $CsPbBr_3$, especially the apparent height alternation in the armchair domain, may lead to interesting non-random halide substitution behavior. further supporting that the Cs cations are causing the new reconstructions seen in $CsPbBr_3$.

Lastly, a previous STM report on $MAPbI_3$ showed that the surface could be interconverted between the two different surface reconstructions via imaging at different conditions STM tip.[151] Such a behavior was not observed for $CsPbBr_3$, suggesting a higher stability of the surface layer. The relative stability of the Cs- and MA-based perovskite will be explored further in the next section.

6.6 Stability of the $CsPbBr_3$ surface

In order to better understand the origin of the high stability of Cs-based perovskites, the chemical state evolution over time of a $CsPbBr_3$ half-cell sample was monitored by XPS. After fabrication, the samples were stored and measured in a UHV environment. This essentially eliminates environmental factors like humidity, oxygen, or degradation due to interaction with a hole transport layer. The Cs *3d*, Br *3d* and Pb *4f* XPS peaks were measured at various time intervals over a period of 224h and no change was seen in any of the three chemical states over this time period (Fig. 6.4). This is in stark contrast to the results described in Chapter 4 for $MAPbBr_3$ using a similar approach (Fig. 4.6), in which a Pb(0) peak appeared after 4h of storage in UHV. Pb(0) is an indicator of perovskite degradation, and the lack of a Pb(0) peak in the $CsPbBr_3$ experiment clearly shows the higher stability of the Cs-based perovskite compared to those with MA^+ in the A site. The fact that such a stark difference in stability is seen even when many environmental

factors are suppressed in UHV suggests that the lower volatility of the Cs^+ compared to MA^+ plays an important role in the excellent stability shown by devices that use Cs-containing perovskite. The superior intrinsic stability may also arise in part from the higher stability of the two surface reconstructions, as mentioned in the previous section.

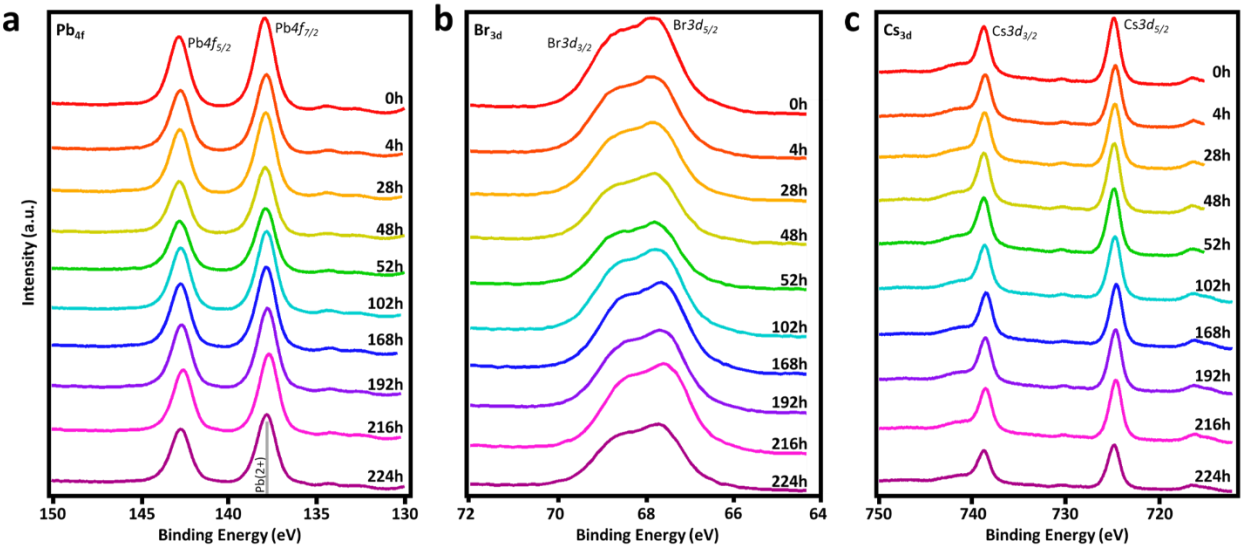

Figure 6.4 Stability test of $CsPbBr_3$ half-cells. Time evolution of the Pb *4f* (a), Br *3d* (b), and Cs *3d* (c) XPS spectra of $CsPbBr_3$ in a half-cell architecture (Glass/FTO/TiO_2/$CsPbBr_3$). The XPS spectra remain unchanged after 224h storage in UHV conditions. Notably, a Pb(0) peak, which is a typical indicator of perovskite degradation, does not appear.

Section 6.7 Summary

In this chapter, the atomic structure of the surface of $CsPbBr_3$ was determined in real space by STM imaging and corroborated by DFT simulations. Two different domains were observed via STM, the stripe domain and the armchair domain, both of which featured asymmetric spacing between Br^- pairs. The armchair domain also exhibited alternating rows of Br^- pairs that had different apparent heights. DFT calculations showed that the different domains occur due to different positioning of the Cs cations and the resulting interactions with the neighboring Br anions in the surface layer. The armchair domain shows a particularly interesting behavior, where the Cs cations occupy three unique vertical positions. The Br anions form pairs with differing apparent heights, depending on whether the neighboring Cs cations are in up positions (bright Br^- pairs) or in middle and down positions (dark Br^- pairs). Conversely, in the stripe phase, all the Cs cations

occupy the same vertical position. Additionally, the stripe phase was more common in STM images and determined by DFT to be the more stable domain of the two.

Both the surface reconstructions and the overall material stability of $CsPbBr_3$ was compared with $MAPbBr_3$. The material stability was evaluated by monitoring the chemical states of the perovskite over time via XPS. $CsPbBr_3$ showed no sign of degradation, in the form of a Pb(0) peak, after 224h, whereas $MAPbBr_3$ showed signs of degradation after just 4h. This difference in UHV, where environment-induced degradation is minimal, suggests that the lower volatility of the Cs cation compared to the MA cation may be a significant contributor to the material stability, and subsequently Cs containing perovskite-based device stability.

The surface reconstructions of the Cs- and MA-perovskites were found to differ in important ways. While the two reconstructions in $MAPbBr_3$ are due to different relative orientations of the asymmetric MA cation, the same mechanism cannot be at work for $CsPbBr_3$, where the Cs cation is spherically symmetric. For $CsPbBr_3$, it is the differing vertical positions of the Cs cations that lead to two surface reconstructions, both of which are distinct from the reconstructions seen on $MAPbBr_3$. This suggests that the identity of the cations plays a strong role determining the surface structure of perovskites. This hypothesis is strengthened by the fact that $MAPbBr_3$ and $MAPbI_3$ exhibit near identical surface reconstructions, despite the differing halide. Thus, it is also anticipated that $CsPbI_3$ likely has surface reconstructions very similar to those imaged here for $CsPbBr_3$.

The original motivation for this work was not only to understand the surface of $CsPbBr_3$, but to use the results as a building block for studies on mixed cation perovskite materials. The work in this chapter highlights the strong influence the cation has on the surface. Surfaces of mixed cation perovskites likely have an even more complex surface reconstruction behavior that depends sensitively on the relative ratio of the cations as well as their distribution in the film. This provides an exciting avenue for future surface science research into a sub-class of perovskites that is especially relevant to the goal of producing perovskite devices with higher stability.

Conclusion

In this thesis, perovskite surfaces and the device-relevant $MAPbX_3$-CuPc interface were characterized in an ultra-high vacuum environment at the atomic scale via scanning tunneling microscopy (STM), and the electronic properties and stability of the perovskite surfaces were explored via ultraviolet and X-ray photoelectron spectroscopy (XPS and UPS), respectively. Where appropriate, density functional theory (DFT) calculations performed by collaborators were utilized to corroborate and interpret experimental results. As described in Section 1.4, surface passivation and interfacial properties are key factors in the further optimization of OHP-based photovoltaic devices, and this thesis provides fundamental characterization of the atomic structure at the perovskite surface.

Aside from surface passivation, defect passivation is also a major strategy for device improvement. In Chapter 3, intrinsic defects that occur at the perovskite surface are characterized. It was observed that vacancy defects clusters, not just single point vacancies, can occur at the $MAPbBr_3$ surface. It was determined that these vacancy clusters alter the local work function, thus potentially affecting energy level alignment and charge transfer at interfaces in a device. These vacancy defects were assigned to be neutral MABr vacancies, based on energy of formation calculations, with corroborating experimental data. Numerous dynamic events were imaged via STM, including vacancy-assisted ion transport, both along the perovskite surface, as well as to and from the bulk. DFT simulations identified favorable ion migration mechanisms, and found a difference in migration activation energy depending on crystal direction. This underscores how crystal orientation distribution in the polycrystalline films used in devices can affect device stabilization and performance. Br^- pair reorientation was also observed, enabling long-range dynamics. This phenomenon was found to potentially be aided by the presence of vacancies. Visualization of these dynamic events provides a unique perspective on the processes occurring at the perovskite surface.

Chlorine incorporation into perovskite materials has been employed as a method to improve performance, and it was suggested that chlorine may passivate defect induced traps. Halide mixing is also a general method for modifying the optoelectronic properties of perovskite materials. In Chapter 4 the effect of halide mixing on the surface of $MAPbBr_3$ was explored. Upon

sublimation of the corresponding lead halide onto the $MAPbBr_3$ surface, it was found that I^- and Cl^- could substitute Br^- at the surface. STM images, corroborated by DFT calculations, showed that these halides are incorporated into the lattice with a random distribution. DFT calculations of the decomposition energy of the perovskite found there is an increase in stability with low Cl-substitution ratios. The existence of an optimal ratio of Cl-substitution was found to result from the balance between a beneficial Pb-X bond strength increase and a detrimental lattice strain increase. This increased stability at low Cl-substitution ratios was verified experimentally by XPS measurements on half-cell architectures stored in UHV. The appearance of a Pb(0) peak in the Pb 4f spectrum was used as an indicator of surface material degradation. While a Pb(0) peak appeared after only 4h for pure $MAPbBr_3$, a Pb(0) peak only appeared after 116h for the 18% Cl-substituted sample, showing a much greater stability.

Although it important to understand and characterize perovskite surfaces, these ultimately only constitute half of the interface in a device, therefore in Chapter 5 the interface between $MAPbI_3$ and CuPc was explored. It was found that CuPc has a relatively weak interaction with the underlying perovskite, as evidenced by the extreme rarity of individual CuPc molecules. Instead, CuPc molecules formed SA layers, even at sub-monolayer coverages. This signifies that the CuPc intermolecular forces are greater than the molecule-substrate binding forces. This is in disagreement with a previous report that proposed a flat-lying layer of CuPc exists at the interface, based on DFT binding energy calculations that only considered a single CuPc molecule. The results in this chapter show the importance of considering an ensemble of molecules. Knowing the CuPc orientation is important because the orientation of organic molecules can alter interfacial properties. It should be noted that the exact orientation and tilt angle of the CuPc molecules in the SA layers observed is not yet known. Some experimental evidence is consistent with an α-CuPc stacking structure, but some discrepancies prevent a definitive assignment at this time.

Non-perovskite domains were also observed on the $MAPbI_3$ films, and the CuPc was found to have a comparatively stronger interaction with these domains. In contrast to $MAPbI_3$, individual, flat-lying CuPc molecules were found in close proximity to each other on the non-perovskite domain. This shows a molecule-substrate interaction that is stronger than the CuPc intermolecular force. The identity of the non-perovskite domain is still not clear, although tentative candidates are PbI_2 or an iodine monolayer. The difference in molecular adsorption behavior has important

implications for the interface of devices that utilize non-stoichiometric perovskite films with organic HTLs. Altering the perovskite stoichiometry can have unintended effects on interfacial properties as it may also alter the other half of the interface by changing the adsorption orientation of organic molecule HTLs.

The previous chapters dealt with MA-based perovskites, but many high performing and highly stable perovskite formulations now involve incorporation of Cs cations into the A site. As an initial step towards understanding Cs-containing mixed cation perovskites, and also to understand the surface properties of all-inorganic perovskites, the atomic structure and stability of the $CsPbBr_3$ surface was characterized in Chapter 6. STM measurements revealed that two different surface reconstructions exist at the $CsPbBr_3$ surface, the "stripe" reconstruction and the "armchair" reconstruction. These two surface reconstructions are both distinct from the reconstructions seen on the surface of MA-based perovskites. The stripe reconstruction was found to be formed by an alternating long and short spacing between Br^- pairs, and each stripe was composed of two rows of Br^- pairs with a relative orientation of around 77°. The armchair reconstruction featured alternating rows of brighter and darker Br^- pairs. DFT calculations showed the difference in apparent height of the two rows was caused by the fact that Cs cations in the surface layer can occupy 3 different vertical positions. The vertical position of the two nearest Cs cations determined the brightness of the Br^- pairs in the STM images. The stability of $CsPbBr_3$ was also checked via XPS. Even after 224h of storage in UHV, there was no appearance of a Pb(0) peak, indicating vastly superior stability in comparison to $MAPbBr_3$, which showed signs of degradation after only 4h. This stability study was performed in UHV, where environmental factors such as oxygen or moisture are at a minimum. Therefore, the superior stability in UHV is tentatively assigned to the lower volatility of Cs^+ in comparison with MA^+.

Overall, this thesis investigated perovskite surfaces and device-relevant interfaces at the atomic scale using STM and evaluated stability by observing changes in XPS spectra as a function of time. This thesis provides valuable fundamental understanding and direct visualization of perovskite surfaces and interfaces that can aid applied research in the quest to optimize interfaces for superior OHP-based solar cell performance and stability.

References

(1) Chih, Y.-K.; Wang, J.-C.; Yang, R.-T.; Liu, C.-C.; Chang, Y.-C.; Fu, Y.-S.; Lai, W.-C.; Chen, P.; Wen, T.-C.; Huang, Y.-C.; Tsao, C.-S.; Guo, T.-F. NiOx Electrode Interlayer and CH3NH2/CH3NH3PbBr3 Interface Treatment to Markedly Advance Hybrid Perovskite-Based Light-Emitting Diodes. *Adv. Mater.* **2016**, *28* (39), 8687-8694.

(2) Liu, Y.; Cui, J. Y.; Du, K.; Tian, H.; He, Z. F.; Zhou, Q. H.; Yang, Z. L.; Deng, Y. Z.; Chen, D.; Zuo, X. B.; Ren, Y.; Wang, L.; Zhu, H. M.; Zhao, B. D.; Di, D. W.; Wang, J. P.; Friend, R. H.; Jin, Y. Z. Efficient Blue Light-Emitting Diodes Based on Quantum-Confined Bromide Perovskite Nanostructures. *Nat. Photonics* **2019**, *13* (11), 760-764.

(3) Jiang, M. W.; Hu, Z. H.; Liu, Z. H.; Wu, Z. F.; Ono, L. K.; Qi, Y. B. Engineering Green-to-Blue Emitting CsPbBr3 Quantum-Dot Films with Efficient Ligand Passivation. *ACS Energy Lett.* **2019**, *4* (11), 2731-2738.

(4) Lin, K. B.; Xing, J.; Quan, L. N.; de Arquer, F. P. G.; Gong, X. W.; Lu, J. X.; Xie, L. Q.; Zhao, W. J.; Zhang, D.; Yan, C. Z.; Li, W. Q.; Liu, X. Y.; Lu, Y.; Kirman, J.; Sargent, E. H.; Xiong, Q. H.; Wei, Z. H. Perovskite Light-Emitting Diodes with External Quantum Efficiency Exceeding 20 Per Cent. *Nature* **2018**, *562* (7726), 245-248.

(5) Fu, Y. P.; Zhu, H. M.; Stoumpos, C. C.; Ding, Q.; Wang, J.; Kanatzidis, M. G.; Zhu, X. Y.; Jin, S. Broad Wavelength Tunable Robust Lasing from Single-Crystal Nanowires of Cesium Lead Halide Perovskites (CsPbX3, X = Cl, Br, I). *ACS Nano* **2016**, *10* (8), 7963-7972.

(6) Eaton, S. W.; Lai, M. L.; Gibson, N. A.; Wong, A. B.; Dou, L. T.; Ma, J.; Wang, L. W.; Leone, S. R.; Yang, P. D. Lasing in Robust Cesium Lead Halide Perovskite Nanowires. *P. Natl. Acad. Sci. U.S.A.* **2016**, *113* (8), 1993-1998.

(7) Kojima, A.; Teshima, K.; Shirai, Y.; Miyasaka, T. Organometal Halide Perovskites as Visible-Light Sensitizers for Photovoltaic Cells. *J. Am. Chem. Soc.* **2009**, *131* (17), 6050-6051.

(8) Miyata, A.; Mitioglu, A.; Plochocka, P.; Portugall, O.; Wang, J. T.-W.; Stranks, S. D.; Snaith, H. J.; Nicholas, R. J. Direct Measurement of the Exciton Binding Energy and Effective Masses for Charge Carriers in Organic-Inorganic Tri-Halide Perovskites. *Nat. Phys.* **2015**, *11* (7), 582-587.

(9) Stranks, S. D.; Eperon, G. E.; Grancini, G.; Menelaou, C.; Alcocer, M. J. P.; Leijtens, T.; Herz, L. M.; Petrozza, A.; Snaith, H. J. Electron-Hole Diffusion Lengths Exceeding 1 Micrometer in an Organometal Trihalide Perovskite Absorber. *Science* **2013**, *342* (6156), 341-344.

(10) Kim, H.-S.; Lee, C.-R.; Im, J.-H.; Lee, K.-B.; Moehl, T.; Marchioro, A.; Moon, S.-J.; Humphry-Baker, R.; Yum, J.-H.; Moser, J. E.; Grätzel, M.; Park, N.-G. Lead Iodide Perovskite Sensitized All-Solid-State Submicron Thin Film Mesoscopic Solar Cell with Efficiency Exceeding 9%. *Sci. Rep.* **2012**, *2*, 591.

(11) Lee, M. M.; Teuscher, J.; Miyasaka, T.; Murakami, T. N.; Snaith, H. J. Efficient Hybrid Solar Cells Based on Meso-Superstructured Organometal Halide Perovskites. *Science* **2012**, *338* (6107), 643-647.

(12) NREL National Renewable Energy Laboratory (NREL) Solar Cell Efficiency Chart. http://www.nrel.gov/ncpv/images/efficiency_chart.jpg (Accessed Apr. 7th, 2020).

(13) Heo, J. H.; You, M. S.; Chang, M. H.; Yin, W.; Ahn, T. K.; Lee, S. J.; Sung, S. J.; Kim, D. H.; Im, S. H. Hysteresis-Less Mesoscopic CH(3)NH(3)Pbl(3) Perovskite Hybrid Solar Cells by Introduction of Li-Treated TiO2 Electrode. *Nano Energy* **2015**, *15*, 530-539.

(14) Burschka, J.; Pellet, N.; Moon, S. J.; Humphry-Baker, R.; Gao, P.; Nazeeruddin, M. K.; Gratzel, M. Sequential Deposition as a Route to High-Performance Perovskite-Sensitized Solar Cells. *Nature* **2013**, *499* (7458), 316-319.

(15) Chen, Q.; Zhou, H. P.; Hong, Z. R.; Luo, S.; Duan, H. S.; Wang, H. H.; Liu, Y. S.; Li, G.; Yang, Y. Planar Heterojunction Perovskite Solar Cells Via Vapor-Assisted Solution Process. *J. Am. Chem. Soc.* **2014**, *136* (2), 622-625.

(16) Ono, L. K.; Wang, S. H.; Kato, Y.; Raga, S. R.; Qi, Y. B. Fabrication of Semi-Transparent Perovskite Films with Centimeter-Scale Superior Uniformity by the Hybrid Deposition Method. *Energ. Environ. Sci.* **2014**, *7* (12), 3989-3993.
(17) Wang, S. H.; Ono, L. K.; Leyden, M. R.; Kato, Y.; Raga, S. R.; Lee, M. V.; Qi, Y. B. Smooth Perovskite Thin Films and Efficient Perovskite Solar Cells Prepared by the Hybrid Deposition Method. *J. Mater. Chem. A* **2015**, *3* (28), 14631-14641.
(18) Leyden, M. R.; Ono, L. K.; Raga, S. R.; Kato, Y.; Wang, S. H.; Qi, Y. B. High Performance Perovskite Solar Cells by Hybrid Chemical Vapor Deposition. *J. Mater. Chem. A* **2014**, *2* (44), 18742-18745.
(19) Tait, J. G.; Manghooli, S.; Qiu, W.; Rakocevic, L.; Kootstra, L.; Jaysankar, M.; de la Huerta, C. A. M.; Paetzold, U. W.; Gehlhaar, R.; Cheyns, D.; Heremans, P.; Poortmans, J. Rapid Composition Screening for Perovskite Photovoltaics Via Concurrently Pumped Ultrasonic Spray Coating. *J. Mater. Chem. A* **2016**, *4* (10), 3792-3797.
(20) Chandrasekhar, P. S.; Kumar, N.; Swami, S. K.; Dutta, V.; Komarala, V. K. Fabrication of Perovskite Films Using an Electrostatic Assisted Spray Technique: The Effect of the Electric Field on Morphology, Crystallinity and Solar Cell Performance. *Nanoscale* **2016**, *8* (12), 6792-6800.
(21) Zhou, Y. Y.; Yang, M. J.; Wu, W. W.; Vasiliev, A. L.; Zhu, K.; Padture, N. P. Room-Temperature Crystallization of Hybrid-Perovskite Thin Films Via Solvent-Solvent Extraction for High-Performance Solar Cells. *J. Mater. Chem. A* **2015**, *3* (15), 8178-8184.
(22) Deng, Y. H.; Wang, Q.; Yuan, Y. B.; Huang, J. S. Vividly Colorful Hybrid Perovskite Solar Cells by Doctor-Blade Coating with Perovskite Photonic Nanostructures. *Mater. Horiz.* **2015**, *2* (6), 578-583.
(23) Ju, Y.; Park, S. Y.; Yeom, K. M.; Noh, J. H.; Jung, H. S. Single-Solution Bar-Coated Halide Perovskite Films Via Mediating Crystallization for Scalable Solar Cell Fabrication. *ACS Appl. Mater. Interfaces* **2019**, *11* (12), 11537-11544.
(24) Li, X.; Bi, D. Q.; Yi, C. Y.; Decoppet, J. D.; Luo, J. S.; Zakeeruddin, S. M.; Hagfeldt, A.; Gratzel, M. A Vacuum Flash-Assisted Solution Process for High-Efficiency Large-Area Perovskite Solar Cells. *Science* **2016**, *353* (6294), 58-62.
(25) Gao, L.; Chen, L.; Huang, S.; Li, X.; Yang, G. Series and Parallel Module Design for Large-Area Perovskite Solar Cells. *ACS Appl. Energy Mater.* **2019**, *2* (5), 3851-3859.
(26) Qiu, L. B.; He, S. S.; Ono, L. K.; Liu, S. Z.; Qi, Y. B. Scalable Fabrication of Metal Halide Perovskite Solar Cells and Modules. *ACS Energy Lett.* **2019**, *4* (9), 2147-2167.
(27) Bailie, C. D.; McGehee, M. D. High-Efficiency Tandem Perovskite Solar Cells. *MRS Bulletin* **2015**, *40* (08), 681-686.
(28) McMeekin, D. P.; Sadoughi, G.; Rehman, W.; Eperon, G. E.; Saliba, M.; Horantner, M. T.; Haghighirad, A.; Sakai, N.; Korte, L.; Rech, B.; Johnston, M. B.; Herz, L. M.; Snaith, H. J. A Mixed-Cation Lead Mixed-Halide Perovskite Absorber for Tandem Solar Cells. *Science* **2016**, *351* (6269), 151-155.
(29) Albrecht, S.; Saliba, M.; Correa Baena, J. P.; Lang, F.; Kegelmann, L.; Mews, M.; Steier, L.; Abate, A.; Rappich, J.; Korte, L.; Schlatmann, R.; Nazeeruddin, M. K.; Hagfeldt, A.; Grätzel, M.; Rech, B. Monolithic Perovskite/Silicon-Heterojunction Tandem Solar Cells Processed at Low Temperature. *Energy Environ. Sci.* **2016**, *9* (1), 81-88.
(30) Tong, J.; Song, Z.; Kim, D. H.; Chen, X.; Chen, C.; Palmstrom, A. F.; Ndione, P. F.; Reese, M. O.; Dunfield, S. P.; Reid, O. G.; Liu, J.; Zhang, F.; Harvey, S. P.; Li, Z.; Christensen, S. T.; Teeter, G.; Zhao, D.; Al-Jassim, M. M.; van Hest, M. F. A. M.; Beard, M. C.; Shaheen, S. E.; Berry, J. J.; Yan, Y.; Zhu, K. Carrier Lifetimes of >1 μs in Sn-Pb Perovskites Enable Efficient All-Perovskite Tandem Solar Cells. *Science* **2019**, *364* (6439), 475-479.
(31) Li, Y.; Meng, L.; Yang, Y.; Xu, G.; Hong, Z.; Chen, Q.; You, J.; Li, G.; Yang, Y.; Li, Y. High-Efficiency Robust Perovskite Solar Cells on Ultrathin Flexible Substrates. *Nat. Commun.* **2016**, *7*, 10214.

(32) Yoon, J.; Sung, H.; Lee, G.; Cho, W.; Ahn, N.; Jung, H. S.; Choi, M. Superflexible, High-Efficiency Perovskite Solar Cells Utilizing Graphene Electrodes: Towards Future Foldable Power Sources. *Energy Environ. Sci.* **2017**, *10* (1), 337-345.
(33) Lee, G.; Kim, M.-c.; Choi, Y. W.; Ahn, N.; Jang, J.; Yoon, J.; Kim, S. M.; Lee, J.-G.; Kang, D.; Jung, H. S.; Choi, M. Ultra-Flexible Perovskite Solar Cells with Crumpling Durability: Toward a Wearable Power Source. *Energy Environ. Sci.* **2019**, *12* (10), 3182-3191.
(34) Sung, H.; Ahn, N.; Jang, M. S.; Lee, J. K.; Yoon, H.; Park, N. G.; Choi, M. Transparent Conductive Oxide-Free Graphene-Based Perovskite Solar Cells with over 17% Efficiency. *Adv. Energy Mater.* **2016**, *6* (3), 1501873.
(35) Chen, S. S.; Lei, L.; Yang, S. W.; Liu, Y.; Wang, Z. S., Characterization of Perovskite Obtained from Two-Step Deposition on Mesoporous Titania. *ACS Appl. Mater. Inter.* **2015**, *7* (46), 25770-25776.
(36) Bu, T.; Li, J.; Zheng, F.; Chen, W.; Wen, X.; Ku, Z.; Peng, Y.; Zhong, J.; Cheng, Y.-B.; Huang, F. Universal Passivation Strategy to Slot-Die Printed SnO2 for Hysteresis-Free Efficient Flexible Perovskite Solar Module. *Nat. Commun.* **2018**, *9* (1), 4609.
(37) Qiu, L.; Liu, Z.; Ono, L. K.; Jiang, Y.; Son, D.-Y.; Hawash, Z.; He, S.; Qi, Y.B. Scalable Fabrication of Stable High Efficiency Perovskite Solar Cells and Modules Utilizing Room Temperature Sputtered SnO2 Electron Transport Layer. *Adv. Funct. Mater.* **2019**, *29* (47), 1806779.
(38) Han, G. S.; Kim, J.; Bae, S.; Han, S.; Kim, Y. J.; Gong, O. Y.; Lee, P.; Ko, M. J.; Jung, H. S. Spin-Coating Process for 10 Cm × 10 Cm Perovskite Solar Modules Enabled by Self-Assembly of SnO2 Nanocolloids. *ACS Energy Lett.* **2019**, *4* (8), 1845-1851.
(39) Heo, J. H.; Han, H. J.; Kim, D.; Ahn, T. K.; Im, S. H. Hysteresis-Less Inverted CH3NH3PbI3 Planar Perovskite Hybrid Solar Cells with 18.1% Power Conversion Efficiency. *Energy Environ. Sci.* **2015**, *8* (5), 1602-1608.
(40) Ono, L. K.; Juárez-Pérez, E. J.; Qi, Y.B. Progress on Novel Perovskite Materials and Solar Cells with Mixed Cations and Halide Anions. *ACS Appl. Mater. Interfaces* **2017**, *9*, 30197−30246.
(41) Zhang, W.; Anaya, M.; Lozano, G.; Calvo, M. E.; Johnston, M. B.; Miguez, H.; Snaith, H. J. Highly Efficient Perovskite Solar Cells with Tunable Structural Color. *Nano Lett.* **2015**, *15* (3), 1698-1702.
(42) Hao, F.; Stoumpos, C. C.; Cao, D. H.; Chang, R. P. H.; Kanatzidis, M. G. Lead-Free Solid-State Organic-Inorganic Halide Perovskite Solar Cells. *Nat. Photonics* **2014**, *8* (6), 489-494.
(43) Yokoyama, T.; Cao, D. Y. H.; Stoumpos, C. C.; Song, T. B.; Sato, Y.; Aramaki, S.; Kanatzidis, M. G. Overcoming Short-Circuit in Lead-Free CH3NH3SnI3 Perovskite Solar Cells Via Kinetically Controlled Gas-Solid Reaction Film Fabrication Process. *J. Phys. Chem. Lett.* **2016**, *7* (5), 776-782.
(44) Eperon, G. E.; Stranks, S. D.; Menelaou, C.; Johnston, M. B.; Herz, L. M.; Snaith, H. J. Formamidinium Lead Trihalide: A Broadly Tunable Perovskite for Efficient Planar Heterojunction Solar Cells. *Energy Environ. Sci.* **2014**, *7* (3), 982-988.
(45) Jeon, N. J.; Noh, J. H.; Yang, W. S.; Kim, Y. C.; Ryu, S.; Seo, J.; Seok, S. I. Compositional Engineering of Perovskite Materials for High-Performance Solar Cells. *Nature* **2015**, *517* (7535), 476-480.
(46) Saliba, M.; Matsui, T.; Seo, J. Y.; Domanski, K.; Correa-Baena, J. P.; Nazeeruddin, M. K.; Zakeeruddin, S. M.; Tress, W.; Abate, A.; Hagfeldt, A.; Gratzel, M. Cesium-Containing Triple Cation Perovskite Solar Cells: Improved Stability, Reproducibility and High Efficiency. *Energy Environ. Sci.* **2016**, *9* (6), 1989-1997.
(47) Tong, G. Q.; Chen, T. T.; Li, H.; Qiu, L. B.; Liu, Z. H.; Dang, Y. Y.; Song, W. T.; Ono, L. K.; Jiang, Y.; Qi, Y. B. Phase Transition Induced Recrystallization and Low Surface Potential Barrier Leading to 10.91%-Efficient CsPbBr3 Perovskite Solar Cells. *Nano Energy* **2019**, *65*, 104015.
(48) Saliba, M.; Matsui, T.; Domanski, K.; Seo, J. Y.; Ummadisingu, A.; Zakeeruddin, S. M.; Correa-Baena, J. P.; Tress, W. R.; Abate, A.; Hagfeldt, A.; Gratzel, M. Incorporation of Rubidium Cations into Perovskite Solar Cells Improves Photovoltaic Performance. *Science* **2016**, *354* (6309), 206-209.

(49) Son, D. Y.; Kim, S. G.; Seo, J. Y.; Lee, S. H.; Shin, H.; Lee, D.; Park, N. G. Universal Approach toward Hysteresis-Free Perovskite Solar Cell Via Defect Engineering. *J. Am. Chem. Soc.* **2018**, *140* (4), 1358-1364.
(50) Chen, Q.; Zhou, H.; Song, T. B.; Luo, S.; Hong, Z.; Duan, H. S.; Dou, L.; Liu, Y.; Yang, Y. Controllable Self-Induced Passivation of Hybrid Lead Iodide Perovskites toward High Performance Solar Cells. *Nano Lett.* **2014**, *14* (7), 4158-63.
(51) Jacobsson, T. J.; Correa-Baena, J. P.; Anaraki, E. H.; Philippe, B.; Stranks, S. D.; Bouduban, M. E. F.; Tress, W.; Schenk, K.; Teuscher, J.; Moser, J. E.; Rensmo, H.; Hagfeldt, A. Unreacted PbI2 as a Double-Edged Sword for Enhancing the Performance of Perovskite Solar Cells. *J. Am. Chem. Soc.* **2016**, *138* (32), 10331-10343.
(52) Cohen, B. E.; Gamliel, S.; Etgara, L. Parameters Influencing the Deposition of Methylammonium Lead Halide Iodide in Hole Conductor Free Perovskite-Based Solar Cells. *APL Mater.* **2014**, *2* (8), 081502.
(53) Hawash, Z.; Raga, S. R.; Son, D.-Y.; Ono, L. K.; Park, N.-G.; Qi, Y.B. Interfacial Modification of Perovskite Solar Cells Using an Ultrathin MAI Layer Leads to Enhanced Energy Level Alignment, Efficiencies, and Reproducibility. *J. Phys. Chem. Lett.* **2017**, 3947-3953.
(54) deQuilettes, D. W.; Vorpahl, S. M.; Stranks, S. D.; Nagaoka, H.; Eperon, G. E.; Ziffer, M. E.; Snaith, H. J.; Ginger, D. S. Impact of Microstructure on Local Carrier Lifetime in Perovskite Solar Cells. *Science* **2015**, *348* (6235), 683-686.
(55) Shao, Y.; Fang, Y.; Li, T.; Wang, Q.; Dong, Q.; Deng, Y.; Yuan, Y.; Wei, H.; Wang, M.; Gruverman, A.; Shield, J.; Huang, J. Grain Boundary Dominated Ion Migration in Polycrystalline Organic–Inorganic Halide Perovskite Films. *Energy Environ. Sci.* **2016**, *9* (5), 1752-1759.
(56) Jiang, Y.; Juarez-Perez, E. J.; Ge, Q.; Wang, S.; Leyden, M. R.; Ono, L. K.; Raga, S. R.; Hu, J.; Qi, Y.B. Post-Annealing of MAPbI3 Perovskite Films with Methylamine for Efficient Perovskite Solar Cells. *Mater. Horiz.* **2016**, *3*, 548-555.
(57) Nie, W. Y.; Tsai, H. H.; Asadpour, R.; Blancon, J. C.; Neukirch, A. J.; Gupta, G.; Crochet, J. J.; Chhowalla, M.; Tretiak, S.; Alam, M. A.; Wang, H. L.; Mohite, A. D. High-Efficiency Solution-Processed Perovskite Solar Cells with Millimeter-Scale Grains. *Science* **2015**, *347* (6221), 522-525.
(58) Cappel, U. B.; Daeneke, T.; Bach, U., Oxygen-Induced Doping of Spiro-MeOTAD in Solid-State Dye-Sensitized Solar Cells and Its Impact on Device Performance. *Nano Lett.* **2012**, *12* (9), 4925-4931.
(59) Juarez-Perez, E. J.; Leyden, M. R.; Wang, S.; Ono, L. K.; Hawash, Z.; Qi, Y.B. Role of the Dopants on the Morphological and Transport Properties of Spiro-MeOTAD Hole Transport Layer. *Chem. Mater.* **2016**, *28* (16), 5702-5709.
(60) Jiang, X. Q.; Wang, D. P.; Yu, Z.; Ma, W. Y.; Li, H. B.; Yang, X. C.; Liu, F.; Hagfeldt, A.; Sun, L. C. Molecular Engineering of Copper Phthalocyanines: A Strategy in Developing Dopant-Free Hole-Transporting Materials for Efficient and Ambient-Stable Perovskite Solar Cells. *Adv. Energy Mater.* **2019**, *9* (4), 1803287.
(61) Yang, G.; Wang, Y. L.; Xu, J. J.; Lei, H. W.; Chen, C.; Shan, H. Q.; Liu, X. Y.; Xu, Z. X.; Fang, G. J. A Facile Molecularly Engineered Copper (II) Phthalocyanine as Hole Transport Material for Planar Perovskite Solar Cells with Enhanced Performance and Stability. *Nano Energy* **2017**, *31*, 322-330.
(62) Cho, K. T.; Trukhina, O.; Roldan-Carmona, C.; Ince, M.; Gratia, P.; Grancini, G.; Gao, P.; Marszalek, T.; Pisula, W.; Reddy, P. Y.; Torres, T.; Nazeeruddin, M. K. Molecularly Engineered Phthalocyanines as Hole-Transporting Materials in Perovskite Solar Cells Reaching Power Conversion Efficiency of 17.5%. *Adv. Energy Mater.* **2017**, *7* (7), 1601733.
(63) Wang, J. M.; Wang, Z. K.; Li, M.; Zhang, C. C.; Jiang, L. L.; Hu, K. H.; Ye, Q. Q.; Liao, L. S. Doped Copper Phthalocyanine Via an Aqueous Solution Process for Normal and Inverted Perovskite Solar Cells. *Adv. Energy Mater.* **2018**, *8* (2), 1701688.
(64) Wang, Y. L.; Zheng, X. L.; Liu, X. Y.; Feng, Y. M.; Shan, H. Q.; Dong, L.; Fang, G. J.; Xu, Z. X. A Study of Different Central Metals in Octamethyl-Substituted Phthalocyanines as Dopant-Free Hole-Transport Layers for Planar Perovskite Solar Cells. *Org. Electron.* **2018**, *56*, 276-283.

(65) Cheng, M.; Li, Y. Y.; Safdari, M.; Chen, C.; Liu, P.; Kloo, L.; Sun, L. C. Efficient Perovskite Solar Cells Based on a Solution Processable Nickel(II) Phthalocyanine and Vanadium Oxide Integrated Hole Transport Layer. *Adv. Energy Mater.* **2017**, *7* (14), 1602556.
(66) Kim, Y. C.; Yang, T. Y.; Jeon, N. J.; Im, J.; Jang, S.; Shin, T. J.; Shin, H. W.; Kim, S.; Lee, E.; Kim, S.; Noh, J. H.; Seok, S. I.; Seo, J. Engineering Interface Structures between Lead Halide Perovskite and Copper Phthalocyanine for Efficient and Stable Perovskite Solar Cells. *Energy Environ. Sci.* **2017**, *10* (10), 2109-2116.
(67) Yaghoobi Nia, N.; Lamanna, E.; Zendehdel, M.; Palma, A. L.; Zurlo, F.; Castriotta, L. A.; Di Carlo, A. Doping Strategy for Efficient and Stable Triple Cation Hybrid Perovskite Solar Cells and Module Based on Poly(3-Hexylthiophene) Hole Transport Layer. *Small* **2019**, *15* (49), 1904399.
(68) Yang, W. S.; Noh, J. H.; Jeon, N. J.; Kim, Y. C.; Ryu, S.; Seo, J.; Seok, S. I. High-Performance Photovoltaic Perovskite Layers Fabricated through Intramolecular Exchange. *Science* **2015**, *348* (6240), 1234-1237.
(69) Park, J. H.; Seo, J.; Park, S.; Shin, S. S.; Kim, Y. C.; Jeon, N. J.; Shin, H. W.; Ahn, T. K.; Noh, J. H.; Yoon, S. C.; Hwang, C. S.; Seok, S. I. Efficient CH3NH3PbI3 Perovskite Solar Cells Employing Nanostructured P-Type NiO Electrode Formed by a Pulsed Laser Deposition. *Adv. Mater.* **2015**, *27* (27), 4013-4019.
(70) Xie, F.; Chen, C.-C.; Wu, Y.; Li, X.; Cai, M.; Liu, X.; Yang, X.; Han, L., Vertical Recrystallization for Highly Efficient and Stable Formamidinium-Based Inverted-Structure Perovskite Solar Cells. *Energy Environ. Sci.* **2017**, *10* (9), 1942-1949.
(71) Rao, H.; Ye, S.; Sun, W.; Yan, W.; Li, Y.; Peng, H.; Liu, Z.; Bian, Z.; Li, Y.; Huang, C., A 19.0% Efficiency Achieved in Cuox-Based Inverted CH3NH3PbI3−xClx Solar Cells by an Effective Cl Doping Method. *Nano Energy* **2016**, *27*, 51-57.
(72) Kung, P.-K.; Li, M.-H.; Lin, P.-Y.; Chiang, Y.-H.; Chan, C.-R.; Guo, T.-F.; Chen, P. A Review of Inorganic Hole Transport Materials for Perovskite Solar Cells. *Adv. Mater. Interfaces* **2018**, *5* (22), 1800882.
(73) Kato, Y.; Ono, L. K.; Lee, M. V.; Wang, S. H.; Raga, S. R.; Qi, Y. B. Silver Iodide Formation in Methyl Ammonium Lead Iodide Perovskite Solar Cells with Silver Top Electrodes. *Adv. Mater. Interfaces* **2015**, *2* (13).
(74) Deng, Y.; Dong, Q.; Bi, C.; Yuan, Y.; Huang, J. Air-Stable, Efficient Mixed-Cation Perovskite Solar Cells with Cu Electrode by Scalable Fabrication of Active Layer. *Adv. Energy Mater.* **2016**, *6* (11), 1600372.
(75) Cacovich, S.; Ciná, L.; Matteocci, F.; Divitini, G.; Midgley, P. A.; Di Carlo, A.; Ducati, C. Gold and Iodine Diffusion in Large Area Perovskite Solar Cells under Illumination. *Nanoscale* **2017**, *9* (14), 4700-4706.
(76) Domanski, K.; Correa-Baena, J.-P.; Mine, N.; Nazeeruddin, M. K.; Abate, A.; Saliba, M.; Tress, W.; Hagfeldt, A.; Grätzel, M. Not All That Glitters Is Gold: Metal-Migration-Induced Degradation in Perovskite Solar Cells. *ACS Nano* **2016**, *10* (6), 6306-6314.
(77) Mei, A.; Li, X.; Liu, L.; Ku, Z.; Liu, T.; Rong, Y.; Xu, M.; Hu, M.; Chen, J.; Yang, Y.; Grätzel, M.; Han, H. A Hole-Conductor–Free, Fully Printable Mesoscopic Perovskite Solar Cell with High Stability. *Science* **2014**, *345* (6194), 295-298.
(78) You, P.; Liu, Z. K.; Tai, Q. D.; Liu, S. H.; Yan, F. Efficient Semitransparent Perovskite Solar Cells with Graphene Electrodes. *Adv. Mater.* **2015**, *27* (24), 3632-3638.
(79) Yan, K.; Wei, Z.; Li, J.; Chen, H.; Yi, Y.; Zheng, X.; Long, X.; Wang, Z.; Wang, J.; Xu, J.; Yang, S. High-Performance Graphene-Based Hole Conductor-Free Perovskite Solar Cells: Schottky Junction Enhanced Hole Extraction and Electron Blocking. *Small* **2015**, *11* (19), 2269-74.
(80) Chen, H. N.; Wei, Z. H.; He, H. X.; Zheng, X. L.; Wong, K. S.; Yang, S. H. Solvent Engineering Boosts the Efficiency of Paintable Carbon-Based Perovskite Solar Cells to Beyond 14%. *Adv. Energy Mater.* **2016**, *6* (8).

(81) He, S.; Qiu, L.; Son, D.-Y.; Liu, Z.; Juarez-Perez, E. J.; Ono, L. K.; Stecker, C.; Qi, Y., Carbon-Based Electrode Engineering Boosts the Efficiency of All Low-Temperature-Processed Perovskite Solar Cells. *ACS Energy Lett.* **2019**, *4* (9), 2032-2039.
(82) Leijtens, T.; Eperon, G. E.; Barker, A. J.; Grancini, G.; Zhang, W.; Ball, J. M.; Kandada, A. R. S.; Snaith, H. J.; Petrozza, A. Carrier Trapping and Recombination: The Role of Defect Physics in Enhancing the Open Circuit Voltage of Metal Halide Perovskite Solar Cells. *Energy Environ. Sci.* **2016**, *9* (11), 3472-3481.
(83) Yin, W. J.; Shi, T. T.; Yan, Y. F. Unusual Defect Physics in CH3NH3PbI3 Perovskite Solar Cell Absorber. *Appl. Phys. Lett.* **2014**, *104* (6), 063903.
(84) Sherkar, T. S.; Momblona, C.; Gil-Escrig, L.; Avila, J.; Sessolo, M.; Bolink, H. J.; Koster, L. J. A. Recombination in Perovskite Solar Cells: Significance of Grain Boundaries, Interface Traps, and Defect Ions. *ACS Energy Lett.* **2017**, *2* (5), 1214-1222.
(85) Snaith, H. J.; Abate, A.; Ball, J. M.; Eperon, G. E.; Leijtens, T.; Noel, N. K.; Stranks, S. D.; Wang, J. T.; Wojciechowski, K.; Zhang, W. Anomalous Hysteresis in Perovskite Solar Cells. *J. Phys. Chem. Lett.* **2014**, *5* (9), 1511-1515.
(86) Munoz-Garcia, A. B.; Ritzmann, A. M.; Pavone, M.; Keith, J. A.; Carter, E. A. Oxygen Transport in Perovskite-Type Solid Oxide Fuel Cell Materials: Insights from Quantum Mechanics. *Acc. Chem. Res.* **2014**, *47* (11), 3340-3348.
(87) O'Regan, B. C.; Barnes, P. R. F.; Li, X. E.; Law, C.; Paomares, E.; Marin-Beloqui, J. M. Optoelectronic Studies of Methylammonium Lead Iodide Perovskite Solar Cells with Mesoporous TiO2: Separation of Electronic and Chemical Charge Storage, Understanding Two Recombination Lifetimes, and the Evolution of Band Offsets During J-V Hysteresis. *J. Am. Chem. Soc.* **2015**, *137* (15), 5087-5099.
(88) Tress, W.; Marinova, N.; Moehl, T.; Zakeeruddin, S. M.; Nazeeruddin, M. K.; Gratzel, M. Understanding the Rate-Dependent J-V Hysteresis, Slow Time Component, and Aging in CH3NH3PbI3 Perovskite Solar Cells: The Role of a Compensated Electric Field. *Energy Environ. Sci.* **2015**, *8* (3), 995-1004.
(89) Yang, D. W.; Ming, W. M.; Shi, H. L.; Zhang, L. J.; Du, M. H. Fast Diffusion of Native Defects and Impurities in Perovskite Solar Cell Material CH3NH3PbI3. *Chem. Mater.* **2016**, *28* (12), 4349-4357.
(90) Azpiroz, J. M.; Mosconi, E.; Bisquert, J.; De Angelis, F. Defect Migration in Methylammonium Lead Iodide and Its Role in Perovskite Solar Cell Operation. *Energy Environ. Sci.* **2015**, *8* (7), 2118-2127.
(91) Eames, C.; Frost, J. M.; Barnes, P. R. F.; O'Regan, B. C.; Walsh, A.; Islam, M. S. Ionic Transport in Hybrid Lead Iodide Perovskite Solar Cells. *Nat. Commun.* **2015**, *6*, 7497.
(92) Baumann, A.; Vath, S.; Rieder, P.; Heiber, M. C.; Tvingstedt, K.; Dyakonov, V. Identification of Trap States in Perovskite Solar Cells. *J. Phys. Chem. Lett.* **2015**, *6* (12), 2350-2354.
(93) Yang, T. Y.; Gregori, G.; Pellet, N.; Gratzel, M.; Maier, J. The Significance of Ion Conduction in a Hybrid Organic-Inorganic Lead-Iodide-Based Perovskite Photosensitizer. *Angew. Chem. Int. Edit.* **2015**, *54* (27), 7905-7910.
(94) Almora, O.; Zarazua, I.; Mas-Marza, E.; Mora-Sero, I.; Bisquert, J.; Garcia-Belmonte, G. Capacitive Dark Currents, Hysteresis, and Electrode Polarization in Lead Halide Perovskite Solar Cells. *J. Phys. Chem. Lett.* **2015**, *6* (9), 1645-1652.
(95) Haruyama, J.; Sodeyama, K.; Han, L. Y.; Tateyama, Y. First-Principles Study of Ion Diffusion in Perovskite Solar Cell Sensitizers. *J. Am. Chem. Soc.* **2015**, *137* (32), 10048-10051.
(96) Meloni, S.; Moehl, T.; Tress, W.; Franckevicius, M.; Saliba, M.; Lee, Y. H.; Gao, P.; Nazeeruddin, M. K.; Zakeeruddin, S. M.; Rothlisberger, U.; Graetzel, M. Ionic Polarization-Induced Current-Voltage Hysteresis in CH3NH3PbX3 Perovskite Solar Cells. *Nat. Commun.* **2016**, *7*, 10334.
(97) Yuan, Y. B.; Chae, J.; Shao, Y. C.; Wang, Q.; Xiao, Z. G.; Centrone, A.; Huang, J. S. Photovoltaic Switching Mechanism in Lateral Structure Hybrid Perovskite Solar Cells. *Adv. Energy Mater.* **2015**, *5* (15), 1500615.

(98) Domanski, K.; Roose, B.; Matsui, T.; Saliba, M.; Turren-Cruz, S.-H.; Correa-Baena, J.-P.; Carmona, C. R.; Richardson, G.; Foster, J. M.; De Angelis, F.; Ball, J. M.; Petrozza, A.; Mine, N.; Nazeeruddin, M. K.; Tress, W.; Grätzel, M.; Steiner, U.; Hagfeldt, A.; Abate, A. Migration of Cations Induces Reversible Performance Losses over Day/Night Cycling in Perovskite Solar Cells. *Energy Environ. Sci.* **2017**, *10* (2), 604-613.
(99) Yang, J.-H.; Yin, W.-J.; Park, J.-S.; Wei, S.-H., Fast Self-Diffusion of Ions in CH3NH3PbI3: The Interstiticaly Mechanism Versus Vacancy-Assisted Mechanism. *J. Mater. Chem. A* **2016**, *4*, 13105-13112.
(100) Yu, H.; Lu, H. P.; Xie, F. Y.; Zhou, S.; Zhao, N. Native Defect-Induced Hysteresis Behavior in Organolead Iodide Perovskite Solar Cells. *Adv. Funct. Mater.* **2016**, *26* (9), 1411-1419.
(101) Li, C.; Tscheuschner, S.; Paulus, F.; Hopkinson, P. E.; Kiessling, J.; Kohler, A.; Vaynzof, Y.; Huettner, S. Iodine Migration and Its Effect on Hysteresis in Perovskite Solar Cells. *Adv. Mater.* **2016**, *28* (12), 2446-2454.
(102) Zhang, T.; Chen, H.; Bai, Y.; Xiao, S.; Zhu, L.; Hu, C.; Xue, Q.; Yang, S. Understanding the Relationship between Ion Migration and the Anomalous Hysteresis in High-Efficiency Perovskite Solar Cells: A Fresh Perspective from Halide Substitution. *Nano Energy* **2016**, *26*, 620-630.
(103) Slotcavage, D. J.; Karunadasa, H. I.; McGehee, M. D. Light-Induced Phase Segregation in Halide-Perovskite Absorbers. *ACS Energy Lett.* **2016**, *1* (6), 1199-1205.
(104) Hoke, E. T.; Slotcavage, D. J.; Dohner, E. R.; Bowring, A. R.; Karunadasa, H. I.; McGehee, M. D. Reversible Photo-Induced Trap Formation in Mixed-Halide Hybrid Perovskites for Photovoltaics. *Chem. Sci.* **2015**, *6* (1), 613-617.
(105) Bischak, C. G.; Hetherington, C. L.; Wu, H.; Aloni, S.; Ogletree, D. F.; Limmer, D. T.; Ginsberg, N. S. Origin of Reversible Photoinduced Phase Separation in Hybrid Perovskites. *Nano Lett.* **2017**, *17* (2), 1028-1033.
(106) Yuan, Y. B.; Li, T.; Wang, Q.; Xing, J.; Gruverman, A.; Huang, J. S. Anomalous Photovoltaic Effect in Organic-Inorganic Hybrid Perovskite Solar Cells. *Sci. Adv.* **2017**, *3* (3) 1602164.
(107) Kim, H. S.; Jang, I. H.; Ahn, N.; Choi, M.; Guerrero, A.; Bisquert, J.; Park, N. G. Control of I-V Hysteresis in CH3NH3PbI3 Perovskite Solar Cell. *J. Phys. Chem. Lett.* **2015**, *6* (22), 4633-4639.
(108) Carrillo, J.; Guerrero, A.; Rahimnejad, S.; Almora, O.; Zarazua, I.; Mas-Marza, E.; Bisquert, J.; Garcia-Belmonte, G. Ionic Reactivity at Contacts and Aging of Methylammonium Lead Triiodide Perovskite Solar Cells. *Adv. Energy Mater.* **2016**, *6* (9) 1502246.
(109) Chen, B.; Rudd, P. N.; Yang, S.; Yuan, Y.; Huang, J. Imperfections and Their Passivation in Halide Perovskite Solar Cells. *Chem. Soc. Rev.* **2019**, *48* (14), 3842-3867.
(110) Xu, J.; Buin, A.; Ip, A. H.; Li, W.; Voznyy, O.; Comin, R.; Yuan, M. J.; Jeon, S.; Ning, Z. J.; McDowell, J. J.; Kanjanaboos, P.; Sun, J. P.; Lan, X. Z.; Quan, L. N.; Kim, D. H.; Hill, I. G.; Maksymovych, P.; Sargent, E. H. Perovskite-Fullerene Hybrid Materials Suppress Hysteresis in Planar Diodes. *Nat. Commun.* **2015**, *6*, 7081.
(111) Shao, Y.; Xiao, Z.; Bi, C.; Yuan, Y.; Huang, J. Origin and Elimination of Photocurrent Hysteresis by Fullerene Passivation in CH3NH3PbI3 Planar Heterojunction Solar Cells. *Nat. Commun.* **2014**, *5*, 5784.
(112) Abate, A.; Saliba, M.; Hollman, D. J.; Stranks, S. D.; Wojciechowski, K.; Avolio, R.; Grancini, G.; Petrozza, A.; Snaith, H. J. Supramolecular Halogen Bond Passivation of Organic-Inorganic Halide Perovskite Solar Cells. *Nano Lett.* **2014**, *14* (6), 3247-3254.
(113) Bi, C.; Zheng, X. P.; Chen, B.; Wei, H. T.; Huang, J. S. Spontaneous Passivation of Hybrid Perovskite by Sodium Ions from Glass Substrates: Mysterious Enhancement of Device Efficiency Revealed. *ACS Energy Lett.* **2017**, *2* (6), 1400-1406.
(114) Abdi-Jalebi, M.; Andaji-Garmaroudi, Z.; Cacovich, S.; Stavrakas, C.; Philippe, B.; Richter, J. M.; Alsari, M.; Booker, E. P.; Hutter, E. M.; Pearson, A. J.; Lilliu, S.; Savenije, T. J.; Rensmo, H.; Divitini, G.; Ducati, C.; Friend, R. H.; Stranks, S. D. Maximizing and Stabilizing Luminescence from Halide Perovskites with Potassium Passivation. *Nature* **2018**, *555* (7697), 497-501.

(115) Zuo, L. J.; Guo, H. X.; deQuilettes, D. W.; Jariwala, S.; De Marco, N.; Dong, S. Q.; DeBlock, R.; Ginger, D. S.; Dunn, B.; Wang, M. K.; Yang, Y. Polymer-Modified Halide Perovskite Films for Efficient and Stable Planar Heterojunction Solar Cells. *Sci. Adv.* **2017**, *3* (8), 1700106.
(116) Cao, J.; Yin, J.; Yuan, S. F.; Zhao, Y.; Li, J.; Zheng, N. F. Thiols as Interfacial Modifiers to Enhance the Performance and Stability of Perovskite Solar Cells. *Nanoscale* **2015**, *7* (21), 9443-9447.
(117) Braly, I. L.; deQilettes, D. W.; Pazos-Outon, L. M.; Burke, S.; Ziffer, M. E.; Ginger, D. S.; Hillhouse, H. W. Hybrid Perovskite Films Approaching the Radiative Limit with over 90% Photoluminescence Quantum Efficiency. *Nat. Photonics* **2018**, *12* (6), 355-361.
(118) Chen, Q.; Zhou, H.; Fang, Y.; Stieg, A. Z.; Song, T.-B.; Wang, H.-H.; Xu, X.; Liu, Y.; Lu, S.; You, J.; Sun, P.; McKay, J.; Goorsky, M. S.; Yang, Y. The Optoelectronic Role of Chlorine in CH3NH3PbI3(Cl)-Based Perovskite Solar Cells. *Nat. Commun.* **2015**, *6*, 7269.
(119) Nan, G. J.; Zhang, X.; Abdi-Jalebi, M.; Andaji-Garmaroudi, Z.; Stranks, S. D.; Lu, G.; Beljonne, D. How Methylammonium Cations and Chlorine Dopants Heal Defects in Lead Iodide Perovskites. *Adv. Energy Mater.* **2018**, *8* (13), 1702754.
(120) Wang, S.; Sakurai, T.; Wen, W.; Qi, Y.B. Energy Level Alignment at Interfaces in Metal Halide Perovskite Solar Cells. *Adv. Mater. Interfaces* **2018**, *5* (22), 1800260.
(121) Schulz, P.; Cahen, D.; Kahn, A. Halide Perovskites: Is It All About the Interfaces? *Chem. Rev.* **2019**, *119* (5), 3349-3417.
(122) Wang, Q. K.; Wang, R. B.; Shen, P. F.; Li, C.; Li, Y. Q.; Liu, L. J.; Duhm, S.; Tang, J. X. Energy Level Offsets at Lead Halide Perovskite/Organic Hybrid Interfaces and Their Impacts on Charge Separation. *Adv. Mater. Interfaces* **2015**, *2* (3), 1400528.
(123) Polander, L. E.; Pahner, P.; Schwarze, M.; Saalfrank, M.; Koerner, C.; Leo, K., Hole-Transport Material Variation in Fully Vacuum Deposited Perovskite Solar Cells. *APL Mater.* **2014**, *2* (8), 081503.
(124) Belisle, R. A.; Jain, P.; Prasanna, R.; Leijtens, T.; McGehee, M. D. Minimal Effect of the Hole-Transport Material Ionization Potential on the Open-Circuit Voltage of Perovskite Solar Cells. *ACS Energy Lett.* **2016**, *1* (3), 556-560.
(125) Park, S. M.; Mazza, S. M.; Liang, Z. M.; Abtahi, A.; Boehm, A. M.; Parkin, S. R.; Anthony, J. E.; Graham, K. R. Processing Dependent Influence of the Hole Transport Layer Ionization Energy on Methylammonium Lead Iodide Perovskite Photovoltaics. *ACS Appl. Mater. Interfaces* **2018**, *10* (18), 15548-15557.
(126) Schulz, P.; Whittaker-Brooks, L. L.; MacLeod, B. A.; Olson, D. C.; Loo, Y. L.; Kahn, A. Electronic Level Alignment in Inverted Organometal Perovskite Solar Cells. *Adv. Mater. Interfaces* **2015**, *2* (7) 1400532.
(127) Wang, C. G.; Wang, C. C.; Liu, X. L.; Kauppi, J.; Shao, Y. C.; Xiao, Z. G.; Bi, C.; Huang, J. S.; Gao, Y. L. Electronic Structure Evolution of Fullerene on CH3NH3PbI3. *Appl. Phys. Lett.* **2015**, *106* (11), 111603.
(128) Shin, D.; Kang, D.; Jeong, J.; Park, S.; Kim, M.; Lee, H.; Yi, Y. Unraveling the Charge Extraction Mechanism of Perovskite Solar Cells Fabricated with Two-Step Spin Coating: Interfacial Energetics between Methylammonium Lead Iodide and C-60. *J. Phys. Chem. Lett.* **2017**, *8* (21), 5423-5429.
(129) Chen, W.; Qi, D.-C.; Huang, H.; Gao, X.; Wee, A. T. S. Organic–Organic Heterojunction Interfaces: Effect of Molecular Orientation. *Adv. Funct. Mater.* **2011**, *21* (3), 410-424.
(130) Zhou, H. P.; Chen, Q.; Li, G.; Luo, S.; Song, T. B.; Duan, H. S.; Hong, Z. R.; You, J. B.; Liu, Y. S.; Yang, Y. Interface Engineering of Highly Efficient Perovskite Solar Cells. *Science* **2014**, *345* (6196), 542-546.
(131) Niu, G. D.; Li, W. Z.; Meng, F. Q.; Wang, L. D.; Dong, H. P.; Qiu, Y., Study on the Stability of CH3NH3PbI3 Films and the Effect of Post-Modification by Aluminum Oxide in All-Solid-State Hybrid Solar Cells. *J. Mater. Chem. A* **2014**, *2* (3), 705-710.
(132) Niu, G. D.; Guo, X. D.; Wang, L. D. Review of Recent Progress in Chemical Stability of Perovskite Solar Cells. *J. Mater. Chem. A* **2015**, *3* (17), 8970-8980.

(133) Leguy, A. M. A.; Hu, Y.; Campoy-Quiles, M.; Alonso, M. I.; Weber, O. J.; Azarhoosh, P.; van Schilfgaarde, M.; Weller, M. T.; Bein, T.; Nelson, J.; Docampo, P.; Barnes, P. R. F. Reversible Hydration of CH(3)NH(3)PbI(3) in Films, Single Crystals, and Solar Cells. *Chem. Mater.* **2015**, *27* (9), 3397-3407.
(134) Hailegnaw, B.; Kirmayer, S.; Edri, E.; Hodes, G.; Cahen, D. Rain on Methylammonium Lead Iodide Based Perovskites: Possible Environmental Effects of Perovskite Solar Cells. *J. Phys. Chem. Lett.* **2015**, *6* (9), 1543-1547.
(135) Berhe, T. A.; Su, W. N.; Chen, C. H.; Pan, C. J.; Cheng, J. H.; Chen, H. M.; Tsai, M. C.; Chen, L. Y.; Dubale, A. A.; Hwang, B. J. Organometal Halide Perovskite Solar Cells: Degradation and Stability. *Energy Environ. Sci.* **2016**, *9* (2), 323-356.
(136) Christians, J. A.; Herrera, P. A. M.; Kamat, P. V. Transformation of the Excited State and Photovoltaic Efficiency of CH3NH3PbI3 Perovskite Upon Controlled Exposure to Humidified Air. *J. Am. Chem. Soc.* **2015**, *137* (4), 1530-1538.
(137) Senocrate, A.; Acartürk, T.; Kim, G. Y.; Merkle, R.; Starke, U.; Grätzel, M.; Maier, J. Interaction of Oxygen with Halide Perovskites. *J. Mater. Chem. A* **2018**, *6* (23), 10847-10855.
(138) Ito, S.; Tanaka, S.; Manabe, K.; Nishino, H. Effects of Surface Blocking Layer of Sb2S3 on Nanocrystalline TiO2 for CH3NH3PbI3 Perovskite Solar Cells. *J. Phys. Chem. C* **2014**, *118* (30), 16995-17000.
(139) Noh, J. H.; Im, S. H.; Heo, J. H.; Mandal, T. N.; Seok, S. I. Chemical Management for Colorful, Efficient, and Stable Inorganic-Organic Hybrid Nanostructured Solar Cells. *Nano Lett.* **2013**, *13* (4), 1764-1769.
(140) Hu, Y.; Aygüler, M. F.; Petrus, M. L.; Bein, T.; Docampo, P. Impact of Rubidium and Cesium Cations on the Moisture Stability of Multiple-Cation Mixed-Halide Perovskites. *ACS Energy Lett.* **2017**, *2* (10), 2212-2218.
(141) Abdi-Jalebi, M.; Andaji-Garmaroudi, Z.; Pearson, A. J.; Divitini, G.; Cacovich, S.; Philippe, B.; Rensmo, H.; Ducati, C.; Friend, R. H.; Stranks, S. D. Potassium- and Rubidium-Passivated Alloyed Perovskite Films: Optoelectronic Properties and Moisture Stability. *ACS Energy Lett.* **2018**, *3* (11), 2671-2678.
(142) Li, N.; Tao, S.; Chen, Y.; Niu, X.; Onwudinanti, C. K.; Hu, C.; Qiu, Z.; Xu, Z.; Zheng, G.; Wang, L.; Zhang, Y.; Li, L.; Liu, H.; Lun, Y.; Hong, J.; Wang, X.; Liu, Y.; Xie, H.; Gao, Y.; Bai, Y.; Yang, S.; Brocks, G.; Chen, Q.; Zhou, H. Cation and Anion Immobilization through Chemical Bonding Enhancement with Fluorides for Stable Halide Perovskite Solar Cells. *Nat. Energy* **2019**, *4* (5), 408-415.
(143) Grancini, G.; Roldan-Carmona, C.; Zimmermann, I.; Mosconi, E.; Lee, X.; Martineau, D.; Narbey, S.; Oswald, F.; De Angelis, F.; Graetzel, M.; Nazeeruddin, M. K. One-Year Stable Perovskite Solar Cells by 2D/3D Interface Engineering. *Nat. Commun.* **2017**, *8*, 15684.
(144) Cao, J.; Lv, X. D.; Feng, X. X.; Meng, R. Q.; Wu, Y. Y.; Tang, Y. Efficient Grain Boundary Suture by Low-Cost Tetra-Ammonium Zinc Phthalocyanine for Stable Perovskite Solar Cells with Expanded Photoresponse. *J. Am. Chem. Soc.* **2018**, *140* (37), 11577-11580.
(145) Arora, N.; Dar, M. I.; Hinderhofer, A.; Pellet, N.; Schreiber, F.; Zakeeruddin, S. M.; Gratzel, M. Perovskite Solar Cells with CuSCN Hole Extraction Layers Yield Stabilized Efficiencies Greater Than 20%. *Science* **2017**, *358* (6364), 768-771.
(146) Wang, H.; Yang, F.; Xiang, Y.; Ye, S.; Peng, X.; Song, J.; Qu, J.; Wong, W.-Y. Achieving Efficient Inverted Perovskite Solar Cells with Excellent Electron Transport and Stability by Employing a Ladder-Conjugated Perylene Diimide Dimer. *J. Mater. Chem. A* **2019**, *7* (42), 24191-24198.
(147) Shin, S. S.; Yeom, E. J.; Yang, W. S.; Hur, S.; Kim, M. G.; Im, J.; Seo, J.; Noh, J. H.; Seok, S. I. Colloidally Prepared La-Doped BaSnO3 Electrodes for Efficient, Photostable Perovskite Solar Cells. *Science* **2017**, *356* (6334), 167-171.
(148) Turren-Cruz, S. H.; Hagfeldt, A.; Saliba, M. Methylammonium-Free, High-Performance, and Stable Perovskite Solar Cells on a Planar Architecture. *Science* **2018**, *362* (6413), 449-453.

(149) Jung, E. H.; Jeon, N. J.; Park, E. Y.; Moon, C. S.; Shin, T. J.; Yang, T.-Y.; Noh, J. H.; Seo, J. Efficient, Stable and Scalable Perovskite Solar Cells Using Poly(3-Hexylthiophene). *Nature* **2019**, *567* (7749), 511-515.
(150) Ohmann, R.; Ono, L. K.; Kim, H. S.; Lin, H.; Lee, M. V.; Li, Y.; Park, N. G.; Qi, Y.B. Real-Space Imaging of the Atomic Structure of Organic-Inorganic Perovskite. *J. Am. Chem. Soc.* **2015**, *137* (51), 16049-54.
(151) She, L. M.; Liu, M. Z.; Zhong, D. Y. Atomic Structures of CH3NH3PbI3 (001) Surfaces. *ACS Nano* **2016**, *10* (1), 1126-1131.
(152) She, L.; Liu, M.; Li, X.; Cai, Z.; Zhong, D. Growth and Interfacial Structure of Methylammonium Lead Iodide Thin Films on Au(111). *Surf. Sci.* **2016**, *656*, 17-23.
(153) Cai, L.; She, L.; Qin, H.; Xu, L.; Zhong, D. Monolayer Methylammonium Lead Iodide Films Deposited on Au(111). *Surf. Sci.* **2018**, *675*, 78-82.
(154) Hsu, H.-C.; Huang, B.-C.; Chin, S.-C.; Hsing, C.-R.; Nguyen, D.-L.; Schnedler, M.; Sankar, R.; Dunin-Borkowski, R. E.; Wei, C.-M.; Chen, C.-W.; Ebert, P.; Chiu, Y.-P. Photodriven Dipole Reordering: Key to Carrier Separation in Metalorganic Halide Perovskites. *ACS Nano* **2019**, *13* (4), 4402-4409.
(155) Mugarza, A.; Krull, C.; Robles, R.; Stepanow, S.; Ceballos, G.; Gambardella, P. Spin Coupling and Relaxation inside Molecule-Metal Contacts. *Nat. Commun.* **2011**, *2*, 490.
(156) Jiang, X. Q.; Yu, Z.; Li, H. B.; Zhao, Y. W.; Qu, J. S.; Lai, J. B.; Ma, W. Y.; Wang, D. P.; Yang, X. C.; Sun, L. C. A Solution-Processable Copper(II) Phthalocyanine Derivative as a Dopant-Free Hole-Transporting Material for Efficient and Stable Carbon Counter Electrode-Based Perovskite Solar Cells. *J. Mater. Chem. A* **2017**, *5* (34), 17862-17866.
(157) Uhlmann, C.; Swart, I.; Repp, J. Controlling the Orbital Sequence in Individual Cu-Phthalocyanine Molecules. *Nano Lett.* **2013**, *13* (2), 777-780.
(158) Gardener, J.; Owen, J. H. G.; Miki, K.; Heutz, S. A Scanning Tunnelling Microscopy Investigation into the Initial Stages of Copper Phthalocyanine Growth on Passivated Silicon Surfaces. *Surf. Sci.* **2008**, *602* (4), 843-851.
(159) Sk, R.; Mulani, I.; Deshpande, A., Emergent Properties of the Organic Molecule-Topological Insulator Hybrid Interface: Cu-Phthalocyanine on Bi2Se3. *J. Phys. Chem. C* **2018**, *122* (40), 22996-23001.
(160) Sun, K.; Tao, M. L.; Tu, Y. B.; Wang, J. Z. Off-Center Rotation of CuPc Molecular Rotor on a Bi(111) Surface and the Chiral Feature. *Molecules* **2017**, *22* (5), 740.
(161) Whitaker, A., X-Ray Powder Diffraction of Synthetic Organic Colorants. In *Analytical Chemistry of Synthetic Colorants*, Peters, A. T.; Freeman, H. S., Eds. Springer Netherlands: Dordrecht, 1995; pp 1-48.
(162) Law, K. Y. Organic Photoconductive Materials: Recent Trends and Developments. *Chem. Rev.* **1993**, *93* (1), 449-486.
(163) Sappok, R. J., *Oil and Colour Chem. Assoc.* **1978**, *61*, 299.
(164) Tidhar, Y.; Edri, E.; Weissman, H.; Zohar, D.; Hodes, G.; Cahen, D.; Rybtchinski, B.; Kirmayer, S. Crystallization of Methyl Ammonium Lead Halide Perovskites: Implications for Photovoltaic Applications. *J. Am. Chem. Soc.* **2014**, *136* (38), 13249-13256.
(165) Peng, W.; Wang, L.; Banavoth, M.; Ho, K.-T.; Bera, A.; Cho, N.; Kang, C.-F.; Burlakov, V.; Pan, J.; Sinatra, L.; Ma, C.; Xu, W.; Shi, D.; Alarousu, E.; Goriely, A.; He, J.-H.; Mohammed, O.; Wu, T.; Bakr, O. Solution-Grown Monocrystalline Hybrid Perovskite Films for Hole-Transporter-Free Solar Cells. *Adv. Mater.* **2016**, *28*, 3383-3390.
(166) Jaffe, A.; Lin, Y.; Beavers, C. M.; Voss, J.; Mao, W. L.; Karunadasa, H. I. High-Pressure Single-Crystal Structures of 3D Lead-Halide Hybrid Perovskites and Pressure Effects on Their Electronic and Optical Properties. *ACS Cent. Sci.* **2016**, *2* (4), 201-209.
(167) Hieulle, J.; Wang, X. M.; Stecker, C.; Son, D. Y.; Qu, L. B.; Ohmann, R.; Ono, L. K.; Mugarza, A.; Yan, Y. F.; Qi, Y. B. Unraveling the Impact of Halide Mixing on Perovskite Stability. *J. Am. Chem. Soc.* **2019**, *141* (8), 3515-3523.

(168) Stecker, C.; Liu, K.; Hieulle, J.; Ohmann, R.; Liu, Z.; Ono, L. K.; Wang, G.; Qi, Y.B. Surface Defect Dynamics in Organic–Inorganic Hybrid Perovskites: From Mechanism to Interfacial Properties. *ACS Nano* **2019**, *13* (10), 12127-12136.
(169) Binnig, G.; Rohrer, H. Scanning Tunneling Microscopy. *Helv. Phys. Acta.* **1982**, *55* (6), 726-735.
(170) Liu, L.; McLeod, J. A.; Wang, R.; Shen, P.; Duhm, S. Tracking the Formation of Methylammonium Lead Triiodide Perovskite. *Appl. Phys. Lett.* **2015**, *107* (6), 061904.
(171) Lindblad, R.; Jena, N. K.; Philippe, B.; Oscarsson, J.; Bi, D. Q.; Lindblad, A.; Mandal, S.; Pal, B.; Sarma, D. D.; Karis, O.; Siegbahn, H.; Johansson, E. M. J.; Odelius, M.; Rensmo, H. Electronic Structure of Ch3nh3pbx3 Perovskites: Dependence on the Halide Moiety. *J. Phys. Chem. C* **2015**, *119* (4), 1818-1825.
(172) Lindblad, R.; Bi, D. Q.; Park, B. W.; Oscarsson, J.; Gorgoi, M.; Siegbahn, H.; Odelius, M.; Johansson, E. M. J.; Rensmo, H. Electronic Structure of TiO2/CH(3)NH(3)PbI(3) Perovskite Solar Cell Interfaces. *J. Phys. Chem. Lett.* **2014**, *5* (4), 648-653.
(173) Miller, D. W.; Eperon, G. E.; Roe, E. T.; Warren, C. W.; Snaith, H. J.; Lonergan, M. C. Defect States in Perovskite Solar Cells Associated with Hysteresis and Performance. *Appl. Phys. Lett.* **2016**, *109* (15), 153902.
(174) Liu, Z. H.; Hu, J. N.; Jiao, H. Y.; Li, L.; Zheng, G. H. J.; Chen, Y. H.; Huang, Y.; Zhang, Q.; Shen, C.; Chen, Q.; Zhou, H. P. Chemical Reduction of Intrinsic Defects in Thicker Heterojunction Planar Perovskite Solar Cells. *Adv. Mater.* **2017**, *29* (23), 1606774.
(175) Ball, J. M.; Petrozza, A. Defects in Perovskite-Halides and Their Effects in Solar Cells. *Nat. Energy* **2016**, *1*, 1-13.
(176) Wang, L. G.; Zhou, H. P.; Hu, J. N.; Huang, B. L.; Sun, M. Z.; Dong, B. W.; Zheng, G. H. J.; Huang, Y.; Chen, Y. H.; Li, L.; Xu, Z. Q.; Li, N. X.; Liu, Z.; Chen, Q.; Sun, L. D.; Yan, C. H. A Eu3+-Eu2+ Ion Redox Shuttle Imparts Operational Durability to Pb-I Perovskite Solar Cells. *Science* **2019**, *363* (6424), 265-270.
(177) Zhang, F.; Bi, D. Q.; Pellet, N.; Xiao, C. X.; Li, Z.; Berry, J. J.; Zakeeruddin, S. M.; Zhu, K.; Gratzel, M. Suppressing Defects through the Synergistic Effect of a Lewis Base and a Lewis Acid for Highly Efficient and Stable Perovskite Solar Cells. *Energy Environ. Sci.* **2018**, *11* (12), 3480-3490.
(178) Lin, C. T.; De Rossi, F.; Kim, J.; Baker, J.; Ngiam, J.; Xu, B.; Pont, S.; Aristidou, N.; Haque, S. A.; Watson, T.; McLachlan, M. A.; Durrant, J. R. Evidence for Surface Defect Passivation as the Origin of the Remarkable Photostability of Unencapsulated Perovskite Solar Cells Employing Aminovaleric Acid as a Processing Additive. *J. Mater. Chem. A* **2019**, *7* (7), 3006-3011.
(179) Zheng, X. P.; Deng, Y. H.; Chen, B.; Wei, H. T.; Xiao, X.; Fang, Y. J.; Lin, Y. Z.; Yu, Z. H.; Liu, Y.; Wang, Q.; Huang, J. S. Dual Functions of Crystallization Control and Defect Passivation Enabled by Sulfonic Zwitterions for Stable and Efficient Perovskite Solar Cells. *Adv. Mater.* **2018**, *30* (52), 1803428.
(180) Wu, Z. F.; Raga, S. R.; Juarez-Perez, E. J.; Yao, X. Y.; Jiang, Y.; Ono, L. K.; Ning, Z. J.; Tian, H.; Qi, Y. B. Improved Efficiency and Stability of Perovskite Solar Cells Induced by C=O Functionalized Hydrophobic Ammonium-Based Additives. *Adv. Mater.* **2018**, *30* (3), 1703670.
(181) Wang, S.; Jiang, Y.; Juarez-Perez, Emilio J.; Ono, Luis K.; Qi, Y.B. Accelerated Degradation of Methylammonium Lead Iodide Perovskites Induced by Exposure to Iodine Vapour. *Nat. Energy* **2016**, *2*, 16195.
(182) Juarez-Perez, E. J.; Ono, L. K.; Maeda, M.; Jiang, Y.; Hawash, Z.; Qi, Y. B. Photodecomposition and Thermal Decomposition in Methylammonium Halide Lead Perovskites and Inferred Design Principles to Increase Photovoltaic Device Stability. *J. Mater. Chem. A* **2018**, *6* (20), 9604-9612.
(183) Buin, A.; Pietsch, P.; Xu, J. X.; Voznyy, O.; Ip, A. H.; Comin, R.; Sargent, E. H. Materials Processing Routes to Trap-Free Halide Perovskites. *Nano Lett.* **2014**, *14* (11), 6281-6286.
(184) Gordillo, G.; Otalora, C. A.; Ramirez, A. A. A Study of Trap and Recombination Centers in MAPbI3 Perovskites. *Phys. Chem. Chem. Phys.* **2016**, *18* (48), 32862-32867.
(185) Yin, W. J.; Shi, T. T.; Yan, Y. F. Unique Properties of Halide Perovskites as Possible Origins of the Superior Solar Cell Performance. *Adv. Mater.* **2014**, *26* (27), 4653-4658.

(186) Walsh, A.; Scanlon, D. O.; Chen, S. Y.; Gong, X. G.; Wei, S. H. Self-Regulation Mechanism for Charged Point Defects in Hybrid Halide Perovskites. *Angew. Chem. Int. Edit.* **2015**, *54* (6), 1791-1794.
(187) Kim, J.; Lee, S. H.; Lee, J. H.; Hong, K. H. The Role of Intrinsic Defects in Methylammonium Lead Iodide Perovskite. *J. Phys. Chem. Lett.* **2014**, *5* (8), 1312-1317.
(188) Yuan, Y. B.; Huang, J. S. Ion Migration in Organometal Trihalide Perovskite and Its Impact on Photovoltaic Efficiency and Stability. *Acc. Chem. Res.* **2016**, *49* (2), 286-293.
(189) Unger, E. L.; Hoke, E. T.; Bailie, C. D.; Nguyen, W. H.; Bowring, A. R.; Heumuller, T.; Christoforo, M. G.; McGehee, M. D. Hysteresis and Transient Behavior in Current-Voltage Measurements of Hybrid-Perovskite Absorber Solar Cells. *Energy Environ. Sci.* **2014**, *7* (11), 3690-3698.
(190) Yuan, Y. B.; Wang, Q.; Shao, Y. C.; Lu, H. D.; Li, T.; Gruverman, A.; Huang, J. S. Electric-Field-Driven Reversible Conversion between Methylammonium Lead Triiodide Perovskites and Lead Iodide at Elevated Temperatures. *Adv. Energy Mater.* **2016**, *6* (2), 1501803.
(191) Bag, M.; Renna, L. A.; Adhikari, R. Y.; Karak, S.; Liu, F.; Lahti, P. M.; Russell, T. P.; Tuominen, M. T.; Venkataraman, D. Kinetics of Ion Transport in Perovskite Active Layers and Its Implications for Active Layer Stability. *J. Am. Chem. Soc.* **2015**, *137* (40), 13130-13137.
(192) De Bastiani, M.; Dell'Erba, G.; Gandini, M.; D'Innocenzo, V.; Neutzner, S.; Kandada, A. R. S.; Grancini, G.; Binda, M.; Prato, M.; Ball, J. M.; Caironi, M.; Petrozza, A. Ion Migration and the Role of Preconditioning Cycles in the Stabilization of the J-V Characteristics of Inverted Hybrid Perovskite Solar Cells. *Adv. Energy Mater.* **2016**, *6* (2), 1501453.
(193) Yang, Y.; Yang, M.; Moore, David T.; Yan, Y.; Miller, E.M.; Zhu, K.; Beard, M. C. Top and Bottom Surfaces Limit Carrier Lifetime in Lead Iodide Perovskite Films. *Nat. Energy* **2017**, *2*, 16207.
(194) Knorr, N.; Brune, H.; Epple, M.; Hirstein, A.; Schneider, M. A.; Kern, K. Long-Range Adsorbate Interactions Mediated by a Two-Dimensional Electron Gas. *Phys. Rev. B* **2002**, *65* (11), 115420.
(195) Liu, Y.; Palotas, K.; Yuan, X.; Hou, T.; Lin, H.; Li, Y.; Lee, S. T. Atomistic Origins of Surface Defects in CH3NH3PbBr3 Perovskite and Their Electronic Structures. *ACS Nano* **2017**, *11* (2), 2060-2065.
(196) Choi, J. I. J.; Khan, M. E.; Hawash, Z.; Kim, K. J.; Lee, H.; Ono, L. K.; Qi, Y.; Kim, Y.-H.; Park, J. Y. Atomic-Scale View of Stability and Degradation of Single-Crystal MAPbBr3 Surfaces. *J. Mater. Chem. A* **2019**, *7*, 20760-20766.
(197) Fomin, E.; Tatarkhanov, M.; Mitsui, T.; Rose, M.; Ogletree, D.; Salmeron, M. Vibrationally Assisted Diffusion of H2O and D2O on Pd(111). *Surf. Sci.* **2006**, *600*, 542-546.
(198) Kresse, G.; Hafner, J. *Ab Initio* Molecular Dynamics for Liquid Metals. *Phys. Rev. B: Condens. Matter Mater. Phys.* **1993**, *47* (1), 558-561.
(199) Kresse, G.; Furthmuller, J. Efficiency of *Ab Initio* Total Energy Calculations for Metals and Semiconductors Using a Plane-Wave Basis Set. *Comp. Mater. Sci.* **1996**, *6* (1), 15-50.
(200) Kresse, G.; Joubert, D. From Ultrasoft Pseudopotentials to the Projector Augmented-Wave Method. *Phys. Rev. B* **1999**, *59* (3), 1758-1775.
(201) Blochl, P. E. Projector Augmented-Wave Method. *Phys Rev B: Condens. Matter Mater. Phys.* **1994**, *50* (24), 17953-17979.
(202) Perdew, J. P.; Burke, K.; Ernzerhof, M. Generalized Gradient Approximation Made Simple. *Phys. Rev. Lett.* **1996**, *77* (18), 3865-3868.
(203) Monkhorst, H. J.; Pack, J. D. Special Points for Brillouin-Zone Integrations. *Phys. Rev. B* **1976**, *13* (12), 5188-5192.
(204) Henkelman, G.; Uberuaga, B. P.; Jonsson, H. A Climbing Image Nudged Elastic Band Method for Finding Saddle Points and Minimum Energy Paths. *J. Chem. Phys.* **2000**, *113* (22), 9901-9904.
(205) Gustafsson, A.; Okabayashi, N.; Peronio, A.; Giessibl, F. J.; Paulsson, M. Analysis of STM Images with Pure and Co-Functionalized Tips: A First-Principles and Experimental Study. *Phys. Rev. B* **2017**, *96* (8), 085415.

(206) Walsh, A.; Stranks, S. D., Taking Control of Ion Transport in Halide Perovskite Solar Cells. *ACS Energy Lett.* **2018**, *3* (8), 1983-1990.
(207) Zhang, Y. P.; Wang, Y. S.; Xu, Z. Q.; Liu, J. Y.; Song, J. C.; Xue, Y. Z.; Wang, Z. Y.; Zheng, J. L.; Jiang, L. C.; Zheng, C. X.; Huang, F. Z.; Sun, B. Q.; Cheng, Y. B.; Bao, Q. L. Reversible Structural Swell-Shrink and Recoverable Optical Properties in Hybrid Inorganic-Organic Perovskite. *ACS Nano* **2016**, *10* (7), 7031-7038.
(208) Leblebici, S. Y.; Leppert, L.; Li, Y.; Reyes-Lillo, S. E.; Wickenburg, S.; Wong, E.; Lee, J.; Melli, M.; Ziegler, D.; Angell, D. K.; Ogletree, D. F.; Ashby, Paul D.; Toma, F. M.; Neaton, J. B.; Sharp, I. D.; Weber-Bargioni, A. Facet-Dependent Photovoltaic Efficiency Variations in Single Grains of Hybrid Halide perovskite. *Nat. Energy* **2016**, *1*, 16093.
(209) Kim, D. H.; Park, J.; Li, Z.; Yang, M. J.; Park, J. S.; Park, I. J.; Kim, J. Y.; Berry, J. J.; Rumbles, G.; Zhu, K. 300% Enhancement of Carrier Mobility in Uniaxial-Oriented Perovskite Films Formed by Topotactic-Oriented Attachment. *Adv. Mater.* **2017**, *29* (23), 1606831.
(210) Ono, L. K.; Qi, Y. B. Surface and Interface Aspects of Organometal Halide Perovskite Materials and Solar Cells. *J. Phys. Chem. Lett.* **2016**, *7* (22), 4764-4794.
(211) Jacobs, R.; Booske, J.; Morgan, D. Understanding and Controlling the Work Function of Perovskite Oxides Using Density Functional Theory. *Adv. Funct. Mater.* **2016**, *26* (30), 5471-5482.
(212) Šimėnas, M.; Banys, J.; Tornau, E. E. Screening of Point Defects in Methylammonium Lead Halides: A Monte Carlo Study. *J. Mater. Chem. C* **2018**, *6* (6), 1487-1494.
(213) Coropceanu, V.; Cornil, J.; da Silva Filho, D. A.; Olivier, Y.; Silbey, R.; Brédas, J.-L. Charge Transport in Organic Semiconductors. *Chem. Rev.* **2007**, *107* (4), 926-952.
(214) Protesescu, L.; Yakunin, S.; Bodnarchuk, M. I.; Krieg, F.; Caputo, R.; Hendon, C. H.; Yang, R. X.; Walsh, A.; Kovalenko, M. V. Nanocrystals of Cesium Lead Halide Perovskites (CsPbX3, X = Cl, Br, and I): Novel Optoelectronic Materials Showing Bright Emission with Wide Color Gamut. *Nano Lett.* **2015**, *15* (6), 3692-3696.
(215) Gil-Escrig, L.; Miquel-Sempere, A.; Sessolo, M.; Bolink, H. J. Mixed Iodide-Bromide Methylammonium Lead Perovskite-Based Diodes for Light Emission and Photovoltaics. *J. Phys. Chem. Lett.* **2015**, *6* (18), 3743-3748.
(216) Jong, U. G.; Yu, C. J.; Ri, J. S.; Kim, N. H.; Ri, G. C., Influence of Halide Composition on the Structural, Electronic, and Optical Properties of Mixed CH3NH3Pb(I1-XBrx)(3) Perovskites Calculated Using the Virtual Crystal Approximation Method. *Phys. Rev. B* **2016**, *94* (12), 125139.
(217) Yang, M. J.; Zhang, T. Y.; Schulz, P.; Li, Z.; Li, G.; Kim, D. H.; Guo, N. J.; Berry, J. J.; Zhu, K.; Zhao, Y. X. Facile Fabrication of Large-Grain CH3NH3PbI3-XBrx Films for High-Efficiency Solar Cells Via CH3NH3Br-Selective Ostwald Ripening. *Nat. Commun.* **2016,** *7*, 12305.
(218) Zhao, Y.; Zhu, K., CH3NH3Cl-Assisted One-Step Solution Growth of CH3NH3PbI3: Structure, Charge-Carrier Dynamics, and Photovoltaic Properties of Perovskite Solar Cells. *J. Phys. Chem. C* **2014**, *118* (18), 9412-9418.
(219) Edri, E.; Kirmayer, S.; Cahen, D.; Hodes, G. High Open-Circuit Voltage Solar Cells Based on Organic–Inorganic Lead Bromide Perovskite. *J. Phys. Chem. Lett.* **2013**, *4* (6), 897-902.
(220) Edri, E.; Kirmayer, S.; Kulbak, M.; Hodes, G.; Cahen, D. Chloride Inclusion and Hole Transport Material Doping to Improve Methyl Ammonium Lead Bromide Perovskite-Based High Open-Circuit Voltage Solar Cells. *J. Phys. Chem. Lett.* **2014**, *5* (3), 429-433.
(221) Zhang, M.; Yu, H.; Lyu, M. Q.; Wang, Q.; Yun, J. H.; Wang, L. Z. Composition-Dependent Photoluminescence Intensity and Prolonged Recombination Lifetime of Perovskite CH3NH3PbBr3-XClx Films. *Chem. Commun.* **2014**, *50* (79), 11727-11730.
(222) Pool, V. L.; Gold-Parker, A.; McGehee, M. D.; Toney, M. F. Chlorine in PbCl2-Derived Hybrid-Perovskite Solar Absorbers. *Chem. Mater.* **2015**, *27* (21), 7240-7243.

(223) Zhang, T.; Yang, M.; Benson, E. E.; Li, Z.; van de Lagemaat, J.; Luther, J. M.; Yan, Y.; Zhu, K.; Zhao, Y. A Facile Solvothermal Growth of Single Crystal Mixed Halide Perovskite CH3NH3Pb(Br(1-X)Cl(X))3. *Chem. Commun.* **2015**, *51* (37), 7820-7823.
(224) Yin, W. J.; Yang, J. H.; Kang, J.; Yan, Y. F.; Wei, S. H. Halide Perovskite Materials for Solar Cells: A Theoretical Review. *J. Mater. Chem. A* **2015**, *3* (17), 8926-8942.
(225) Ye, M. D.; Hong, X. D.; Zhang, F. Y.; Liu, X. Y. Recent Advancements in Perovskite Solar Cells: Flexibility, Stability and Large Scale. *J. Mater. Chem. A* **2016**, *4* (18), 6755-6771.
(226) Luo, S. Q.; Daoud, W. A. Crystal Structure Formation of CH3NH3PbI3-XClx Perovskite. *Materials* **2016**, *9* (3), 123.
(227) Zhou, Y. Y.; Zhou, Z. M.; Chen, M.; Zong, Y. X.; Huang, J. S.; Pang, S. P.; Padture, N. P. Doping and Alloying for Improved Perovskite Solar Cells. *J. Mater. Chem. A* **2016**, *4* (45), 17623-17635.
(228) Luo, Y. R. *Comprehensive Handbook of Chemical Bond Energies*. CRC Press: Boca Raton, FL, 2007.
(229) Conings, B.; Drijkoningen, J.; Gauquelin, N.; Babayigit, A.; D'Haen, J.; D'Olieslaeger, L.; Ethirajan, A.; Verbeeck, J.; Manca, J.; Mosconi, E.; De Angelis, F.; Boyen, H. G. Intrinsic Thermal Instability of Methylammonium Lead Trihalide Perovskite. *Adv. Energy Mater.* **2015**, *5* (15), 1500477.
(230) Emara, J.; Schnier, T.; Pourdavoud, N.; Riedl, T.; Meerholz, K.; Olthof, S. Impact of Film Stoichiometry on the Ionization Energy and Electronic Structure of CH3NH3PbI3 Perovskites. *Adv. Mater.* **2016**, *28* (3), 553-559.
(231) Zhang, X. F.; Zhou, X. Y.; Zhang, L. Z.; Xu, B. M. Facile Phthalocyanine Doping into PEDOT Leads to Highly Efficient and Stable Inverted Metal Halide Perovskite Solar Cells. *J. Mater. Chem. A* **2018**, *6* (26), 12515-12522.
(232) Zhang, F. G.; Yang, X. C.; Cheng, M.; Wang, W. H.; Sun, L. C. Boosting the Efficiency and the Stability of Low Cost Perovskite Solar Cells by Using CuPc Nanorods as Hole Transport Material and Carbon as Counter Electrode. *Nano Energy* **2016**, *20*, 108-116.
(233) Löbbert, G. (2000). Phthalocyanines. In Ullmann's Encyclopedia of Industrial Chemistry, (2012).
(234) Buchholz, J. C.; Somorjai, G. A., The Surface Structures of Phthalocyanine Monolayers and Vapor-Grown Films: A Low-Energy Electron Diffraction Study. *J. Chem. Phys.* **1977**, *66* (2), 573-580.
(235) Mishra, N.; Mukherjee, B.; Xing, G.; Chakrabortty, S.; Guchhait, A.; Lim, J. Y. Cation Exchange Synthesis of Uniform PbSe/Pbs Core/Shell Tetra-Pods and Their Use as near-Infrared Photodetectors. *Nanoscale* **2016**, *8* (29), 14203-14212.
(236) Christians, J. A.; Fung, R. C. M.; Kamat, P. V. An Inorganic Hole Conductor for Organo-Lead Halide Perovskite Solar Cells. Improved Hole Conductivity with Copper Iodide. *J. Am. Chem. Soc.* **2014**, *136* (2), 758-764.
(237) Yang, C.-H.; Yau, S.-L.; Fan, L.-J.; Yang, Y.-W. Deposition of Lead Iodide Films on Rh(100) Electrodes from Colloidal Solutions—the Effect of an Iodine Adlayer. *Surf. Sci.* **2003**, *540* (2), 274-284.
(238) Palosz, B. The Structure of PbI2 polytypes 2h and 4h: A Study of the 2h-4h Transition. *J. Phys. Condens. Matter* **1990**, *2* (24), 5285-5295.
(239) Westenbrink, H.; Terpstra, P. In *On the Crystal Structure of Lead-Iodide*. Proc. K. Ned. Akad. Wet, 1926; pp 431-442.
(240) Hendricks Sterling, B. The Crystal Structures of the Monomethyl Ammonium Halides. In *Zeitschrift für Kristallographie - Crystalline Materials*, 1928; Vol. 67, pp 106-118.
(241) Haiss, W. S., J. K.; Gao, X.; Weaver, M. J. Iodine Adlayer Structures on Au(111) as Discerned by Atomic-Resolution Scanning Tunnelling Microscopy: Relation to Iodide Electrochemical Adsorption. *Surf. Sci.* **1992**, *274* (3), L593-L598.
(242) Huang, L.; Zeppenfeld, P.; Horch, S.; Comsa, G. Determination of Iodine Adlayer Structures on Au(111) by Scanning Tunneling Microscopy. *J. Chem. Phys.* **1997**, *107* (2), 585-591.

(243) Gao, X. P.; Weaver, M. J. Probing Redox-Induced Molecular-Transformations by Atomic-Resolution Scanning Tunneling Microscopy - Iodide Adsorption and Electrooxidation on Au(111) in Aqueous-Solution. *J. Am. Chem. Soc.* **1992**, *114* (22), 8544-8551.
(244) Crepaldi, A.; Pons, S.; Frantzeskakis, E.; Calleja, F.; Etzkorn, M.; Seitsonen, A. P.; Kern, K.; Brune, H.; Grioni, M. Combined ARPES and STM Study of Pb/Au(111) Moiré Structure: One Overlayer, Two Symmetries. *Phys. Rev. B* **2013**, *87* (11), 115138.
(245) Hallmark, V. M.; Chiang, S.; Rabolt, J. F.; Swalen, J. D.; Wilson, R. J. Observation of Atomic Corrugation on Au(111) by Scanning Tunneling Microscopy. *Phys. Rev. Lett.* **1987**, *59* (25), 2879-2882.
(246) Kim, J.; Shin, E. H.; Sharma, M. K.; Ihm, K.; Dugerjav, O.; Hwang, C.; Lee, H.; Ko, K. T.; Park, J. H.; Kim, M.; Kim, H.; Jung, M. H. Observation of Restored Topological Surface States in Magnetically Doped Topological Insulator. *Sci. Rep.* **2019**, *9*, 1331.
(247) Kobayashi, T.; Fujiyoshi, Y.; Iwatsu, F.; Uyeda, N. High-Resolution Tem Images of Zinc Phthalocyanine Polymorphs in Thin Films. *Acta Crystallogr. A* **1981**, *37* (5), 692-697.
(248) Hieulle, J.; Luo, S.; Son, D.-Y.; Jamshaid, A.; Stecker, C.; Liu, Z.; Na, G.; Yang, D.; Ohmann, R.; Ono, L. K.; Zhang, L.; Qi, Y. Imaging of the Atomic Structure of All-Inorganic Halide Perovskites. *J. Phys. Chem. Lett.* **2020**, 818-823.
(249) Delugas, P.; Filippetti, A.; Mattoni, A. Methylammonium Fragmentation in Amines as Source of Localized Trap Levels and the Healing Role of Cl in Hybrid Lead-Iodide Perovskites. *Phys. Rev. B* **2015**, *92* (4), 045301.
(250) Tong, G. Q.; Ono, L. K.; Qi, Y. B. Recent Progress of All-Bromide Inorganic Perovskite Solar Cells. *Energy Technol.* **2019**, 1900961.
(251) Liu, Z. Y.; Sun, B.; Liu, X. Y.; Han, J. H.; Ye, H. B.; Shi, T. L.; Tang, Z. R.; Liao, G. L. Efficient Carbon-Based CsPbBr3 Inorganic Perovskite Solar Cells by Using Cu-Phthalocyanine as Hole Transport Material. *Nano-Micro Lett.* **2018**, *10* (2), 34.
(252) Stoumpos, C. C.; Malliakas, C. D.; Peters, J. A.; Liu, Z. F.; Sebastian, M.; Im, J.; Chasapis, T. C.; Wibowo, A. C.; Chung, D. Y.; Freeman, A. J.; Wessels, B. W.; Kanatzidis, M. G. Crystal Growth of the Perovskite Semiconductor CsPbBr3: A New Material for High-Energy Radiation Detection. *Cryst. Growth Des.* **2013**, *13* (7), 2722-2727.
(253) Thind, A. S.; Luo, G.; Hachtel, J. A.; Morrell, M. V.; Cho, S. B.; Borisevich, A. Y.; Idrobo, J.-C.; Xing, Y.; Mishra, R. Atomic Structure and Electrical Activity of Grain Boundaries and Ruddlesden–Popper Faults in Cesium Lead Bromide Perovskite. *Adv. Mater.* **2019**, *31* (4), 1805047.
(254) Xue, J.; Yang, D. D.; Cai, B.; Xu, X. B.; Wang, J.; Ma, H.; Yu, X. C.; Yuan, G. L.; Zou, Y. S.; Song, J. Z.; Zeng, H. B. Photon-Induced Reversible Phase Transition in CsPbBr3 Perovskite. *Adv. Funct. Mater.* **2019**, *29* (13), 1807922.
(255) Hirotsu, S.; Harada, J.; Iizumi, M.; Gesi, K. Structural Phase-Transitions in CsPbBr3. *J. Phys. Soc. Jpn.* **1974**, *37* (5), 1393-1398.

List of publications during PhD at OIST

1. Stecker, C.; Liu, Z; Hieulle, J.; Ono, L.K.; Wang, G., Qi, Y.B. Atomic-scale imaging of the perovskite-CuPc interface (tentative title). *In preparation*.

2. Hieulle, J.; Luo, S.; Son, D.Y.; Jamshaid, A.; Stecker, C.; Liu, Z.; Na, G.; Yang, D.; Ohmann, R.; Ono, L.K.; Zhang, L.; Qi, Y.B. Imaging of the Atomic Structure of All-Inorganic Halide Perovskites. *Journal of Physical Chemistry Letters* **2020**, *11*, 818−823.

3. Stecker, C.; Liu, K; Hieulle, J.; Ohmann, R.; Liu, Z.; Ono, L.K.; Wang, G.; Qi, Y.B. Surface Defect Dynamics in Organic–Inorganic Hybrid Perovskites: From Mechanism to Interfacial Properties. *ACS Nano* **2019**, *13*, 12127-12136.

4. Hieulle, J., Wang, X., Stecker, C., Son, D.Y., Qiu, L., Ohmann, R., Ono, L.K., Mugarza, A., Yan, Y., Qi, Y.B., Unraveling the Impact of Halide Mixing on Perovskite Stability. *Journal of the American Chemical Society* **2019**, *141*, 3515–3523.

5. He, S; Qiu, L.; Son D.Y.; Liu, Z.; Juarez-Perez, E.J.; Ono, L.K.; Stecker, C.; Qi, Y.B. Carbon-Based Electrode Engineering Boosts the Efficiency of All Low-Temperature-Processed Perovskite Solar Cells. *ACS Energy Letters* **2019**, *4*, 2032-2039.

6. Hieulle, J., Stecker, C., Ohmann, R., Ono, L.K., Qi, Y.B., Scanning Probe Microscopy Applied to Organic-Inorganic Halide Perovskites and Solar Cells. *Small Methods* **2018**, *2*, 1700295.